Molecular Dynamics Studies of Permeation and Gating Mechanisms in Potassium Channels

Dissertation

for the award of the degree

"Doctor of Philosophy" (Ph.D.)
Division of Mathematics and Natural Sciences

of the Georg-August-Universität Göttingen

within the doctoral program
International Max-Planck Research School
for Physics of Biological and Complex Systems
of the Göttingen Graduate School
for Neurosciences, Biophysics and Molecular Biosciences

submitted by
Chun Kei Lam
from Hong Kong

Göttingen, 2023

Thesis Advisory Committee

Prof. Dr. Bert de Groot
Max Planck Institute for Multidisciplinary Sciences, Göttingen

Prof. Dr. Marcus Müller
Georg-August-Universität, Göttingen

Prof. Dr. Claudia Steinem
Georg-August-Universität, Göttingen

Members of the Examination Board

Prof. Dr. Bert de Groot
Max Planck Institute for Multidisciplinary Sciences, Göttingen

Prof. Dr. Marcus Müller
Georg-August-Universität, Göttingen

Prof. Dr. Claudia Steinem
Georg-August-Universität, Göttingen

Dr. Johannes Söding
Max Planck Institute for Multidisciplinary Sciences, Göttingen

Prof. Dr. Christian Griesinger
Max Planck Institute for Multidisciplinary Sciences, Göttingen

Dr. Andreas Neef
Göttingen Campus Institute for Dynamics of Biological Networks, Göttingen

Date of Oral Examination: 13th April, 2023

Abstract

Potassium (K^+) channels contribute to diverse physiological activities, representing an indispensable part of living organisms. A thorough understanding of different aspects of permeation mechanisms and gating in K^+ channels is of crucial importance.

Since only static information can be inferred from the available high-resolution structures of K^+ channels, the dynamical nature of ion permeation calls for a systematic investigation into the collective behavior of ions during permeation using computer simulations. In the first part of the thesis, we use molecular dynamics simulations and Markov state models to obtain dynamical details of multi-ion permeation processes in the selectivity filter. The permeation cycles representing ion permeation events reveal the dominance of the water-free direct knock-on permeation mechanism over a wide range of salt concentration, temperature, and transmembrane voltage for MthK. Other potassium channels with a highly conserved selectivity filter also demonstrate direct knock-on. Finally, charge strength dependence of permeation cycles was explored. The results illustrate the robustness of direct knock-on and shed light on the dynamical aspect of details in ion conduction, providing valuable insights into the conduction mechanisms in potassium channels.

The second part of the thesis delves into the possibility of channel gating via switching between two conformations. TREK-2 responds to a wide range of stimuli, such as pH, membrane tension, and binding of small ligands. The crystallographic up and down conformations have been resolved, where their main difference lies in the position and orientation of the transmembrane helix M4. However, molecular explanations for gating mechanisms and whether transitions between these two conformations play an essential role in gating remain elusive. Here, we use molecular dynamics simulations and free energy calculations to determine how the equilibrium between the up and the down conformations of TREK-2 is shifted by mutations. Mutants that exhibit considerable shifts away from the down state are identified. Most conformational shifts due to mutations can be attributed to induced steric clashes or weakened favorable interactions in the cytoplasmic part of M2, M3, and M4. These findings are in excellent agreement with functional analysis and NFx inhibition measurement of TREK-1 WT and mutants, unraveling the molecular roles of the identified residues in governing transitions between the two conformations and suggesting that conformational switching between the up and down states is a viable gating mechanism for TREK-1 and TREK-2.

Acknowledgment

I express my sincere gratitude to my advisor Prof. Bert de Groot for his guidance and support. I am privileged to complete my PhD in a highly regarded research group, pursuing science professionally with fun. I enjoy and appreciate the autonomy in a worry-free environment when conducting my research. At the same time, I receive instant support from Bert when I need it. He is a role model when it comes to supervision and mentorship.

I thank my thesis committee members Prof. Marcus Müller and Prof. Claudia Steinem for their valuable time and suggestions on improving my thesis from different perspectives. I thank Marcus Schewe, Marianne Musinszki, and Thomas Baukrowitz for contributing to our K2P channel project. It is exciting and rewarding to take part in interdisciplinary research. I thank Wojciech Kopec for advice on ion channel simulations and Vytautas Gapsys for suggestions on free energy calculations. They have demonstrated what a professional scientist is like. I thank Ansgar Esztermann, Martin Fechner, and Carsten Kutzner for solving all software and hardware issues. I thank Petra Kellers, Antje Erdmann, Frauke Bergmann, Eveline Heinemann, and Stefanie Teichmann for helping me with administrative work and making my life in Göttingen much easier. I thank all group members, including Dirk Matthes, Chenggong Hui, Andrei Mironenko, Benjamin Eltzner, Olga Rogacheva, Reinier de Vries, Edward Mendez-Otalvaro, Carter Wilson, Lisa Schmidt, Ricarda Kuntze, Yuriy Khalak, Ruo-Xu Gu, Martin Werner, and Csaba Daday, and all department members for maintaining a friendly and supportive atmosphere.

I thank my friends for the fun time we have. Last but not least, I thank my family and my girlfriend Elise Leung for their unconditional love, support, and tolerance.

Contents

1. Introduction

1.1. Overview of Potassium Channels

Potassium (K^+) channels are involved in numerous physiological functions, including neurotransmission, neuronal coding of information, heart beating, muscle contraction, and hormone secretion, via mediating potassium transport across cell membranes to regulate the electrical membrane potential [1, 2]. Malfunctions of these channels due to gene mutations and altered functional regulation lead to cardiac [3, 4], renal [5], pancreatic [6], and neuronal diseases [7]. As a result, much effort has been made to understand how potassium channels work.

K^+ channels are classified into three major classes: the voltage-gated (Kv), inwardly rectifying (Kir), and tandem pore domain (K2P) channels [8]. Most channels contain a pore domain and regulatory domains, except for channels such as KcsA which contains only a pore domain. The pore domain provides a direct passage of K^+ across membrane bilayers. They are usually arranged in a four-fold symmetric configuration with the permeation pathway located at the symmetry axis. The regulatory domains are responsible for sensing stimuli and inducing conformational changes of the channel to regulate ionic fluxes through the pore [9]. MthK is a calcium-activated K^+ channel. The full structure of MthK consists of a pore domain and a regulatory domain called the gating ring (Figure 1) [10]. Calcium ions bind to the eight RCK domains, which are located in the gating ring, and induce conformational changes in the gating ring, thereby opening the gate [11, 12].

1.1.1. Selectivity Filter

The selectivity filter (SF) is a critical component in the pore-forming domain. It represents the narrowest section of the conduction pathway taken by permeant K^+s. The SF is typically formed by four subunits with part of the amino acid sequence being TxGYG, a highly conserved motif in K^+ channels [9]. In four-fold symmetrical K^+ channels such as KcsA, MthK, and NaK2K, the sequence TVGYG constitutes the SF. In K2P channels such as TRAAK, TREK-1, and TREK-2, the SF is formed by two subunits, SF1 and SF2, with sequence TIGYG and TVGFG, respectively (Figure 2). There are four major binding sites in a canonical SF, S1, S2, S3, and S4. In addition, two extra binding sites, S0 and Scav, are connected to the passage to the extracellular and intracellular sides,

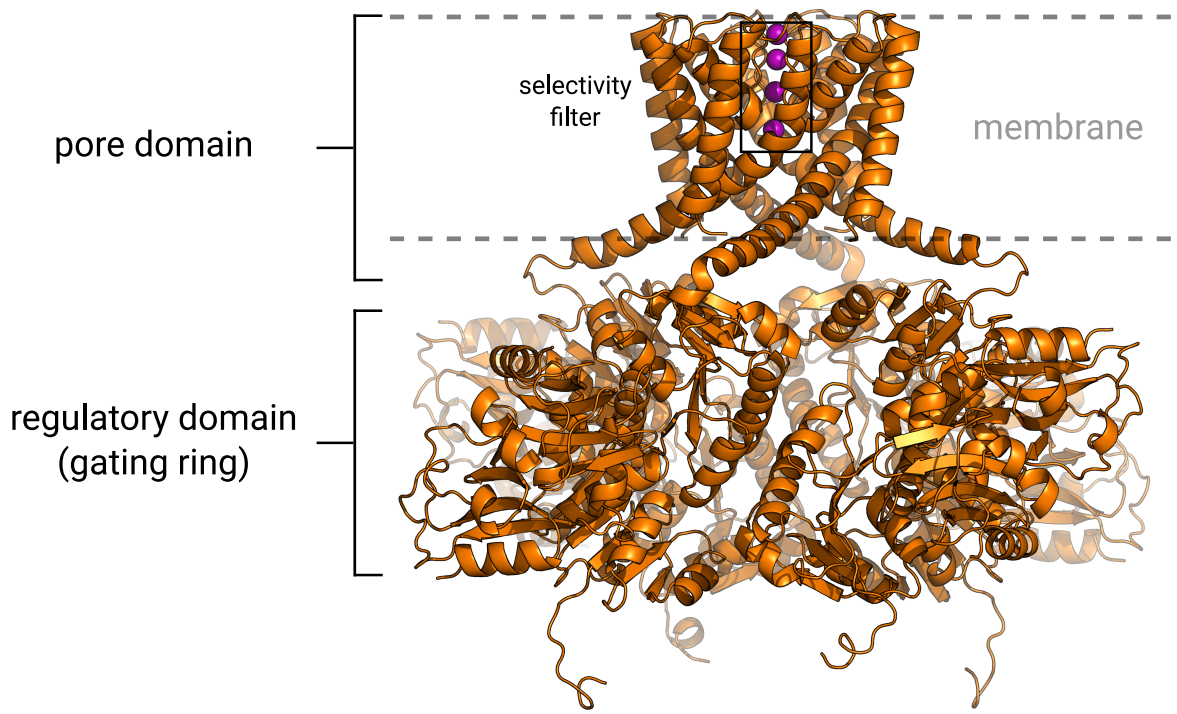

Figure 1: Structure of full-length MthK (PBD ID: 6OLY). K^+ ions in the SF are in purple.

respectively. The binding sites compensate K^+ for the loss of solvation when K^+ ions enter the SF. The backbone carbonyl oxygen atoms of the SF residues form S0, S1, S2, and S3. Backbone carbonyl oxygen atoms and sidechain hydroxyl oxygen atoms from four threonines represent S4. S4 and Scav share the sidechain hydroxyl oxygen atoms. The geometry of the SF plays a crucial role in determining the conduction properties of K^+ channels. For instance, single channel electrophysiology for the wild type and mutants of the non-selective NaK channel shows that only NaK2K, the mutant having a SF with four binding sites, exhibits selectivity of K^+ over Na^+. The channels with only two or three SF binding sites are not selective and allow Na^+ and K^+ permeation at a comparable rate [13].

1.1.2. Permeation Mechanisms

The highly conserved SF prompts the question of the universal permeation mechanism in K^+ channels. KcsA was the first K^+ channel with its structure resolved [14]. A full electron density was found in all four SF binding sites, S1 to S4. As full ion occupancy was thought to be electrostatically unstable, the occupancy of the SF was then explained as a superposition of two water-ion alternating configurations (W-K-W-K and K-W-K-

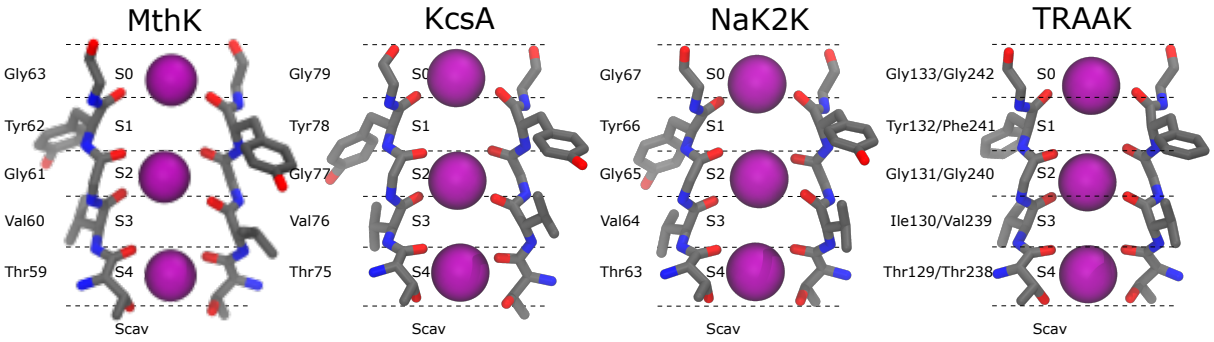

Figure 2: SF of MthK, KcsA, NaK2K, and TRAAK. Only two diagonal subunits are shown for clarity.

W) [14, 15]. Since then, the mechanism by which ion passes through the SF has been believed to be water-mediated and involve water co-permeation in a 1:1 ratio. Such a permeation mechanism was termed soft knock-on. A computational study based on molecular dynamics simulations revealed that configurations with close ion contact were energetically possible [16]. In 2015, A direct observation of the water-free direct knock-on permeation, driven by ion-ion head-on collisions, in molecular dynamics simulations of KcsA was reported, challenging the traditional view of the ion conduction mechanism [17].

Recent experimental measurements support direct knock-on more often than soft knock-on [18]. Solid-state nuclear magnetic resonance (ssNMR) spectroscopy reveals the absence of water in S3 and S4 of NaK2K [19]. Having no canonical voltage-sensing domain, K2P can be activated by having 3 to 4 ions in the SF, suggesting that a conductive SF is occupied by a high number of ions [20]. Full ion occupancy in S1 to S4 was identified with single-wavelength anomalous dispersion X-ray diffraction in TREK-1 [21] and NaK2K [22]. However, two-dimensional infrared spectroscopy suggests that soft knock-on and direct knock-on are possible [17]. Interpretation of streaming potential experiments favors the soft direct-on mechanism [23, 24, 25]. As a consensus on the dominant ion permeation mechanism has not been completely reached, more work is needed to understand the dominant ion permeation mechanisms under different physiological conditions.

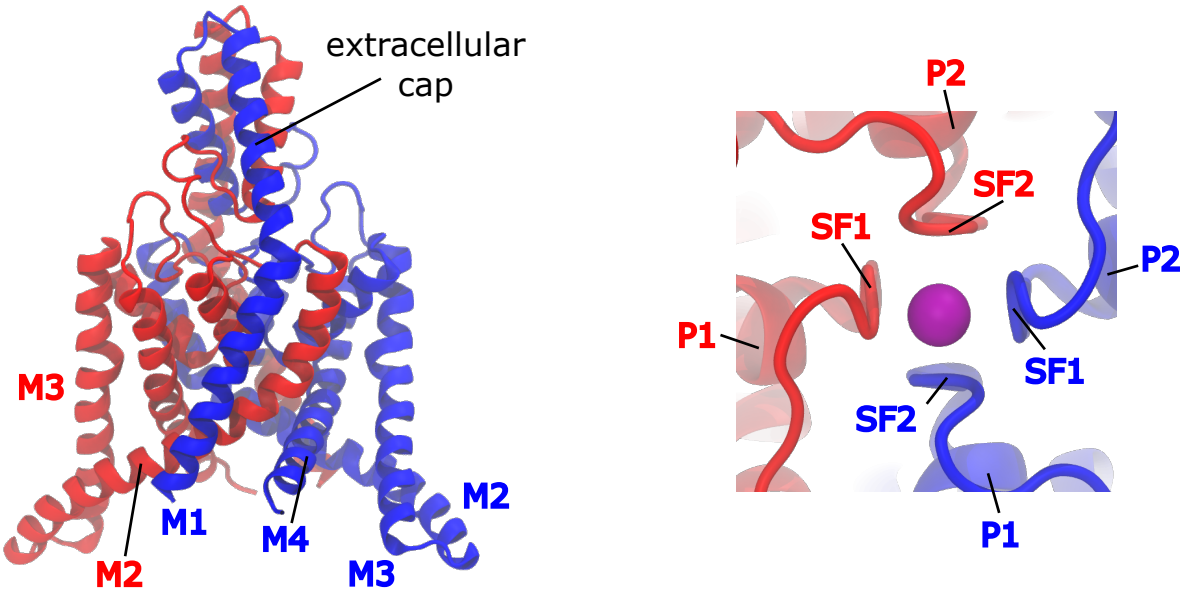

Figure 3: Side and top (excluding extracellular cap) view of TREK-2. Two subunits are colored in red and blue, respectively.

1.2. K2P Channels

1.2.1. Structural Characteristics

Unlike Kv and Kir channels that assemble as tetramers, K2P channels have a homodimeric arrangement. There are two asymmetric pore domains, PD1 and PD2, each containing a pore helix (P1 or P2) and a selectivity filter (SF1 or SF2) that are flanked by two transmembrane helices (M1-M2 or M3-M4). The asymmetry of PD1 and PD2 gives rise to different SF signature sequences for SF1 and SF2 in K2Ps. For example, the sequence for SF1 and SF2 in TREK-2 are TIGYGN and TVGFGD, respectively [1, 26]. It implies that a K2P channel is the product of two PD1s and two PD2s assembled as a dimer around the central axis, having a pseudo-fourfold symmetry (Figure 3). The K2P homodimeric architecture enables pinching and dilation of SF to be observed under low potassium concentrations in computer simulations [21]. Nevertheless, such a SF retains the conductive properties of the selectivity filters found in other homotetrameric potassium channels [27, 28, 29, 30]. There is a helical extracellular cap linking M1 and P1 [1, 26]. The cap forces a bifurcated extracellular pathway for potassium and is believed to block toxins from binding to the extracellular entrance of the pore [27, 31].

1.2.2. Sensitivity to Stimuli

K2P channels are sensitive to diverse classes of stimuli for physiological regulation. All K2P channels except K2P13.1 (THIK-1), K2P12.1 (THIK-2), and K2P18.1 (THESK) can be regulated by pH. Due to the presence of a pH sensor in the C-termini, K2P2.1 (TREK-1) and K2P 10.1 (TREK-2) are activated by intracellular acidification [32]. In contrast, TREK-2 is activated and TREK-1 is inhibited by low extracellular pH. This opposite response to extracellular acidification can be attributed to the altered electrostatic interactions between a conserved histidine (H126 and H151 for TREK-1 and TREK-2, respectively) that acts as a proton sensor and the residues, located in the P2M4 loop, that are positively and negatively charged in TREK-1 and TREK-2, respectively [33, 34]. TRAAK, TREK-1, and TREK-2 are mechanosensitive K2P channels modulated upon applying mechanical forces. In TREK-1, deletion of a charged region in the C-terminus abolishes its sensitivity to arachidonic acid (AA) and laminar shear stress, suggesting an essential role of M4 in chemical and mechanical activation [35]. Removal of the C-terminus of TREK-2 similarly renders the channel insensitive to fatty acids and intracellular pH and reduces the sensitivity to mechanical forces [36].
Despite the modest size of K2P ($\sim$70 kDas), they demonstrate the ability to be modulated by classes of modulators that bind in different sites of the channels. An L-shaped pocket behind the SF of TREK-1 in the P1-M4 interface was found to be a binding site for two activators, ML335 and ML402. The two molecules act as molecular wedges to reduce the motion of the P1-M4 interface and activate the C-type gate [28]. Inhibitors, such as fluoxetine and norfluoxetine (NFx) [29], can bind to a side fenestration site that is exposed when the channel is in the 'down' conformation. It is believed that the two inhibitors influence the channel activity by influencing the C-type gate conformational dynamics allosterically. A class of negatively charged activators (BL-1249, PD-118057, and NS11021) that bind below the SF were also reported [37]. These demonstrate the remarkable druggability of K2P channels.

1.2.3. 'Up' and 'Down' Conformations

Two conformations of TREK-2, termed "up" and "down", respectively, were resolved by X-ray crystallography. The main difference between the two conformations lies in the cytosolic parts of the M2, M3, and M4 helices [29]. In the "up" conformation, M4 is kinked

and hinged around a conserved glycine (GLY312) and moves further toward the membrane bilayer. Hinges at GLY201/GLY206 and GLY248 are also present in M2 and M3 of the TREK-2 "up" conformation, respectively. On the contrary, M4 is relatively straight and does not form extensive contact with M2 of another subunit in the "down" conformation. Analogous "up" and 'down' conformations that share many common structural features with the two TREK-2 conformations were also resolved for TRAAK [38].

While all four binding sites in the SF of the TREK-2 up conformation were found to be occupied by K^+s, K^+s were only observed in S2, S3, and S4 of the down crystal structure. As a result, it was believed that the up conformation represented an open, conductive state while the down conformation represented a closed, nonconductive state [39]. Furthermore, a lipid acyl chain was found in the central cavity of TRAAK in the down conformation. This finding gave rise to a novel hypothesis that K2P channels might gate via lipid blocking as a lipid was accessible to the central cavity when the channel was in the down conformation [38]. However, more evidence suggests that both conformations are conductive. First, an unobstructed path via the SF for ions is present in both conformations. Molecular dynamics simulations confirmed that both conformations are conductive. The down conformation is less conductive than the up conformation due to an increased probability of carbonyl oxygen flipping at the SF, rendering the channel nonconductive until the canonical position of the carbonyl oxygen is restored [40]. Functional experiments also revealed the existence of more than one open state for TREK-2, and channel activation cannot be simply attributed to switching between the up and the down conformations [41], and the open state retains the sensitivity to norfluoxetine [42], suggesting that both the up and down conformations contribute to the open states.

When TREK-2 adopts the up conformation, two fenestration sites below the SF are blocked by the side chains of PHE316 and LEU320 of M4, making the two sites inaccessible to inhibitors such as fluoxetine and norfluoxetine [29, 43, 42]. These conformation-selective inhibitors can therefore be used to study the conformational preference of K2P.

1.2.4. Gating Mechanism Hypotheses

Kvs [44] and Kirs [45] gate via dilation of their "lower" gate at the cytoplasmic entrance to the SF. This mechanism, however, is not adopted by K2Ps. It has been well established

that the C-type gate, also called SF gate, is the primary gate for K2P channels [46, 20]. For instance, quaternary ammonium (QA) ions bind freely and strongly to the binding sites of SF of TREK-1 even before intracellular pH or pressure activation, suggesting that the "lower" gate of TREK-1 is constitutively open. At the same time, mutations close to the SF and the physical properties of the permeant ions critically determine the channel gating of TREK-1. As a result, the primary gate locates at or close to the SF, and the "lower" gate is not involved in gating.

A hypothesis reconciling the identification of SF being the primary gate and the possibly functionally relevant up and down conformations of TRAAK and TREK-2 is that the motion of M4 interpolated between the two conformations is coupled to the dynamics of the SF [21, 28, 40, 47]. However, whether gating via conformation switching between the two conformations is adapted by K2Ps remains to be established.

1.3. Electrophysiology

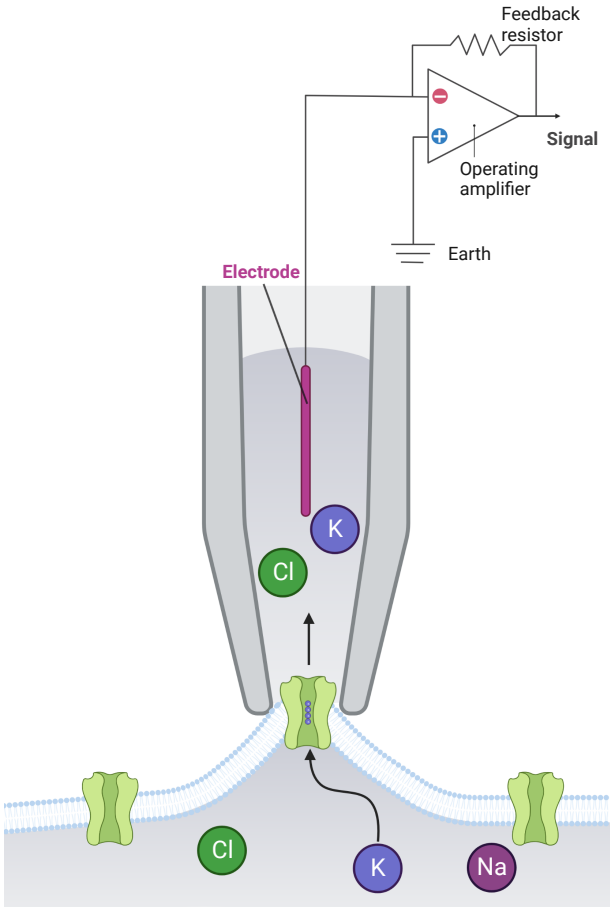

Figure 4: Cell-attached configuration for patch clamp technique.

The patch clamp technique is a widely used experimental method to measure electrophysiological properties of membranes and ion channels [48]. This section briefly describes the patch clamp technique for measuring the conduction properties of K^+ channels.
The cell-attached configuration in Figure 4 is the most common configuration in patch clamp technique [49]. First, the tip of a pipette is pressed against the surface of a cell. A slight negative pressure is then applied to suck and seal the contact point between the pipette and the cell, forming a "Ω"-shaped protrusion. The seal is sufficiently tight such that the leak current through the glass-membrane interface is small and can be subtracted to obtain a corrected measurement of currents through the channels embedded in the membrane segment. After the cell-attached configuration is established, additional procedures may be executed to obtain one of the three configurations, whole-cell, outside-out, and inside-out, which are better suited to different scenarios. For instance, in the outside-out configuration, the pipette is sealed against a small membrane segment whose extracellular side is exposed to the bath solution, making this configuration useful for measuring ion channels gated by extracellular ligands. By recording the detected current, one can obtain a graph of channel recording (current as a function of time) from which many conduction properties, such as the conductance and the existence of multiple conductive and non-conductive states, can be deduced.

2. Aim and Organization of the Thesis

This thesis aims to contribute to understanding conduction properties in potassium channels using molecular dynamics simulations. An overview of potassium channels, ion conduction mechanisms, and the patch clamp technique for measuring channel activities is given in Chapter 1. Methods, including molecular dynamics simulations, free energy calculation, and Markov state modeling, used in the study are introduced in Chapter 3. Next, the first project, which is dedicated to investigating multi-ion dynamics and permeation mechanisms in the selectivity filter of potassium channels, is presented in Chapter 4. We devise an analysis framework for systematically comparing permeation details in the selectivity filter and discover that the dominant permeation mechanism is water-free and largely invariant for different simulation conditions. The second project, which aims to establish the hypothesis that conformational changes in the transmembrane helices serve a gating mechanism in TREK-2, is summarized in Chapter 5. In collaboration with a research group specialized in experimental electrophysiology, we identify residues in TREK-1 and TREK-2 sensitive to channel gating. Our results represent strong evidence supporting the hypothesis of conformational switching as a gating mechanism in K2P channels.

Finally, the conclusions and outlook of the projects are given in Chapter 6 and 7, respectively. Supporting information for the two projects can be found in Appendices A and B.

3. Theory

3.1. Molecular Dynamics Simulations

3.1.1. Equations of Motion

Understanding of dynamics of biomolecules is often required to explain their molecular mechanisms. Molecular dynamics (MD) simulations are a method to predict the motions of biomolecules, such as protein-ligand binding and protein folding, using computer simulations [50, 51]. A short introduction to atomistic MD simulations is given here.
The Born–Oppenheimer approximation states that the total wave function can be decomposed into the wave function for nuclei (Ψ_n) and the wave function for electrons (Ψ_e), which can be treated separately:

$$\Psi_{\text{total}} = \Psi_n * \Psi_e. \tag{1}$$

As the electrons have a much lighter mass than nuclei, the nuclei can be considered stationary when solving the electronic wave function. Therefore, $\Psi_e(\vec{r}, \vec{R})$ can be obtained by solving the Schrödinger equation for all electronic configurations $\vec{r}$ and a given nuclei configuration $\vec{R}$ [52].
We assume that the electrons are always in the ground state and do not involve in the molecular processes, and the molecular processes can be fully described in terms of the coordinates of atoms. In MD simulations, the coordinates of atoms are determined by solving Newton's equations of motion:

$$m_i \frac{d^2\vec{r}_i}{dt^2} = \vec{F}_i, \quad i = 1, 2, ..., N, \tag{2}$$

where m_i, $\vec{r}_i$, are the mass and position of atom i, and $\vec{F}_i$ is the force acting on atom i at time t.
Since analytical solutions are generally unavailable, numerical integration is performed to calculate the atomic coordinates at every time t. An example of a numerical integration algorithm is leapfrog integration:

$$\vec{v}_{i,t+\frac{\Delta t}{2}} = \vec{v}_{i,t-\frac{\Delta t}{2}} + \frac{\vec{F}_i}{m_i}\Delta t \tag{3}$$

$$\vec{r}_{i,t+\Delta t} = \vec{r}_{i,t} + \vec{v}_{i,t+\frac{\Delta t}{2}}\Delta t, \tag{4}$$

where Δt is the size of each time step and $\vec{v}_{i,t+\frac{\Delta t}{2}} = \frac{\partial \vec{r}_{i,t+\frac{\Delta t}{2}}}{\partial t}$ is the velocity of atom i evaluated at time $t + \frac{\Delta t}{2}$. Δt should be small enough to resolve the fastest motion in the simulation system. For biomolecular systems, the fastest vibrations are usually represented by the oscillations of bonded hydrogen atoms. To eliminate such oscillations, which are usually irrelevant to the biophysical problems in hand, and to create a more accurate physical representation of the hydrogen atoms which are exclusively in the vibrational ground state, holonomic constraints are applied to the associated atoms [53]. It allows an increase in Δt from typically ∼1 fs to 2 fs. Additional techniques, such as increasing the mass of hydrogen atoms and introducing dummy atoms to replace hydrogen atoms, can also be used to speed up the simulations by increasing Δt [54].

3.1.2. Force Fields

A force field determines most terms in $\vec{F}_i$. An empirical force field, such as AMBER [55], and CHARMM [56, 57] force fields, consists of an empirical potential energy function with parameters, which together define the interactions between atoms [58]. A common, minimal form of the potential energy function $U(\vec{r}_1, \vec{r}_2, ..., \vec{r}_N)$ is

$$\begin{aligned} U(\vec{r}_1, \vec{r}_2, ..., \vec{r}_N) = &\sum_{bonds} K_b(b - b_0)^2 + \sum_{angles} K_\theta(\theta - \theta_0)^2 + \\ &\sum_{dihedral} K_\phi\Big(1 + \cos\left(n\phi - \delta\right)\Big) + \sum_{impropers} K_\psi(\psi - \psi_0)^2 + \\ &\sum_{atoms, i<j} \left[\epsilon_{ij}\left((\frac{A_{ij}}{r_{ij}})^{12} - (\frac{B_{ij}}{r_{ij}})^6\right) + \frac{q_i q_j}{4\pi\epsilon_0 r_{ij}}\right]. \end{aligned} \tag{5}$$

Bond lengths b, bond angles θ, and out-of-plane bending (quantified by improper dihedral angles ψ) are modeled by harmonic functions. Dihedral angles ϕ are treated using a sinusoidal function. Van der Waals (VdW) interactions between two atoms are described by a Lennard-Jones potential. Electrostatic interactions are calculated using Coulomb's law. Parameters may be obtained by optimizing against reference values from quantum mechanical (QM) calculations. In Amberff99sb, parameters associated with dihedral angles for protein were based on fitting conformational energy of glycine and alanine tetrapeptides from ab initio QM calculations [59]. In Amberff14sb, some parameters for the backbone dihedral angles in amino acid were optimized to achieve high agreement between NMR

and MD simulations for short alanine peptides [55]. Given a potential energy function $U(\vec{r}_1, \vec{r}_2, ..., \vec{r}_N)$, $\vec{F}_i = -\nabla U(\vec{r}_1, \vec{r}_2, ..., \vec{r}_N)$ can be computed.

3.1.3. Long-range Interactions

Direct calculation using Equation 5 for the whole system leads to a quadratic computation complexity $O(N^2)$, rendering the simulations unscalable to large biomolecular systems. Thanks to the quickly decaying r^{-6} dependence of the vdW interactions, it is possible to compute the interactions only for atom pairs whose separation is shorter than a cut-off distance. For the Coulomb interactions, the Particle mesh Ewald (PME) algorithm is usually employed [60]. The PME algorithm decomposes ionic interactions into short-range and long-range contributions. The short-range contribution is calculated by adding all Coulomb interaction pairs in real space, while the long-range contribution is calculated with a Fourier transformation as the equivalent sum of interaction terms converges much more quickly in Fourier space than in real space. By treating the long-range molecular interactions differently, the calculation of forces acting on every atom, which represents the most computationally intensive step in MD simulations, can be reduced from $O(N^2)$ to $O(N \log N)$ and becomes feasible for large systems.

3.1.4. Thermostats and Barostats

Simulating the system under constant pressure and temperature is desirable to match physiological conditions. Algorithms termed thermostats and barostats that regulate the temperature and pressure, respectively, are used during the simulations to obtain the NPT (constant number of atoms N, pressure P, and temperature T) ensemble. For instance, velocity rescaling is a thermostat that properly rescales velocities of atoms to generate the canonical distribution at a given temperature [61]. The Berendsen thermostat works by introducing stochastic and friction terms into the equations of motion to couple the system to an external heat bath with a fixed reference temperature value T_0, yielding the relation

$$\frac{dT}{dt} = \frac{T_0 - T}{\tau_T}, \tag{6}$$

where τ_T is the temperature coupling time constant. The change in temperature is realized by scaling the velocity of atoms by the factor

$$\lambda = [1 + \frac{\Delta t}{\tau_T}(\frac{T_0}{T} - 1)]. \tag{7}$$

Analogously, the Berendsen barostat controls the pressure via

$$\frac{dP}{dt} = \frac{P_0 - P}{\tau_P}, \tag{8}$$

where τ_P is the pressure coupling time constant. Assuming the system is isotropic and confined in a cubic box, the pressure can be achieved by scaling the coordinates so that the box lengths extend or shrink by the factor

$$\mu = [1 - \frac{\Delta t}{\tau_P}(P_0 - P)]^{1/3} \tag{9}$$

[62]. It is recommended to use the force field with the thermostat and barostat suggested by the force field developer to avoid undesirable artifacts.

3.1.5. Periodic Boundary Conditions

To reduce finite-size artifacts and surface effects which adversely affect the interpretability of the results, periodic boundary conditions are usually implemented, allowing the simulated system to interact with its first images to mimic an infinitely large system. Atoms moving across a periodic boundary will "appear" on the opposite side of the box.

3.1.6. Limitations

Conventional MD simulations allow direct observation of rare events, such as conformational changes in proteins. However, insufficient sampling due to the timescale of motions of interest exceeding the simulation timescale hampers it. For instance, in Section 5, the transitions between the up and the down states of TREK-2 are experimentally estimated to be on the millisecond timescale, while conventional MD simulations are only up to the microsecond timescale. As a result, it is not feasible to calculate the free energy difference between the two states for different mutants only by estimating the ratio of their populations using conventional MD simulations. To overcome this challenge, free

energy calculations, which are an enhanced sampling technique and will be explained in Chapter 3.3, were employed. Another way of simulating a larger system with a longer simulation time is to use a more simplified system representation. Using a coarse-grained model, including MARTINI [63], simulations of large-scale systems such as realistic cell membranes become more feasible [64].

Empirical atomistic force fields by no means represent the true details of the molecular interactions in the system. One may carry out quantum mechanical calculations at the expense of computational resources to obtain a more accurate description of the system. While empirical atomistic force fields have demonstrated their ability to unravel molecular mechanisms at an affordable cost, uncertainty in the force fields makes the interpretation of the results difficult. For instance, as illustrated in Chapter 4, Amber14sb and CHARMM36m force fields result in quantitatively different permeation processes. The differences can be attributed to the uncertainty in the parameterization of the force fields and the limited ability to describe molecular interactions using simplified physical models.

3.2. Ion Permeation in MD Simulations

Analogous to experimental electrophysiology, one can perform *in silico* electrophysiology, simulating ion permeation processes through potassium channels using MD simulations. MD simulations of ion permeation are appealing as they provide atomistic and dynamical details of channels and permeant ions, which are not accessible simultaneously by current experimental techniques. It is desirable to generate a continuous flow of ions through the channel in MD simulations that mimic the experimental conditions for direct comparison between simulations and experiments.

3.2.1. Computational Electrophysiology

Unidirectional flow of ions in MD simulations can be accomplished by computational electrophysiology [65, 66]. In computational electrophysiology, an ion concentration imbalance is first established across two compartments separated by two lipid bilayers. Thanks to the concentration gradient, which in turn is typically accompanied by a gradient in electrostatic potential, there is a net ion flow across the compartments through the channel. Ions are swapped between the compartments using a non-equilibrium Monte Carlo method to

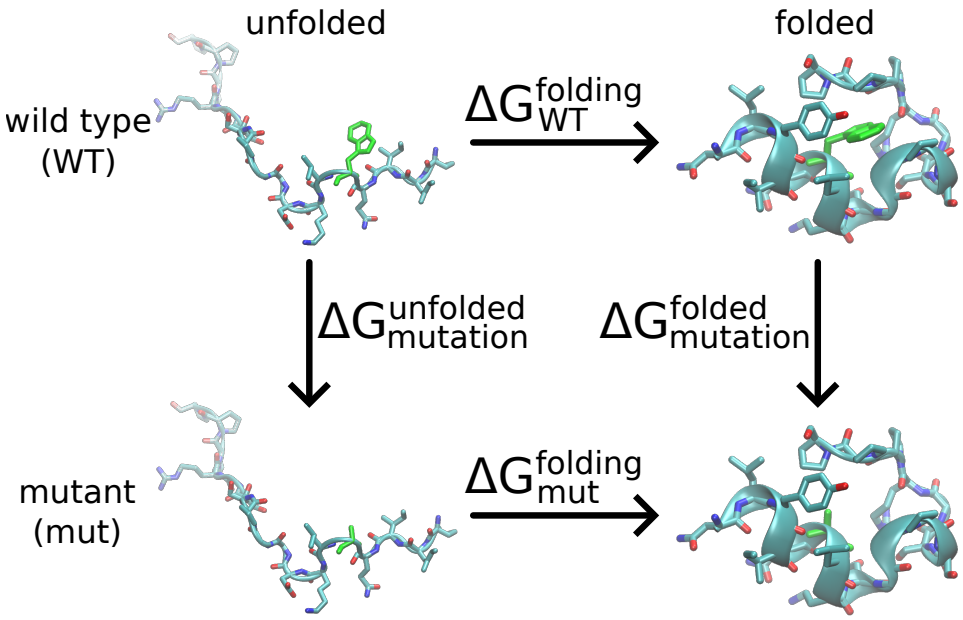

Figure 5: Thermodynamic cycle for determination of folding free energy.

maintain the steep ion gradient for steady ionic fluxes throughout the simulation.

3.2.2. External Electric Field

Another way of generating net ionic fluxes is to apply an external electric field. It has been shown that a transmembrane voltage V can be induced by applying an electric field $E = \frac{V}{L}$ in the direction of membrane normal, where L is the length of the simulation box along the membrane normal [67]. This method is sometimes more practical as computational electrophysiology requires a double-bilayer setup which is often more challenging to construct, and both approaches yield practically indistinguishable results [68]. As a result, ion permeation events in Chapter 4 were generated by applying an external electric field to a potassium channel embedded in a single bilayer.

3.3. Non-equilibrium Alchemical Free Energy Calculations

Accurate determination of free energies is crucial for obtaining a thorough understanding of molecular processes, contributing to the development of drug design and discovery [69], and understanding of protein thermostability [70]. Here, a short introduction to MD-based non-equilibrium alchemical free energy calculations is given.

3.3.1. Alchemical Transformation

It is often sufficient to calculate only the relative free energy $\Delta\Delta G$ as far as only the relative free energy difference between two thermodynamic states is concerned [69]. Consider the thermodynamic cycle in Figure 5, knowing the folding free energy of a mutant relative to the wild type ($\Delta\Delta G = \Delta G^{\text{folding}}_{\text{mut}} - \Delta G^{\text{folding}}_{\text{WT}}$) is sufficient to rank the destabilization caused by mutation for multiple mutants. Thanks to the thermodynamic cycle, one can instead calculate $\Delta\Delta G$ via a non-physical (alchemical) path by morphing the relevant residue into the target residue and calculating the difference between the mutational free energies $\Delta\Delta G = \Delta G^{\text{folded}}_{\text{mutation}} - \Delta G^{\text{unfolded}}_{\text{mutation}}$, where $\Delta G^{\text{folded}}_{\text{mutation}}$ and $\Delta G^{\text{unfolded}}_{\text{mutation}}$ are the mutational free energy for the folded state and unfolded state, respectively. This way, a difference in folding free energy can be calculated without having to sample the cumbersome folding/unfolding pathway.

3.3.2. Non-equilibrium Free Energy Calculations

The calculation of mutational free energies can be carried out by simulating the amino acid transformation reversibly (equilibrium), theoretically infinitely slowly ($\tau \to \infty$), or irreversibly (non-equilibrium), completing in a finite time τ. Jarzynsky's inequality

$$\langle e^{-\beta W(\tau)} \rangle = e^{-\beta \Delta G}, \tag{10}$$

where $\beta = \frac{1}{k_B T}$ is the reciprocal of Boltzmann constant times temperature, provides a means to determine the equilibrium free energy difference ΔG between the two states using the average of non-equilibrium work values W when carrying the transformations irreversibly. Unlike Jarzynsky's inequality which considers only transformations in one direction, Crooks fluctuation theorem takes into account the irreversible transitions in both forward and backward directions:

$$\frac{P_f(W(\tau))}{P_b(-W(\tau))} = e^{-\beta \Delta G}, \tag{11}$$

where $P_f(W)$ and $P_b(W)$ are the distributions of the forward and backward work values, respectively. A simple estimator for ΔG is

$$\widehat{\Delta G} = W(\tau) + k_B T \ln \frac{P_f(W\tau))}{P_b(-W\tau))}. \tag{12}$$

$\widehat{\Delta G}$ is given by the value of W where the two distributions intersect. However, since this requires a great overlap of the two distributions and long tails of distributions would contribute to large uncertainty, using an alternative, asymptotically unbiased estimator called Bennet's Acceptance Ratio (BAR) is preferred [71, 72]. The BAR estimator can be calculated by numerically solving

$$\sum_{i=1}^{N_f} \frac{1}{1 + \frac{N_f}{N_b} e^{\beta(W_i - \widehat{\Delta G})}} = \sum_{j=1}^{N_b} \frac{1}{1 + \frac{N_b}{N_f} e^{\beta(W_j - \widehat{\Delta G})}}, \tag{13}$$

where N_f and N_b are the number of forward and backward work values, respectively.

3.4. Markov State Modeling

Markov State Models (MSMs) are a powerful technique for extracting and resolving complex kinetic details in MD simulations, including folding of small proteins [73] and intrinsically disordered proteins [74]. Since only conditional probabilities are required to estimate the transition matrix of a MSM, multiple MD trajectories whose simulation length is much shorter than the timescale of motions of interest can be combined to reveal the molecular details [75]. This section provides a short introduction to discrete-time Markov chains, which jump at discrete time steps and have a countable set S for their state space.

3.4.1. Dimension Reduction

A discrete-time Markov chain constructed from MD simulations involves dimension reduction, projecting all degrees of freedom $(\vec{r}, \vec{v})$ in MD trajectories onto a finite number of states S_i. Time-lagged independent component analysis (TICA) allows one to obtain a set of states which are maximally separated in time, suitable for describing slow processes in an equilibrium system by transitions between the Markov states [76]. An analogous approach for non-equilibrium systems is a variational approach for Markov processes

(VAMP) [77]. Having the Markov states defined, MD trajectories can be expressed as time sequences of the states.

3.4.2. Estimation of Transition Matrices

From the observed sequences of the Markov states visited in the simulations, we can compute a N_S-by-N_S count matrix $\boldsymbol{C}(\tau)$, where N_S is the number of Markov states, and $C_{ij}(\tau)$ is the number of transitions from state S_i to state S_j observed after a lag time τ. To reduce the amount of data discarded due to $\tau > \Delta t$, where Δt is the size of the time step of the simulations, a sliding window approach of width τ, where the original sequence is split into sequences such as $\Big[S(t) \rightarrow S(t+\tau) \rightarrow S(t+2\tau) \rightarrow ... \Big]$ and $\Big[S(t+\Delta t) \rightarrow S(t+\Delta t+\tau) \rightarrow S(t+\Delta t+2\tau) \rightarrow ...\Big]$, may be used. However, this would lead to errors in the estimation of $\boldsymbol{C}(\tau)$ if these split sequences are not statistically independent.

The transition matrix $\boldsymbol{T}(\tau)$, where $T_{ij}(\tau)$ is the probability of visiting S_j after τ given that the system is currently in S_i, is central to a MSM as all stationary and kinetic properties are encoded in it. A simple maximum likelihood estimator is $\hat{T}_{ij} = \frac{C_{ij}}{\sum_j C_{ij}}$ [75].

3.4.3. Validation of Markov State Models

The probabilities in $\boldsymbol{T}$ are only conditioned on the current state $S(t)$, assuming that the dynamics are 'memoryless' and the next state depends only on the current state but not the past. For this assumption to hold reasonably well, discretization of phase space into Markov states representing metastable states and a sufficiently long τ to let the system relax to get rid of the memory are needed. To evaluate how close the constructed MSM is to an ideal one, one can perform a so-called Chapman–Kolmogorov test [75], checking whether

$$\hat{\boldsymbol{T}}^k(\tau) \approx \hat{\boldsymbol{T}}(k\tau), \tag{14}$$

for $k = 1, 2, 3, ...$, holds. An example of the Chapman–Kolmogorov test is illustrated in Section 4. Markov Chain (MC) simulations based on the transition matrices derived from the MD simulations were performed, starting the system in one of the most frequently observed states and comparing the relaxation of the system for different values of τ. This is a harsh test as a sufficient sampling of transitions from and to the most frequently observed states is needed [75, 78].

4. Ion Conduction Mechanisms in Potassium Channels Revealed by Permeation Cycles

Abstract

Potassium channels are responsible for the selective yet efficient permeation of potassium ions across cell membranes. Despite many available high-resolution structures of potassium channels, those conformations inform only on static information of the ion permeation processes. Here, we use molecular dynamics simulations and Markov state models to obtain dynamical details of ion permeation. The permeation cycles, expressed in terms of selectivity filter occupancy and representing ion permeation events, are illustrated. We show that the direct knock-on permeation represents the dominant permeation mechanism over a wide range of potassium concentration, temperature, and membrane voltage for the pore of MthK. Direct knock-on is also observed in other potassium channels with a highly conserved selectivity filter, demonstrating the robustness of the permeation mechanism. Lastly, we investigate the charge strength dependence of permeation cycles. Our results shed light on the underlying permeation details, which are valuable in studying conduction mechanisms in potassium channels.

4.1. Introduction

Potassium (K^+) channels are present in almost all organisms, mediating K^+ fluxes during action potentials [79]. Most K^+ channels contain regulatory domain(s) and pore-forming domain(s), except for channels such as KcsA, which contains only the pore-forming domain [8]. The regulatory domains are responsible for sensing stimuli and inducing conformational changes in the channel to regulate ionic fluxes through the pore. The pore-forming domains provide a direct passage of K^+ across membrane bilayers (Figure 6A). Despite the structural variety of K^+ channels due to variations in their pore-forming domains and regulatory domains, the selectivity filter (SF), a component of the pore domain central to ion permeation, is highly conserved. A signature sequence TVGYG constitutes a SF with four-fold symmetry in K^+ channels such as KcsA, MthK, and NaK2K. Substitutions of V by I and Y by F in pore domain 1 (P1) and pore domain 2 (P2), respectively, are observed in K2P channels such as TRAAK and TREK-2 and lead to a two-fold symmetric SF. The SF forms the narrowest part of the channel and provides a conduction path to permeant ions. A canonical SF contains four main binding sites (S1, S2, S3, and S4) and two additional binding sites (S0 and Scav), which are exposed to the extracellular side and the cavity of the channel, respectively (Figure 6B). The binding sites provide coordination to K^+, compensating for the loss of solvation upon entering the SF. S0 to S3 are formed by the backbone carbonyl oxygen atoms of the SF residues. S4 is formed by the backbone carbonyl oxygen atoms and sidechain hydroxyl oxygen atoms from four threonines. Scav shares the sidechain hydroxyl oxygen atoms with S4. It has been shown that the conduction properties of K^+ channels are sensitive to the geometry of the SF. For instance, a study of the wild type (WT) and mutants of NaK channel demonstrated that the channels with two or three binding sites lost their selectivity to K^+ over Na^+ and only when four binding sites were present were the selectivity and permeation rate restored [13]. Structural plasticity is also needed to explain the efficient conduction of different ions in the non-selective channel NaK [80].

Because of the conservation of the SF, K^+ channels likely share the same or very similar permeation mechanisms. The debate about the permeation mechanisms in K^+ channels has lasted for at least one decade. The first KcsA structure revealed a full electron density in all four binding sites of its SF. The SF occupancy was interpreted as a superposition of two configurations KWKW and WKWK (for S1 to S4), as it was believed that K^+ in

direct contact would be electrostatically unfavourable [14, 15]. This interpretation naturally gave rise to the soft knock-on hypothesis for ion permeation. In the soft knock-on permeation, ions and water molecules move concertedly through the SF, achieving an ion-water permeation ratio of 1:1 [81]. However, molecular dynamics (MD) simulations showed that an alternative permeation mechanism that involves no water co-permeation is energetically possible [16]. A study consisting of extensive MD simulations and crystallographic measurements challenged the traditional view of the ion permeation mechanism, suggesting that direct knock-on, where ion-ion head-on collisions in the absence of water inside the SF are the primary driving force of ion permeation, is the dominant permeation mechanism in K^+ channels [17].

Even with the availability of high-resolution structures of K^+ channels, limited insights into the dynamical properties relevant to ion permeation can be gained from these static conformations. Advance in computational research enables us to extract detailed dynamical information about ion permeation at an atomistic scale to investigate the permeation mechanisms in K^+ channels. To this end, we used MD simulations and Markov state models (MSMs) to examine how the occupancy of the SF evolves during ion permeation under different conditions, including K^+ concentration, temperature, and membrane voltage. Additional simulations were carried out to identify variations in ion permeation patterns for different channels. Finally, we varied the charges of charged residues and ions to evaluate the dependence of the observed permeation patterns on the force field implementation. The MD trajectories, resulting in a total simulation time of 260 μs and thousands of K^+ permeation events, provide extensive dynamical information from which the underlying permeation processes were studied.

4.2. Methods

4.2.1. MD Simulations

The MthK system was adopted from the work by Kopec *et al* [82]. CHARMM-GUI [83, 56, 84] was used to embed the pore-only structure of MthK (PDB: 3LDC [85]), KcsA E71A (PDB: 5VK6 [86]), NaK2K F92A (PDB: 3OUF [13]), and TRAAK (PDB: 4I9W [87]) into a 1-palmitoyl-2-oleoyl-sn-glycero-3-phosphocholine (POPC) membrane bilayer. For NaK2K, the mutation F92A was performed using CHARMM-GUI. The systems were solvated and neutralized by KCl. Binding sites S1 to S4 of all channels were occupied

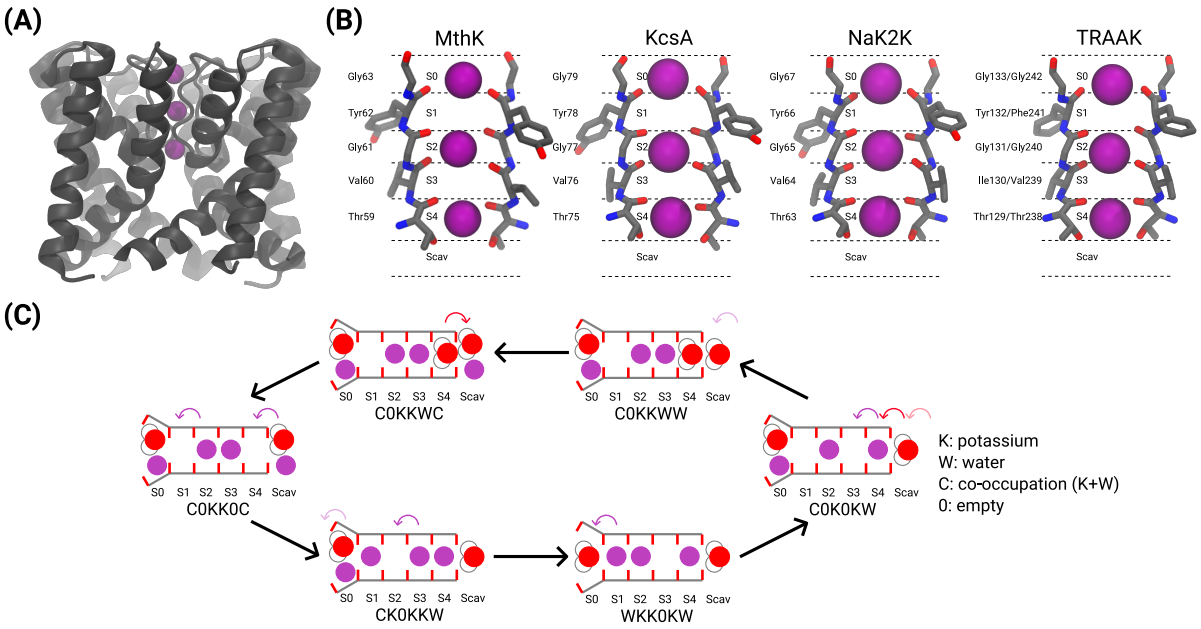

Figure 6: (**A**) Pore-only structure of MthK (PDB ID: 3LDC). (**B**) Selectivity filter (SF) of MthK, KcsA, NaK2K, and TRAAK. Each SF consists of six binding sites (S0 to Scav). Only two opposite subunits are shown for clarity. (**C**) Example of reduced permeation cycles.

by K^+ in the starting structures for the MD simulations. Two force fields, Amber14sb [55] and CHARMM36m [57] were used to model the systems. For Amber14sb, Berger lipids [88, 89], the TIP3P water model [90] and Joung and Cheatham ion parameters [91] were used. Aliphatic hydrogen atoms were replaced by virtual sites [54]. Combined with the use of LINCS algorithm [53], an integration time step of 4 fs was used for the Amber14sb simulations. A leap-frog algorithm was used as the integrator. The temperature was maintained using a velocity rescaling algorithm [61]. The pressure was kept at 1 bar using a semi-isotropic Berendsen barostat [62]. A cutoff of 1.0 nm was used for van der Waals interactions. The particle mesh Ewald (PME) algorithm [60] with a 1.0 nm distance cutoff was chosen to compute electrostatic interactions. For CHARMM36m, CHARMM36 lipids [92], CHARMM TIP3P water model [93] and CHARMM ion parameters [94] were used. The LINCS algorithm [53] was used to constrain all bonds associated with hydrogen atoms. An integration time step of 2 fs was used for all CHARMM36m simulations. A cutoff of 1.2 nm was used for van der Waals forces and the forces were switched smoothly to zero between 0.8 to 1.2 nm. The particle mesh Ewald (PME) method with a 1.2 nm distance cutoff was used for electrostatic interactions. The temperature was maintained using Nosé–Hoover thermostat [95, 96]. The pressure was kept at 1 bar

using Parrinello–Rahman barostat [97]. Simple harmonic distance restraints between the backbone oxygen atom of the i-th residue and the backbone hydrogen atom of the $(i+4)$-th residue for residues between ACE17 (N-terminal acetyl capping group) and VAL30 and between PHE87 and NME100 (C-terminal N-methyl amide capping group) within the same chain were applied to avoid unfolding of the two termini in each monomer. The equilibrium distance d_0 and the force constant k are 0.2 nm and 1000 kJ mol^{-1} nm^{-2}, respectively. An external electric field $E = \frac{V}{L}$, where V is the membrane voltage and L is the length of the simulation box in the z-direction, was applied along the z-axis. For charge scaling, the scaling factor q/q_0, where q is the scaled charge and q_0 is the default charge of the charged residues of MthK, K^+, and Cl^-, was applied. In the case of charged residues, q was achieved by adding an offset charge of $(q-q_0)/n_{\mathrm{nm}}$, where n_{nm} is the number of non-mainchain atoms of the residue, to all the non-mainchain atoms of the same residue. Also, as all partial charges were rounded to four decimal places, counter charges were added to C_β atoms to account for missing charges due to rounding to keep the simulation box neutral. All simulations were performed with GROMACS 2020 [98, 99]. A summary of the simulations can be found in Table S1, S2, S3, and S4.

4.2.2. Markov State Modeling and Permeation Cycles

The boundaries of the SF binding sites were defined by the z-coordinate of the center of mass (CoM) of the backbone carbonyl oxygen atoms or the hydroxyl oxygen atoms of residues of the SF. For instance, the upper boundary of S2 of MthK WT was defined by the z-coordinate of the CoM of the backbone carbonyl oxygen atoms from the four Gly61, as MthK is a tetramer. Similarly, the lower boundary of S2 was defined by the z-coordinate of the CoM of the backbone carbonyl oxygen atoms from the four Val60. In Figure 6B, S2 is occupied by a K^+, as a K^+ is found between the two boundaries of S2 and within 4 Å of the axis of symmetry of the SF. The upper boundary of Scav was formed by the hydroxyl oxygen atoms of four threonine residues, and the lower boundary of Scav was set to be 4 Å below its upper boundary. Using these definitions, we expressed the SF occupancy of each simulation snapshot using a six-character code, with each character representing the occupancy of one binding site. For the state C0K0KW in Figure 6C, since S0 is occupied by a potassium ion and a water molecule at the same time before the transition, C (**C**o-occupation) is assigned to the first letter. The second letter is 0, as

S1 is vacant. Letters K and W represent the occupation by a potassium ion and a water molecule, respectively. The resulting six-character code defines a SF occupation state.

The transition matrix $\boldsymbol{T}(\tau)$ of a Markov state model (MSM) using the SF occupation states was obtained via normalizing the count matrix $\boldsymbol{C}(\tau)$ by

$$T_{ij}(\tau) = \frac{C_{ij}(\tau)}{\sum_j C_{ij}(\tau)}, \tag{15}$$

where $T_{ij}(\tau)$ is the probability of transitioning from state S_i to state S_j, and $C_{ij}(\tau)$ is the number of transitions from state S_i to state S_j after a lag time τ observed in MD simulations.

Performing eigendecomposition on $\boldsymbol{T}$ yields eigenvalues λ_m and eigenvectors $\boldsymbol{\nu}_m$ that characterize the dynamical processes in the molecular system on different timescales [75]. The first eigenvalue λ_1 has a value of 1, corresponding to the steady-state distribution of the SF occupation states. Since the system exhibited non-equilibrium dynamics, λ_m and $\boldsymbol{\nu}_m$ could be complex-valued for $m > 1$. We took the norm of λ_m when computing the m-th relaxation time t_m, given by

$$t_m = -\frac{\tau}{\ln|\lambda_m|}. \tag{16}$$

t_m as a function of τ is plotted in Figure S2.

Another test checking whether Markov properties hold is the Chapman-Kolmogorov test [100, 75, 78], justifying to what extent the approximation,

$$\hat{\boldsymbol{T}}^k(\tau) \approx \hat{\boldsymbol{T}}(k\tau), \tag{17}$$

for $k = 2, 3, \ldots$, is fulfilled. τ was chosen to be 20 ps. Details can be found in the Supporting Information.

Independent permeation events, each capturing a series of transitions between SF occupation states that results in a K^+ arriving at the extracellular side while the SF returns to its original occupation state, were first extracted from the trajectories using Algorithm 1. It assumes that a positive membrane voltage is applied. WKK0KW was selected to be the initial and the final state (denoted as S_c) of the cycles as it was one of the states with a high probability of being observed under different simulation conditions. For instance, 98%

and 100% of the observed permeation events in Figure 8 can be expressed in cycles that start and end in WKK0KW for Amber14sb and CHARMM36m, respectively. Using Algorithm 2, each of these permeation cycles was reduced such that only the non-repeating, first-arrived states remain. Trivial oscillations between SF occupation states that involve no net ion jumps were removed. From the reduced permeation cycle trajectories, transition matrices, containing the probabilities of observing a transition between any two SF occupation states in a reduced permeation cycle, were computed. Apart from transition probabilities based on the reduced permeation cycles, the net fluxes $f_{ij} = T_{ij}\rho_i - T_{ji}\rho_j$, where ρ_i and ρ_j are the steady-state distribution of state S_i and S_j, respectively, between S_i and S_j were computed from the full trajectories without cycle identification and reduction. The currents through the channels were calculated as $I = \lfloor \frac{J_k}{5} \rfloor$, where J_k is the total number of net ion jumps in the SF throughout a simulation (see Figure S1 for details of ion jumps in the SF).

The mean first passage time (MFPT), for the transitions from state S_i to state S_j,

$$t_{\mathrm{MFPT}} = \mathbb{E}\Big[\inf\{t = t'' - t' \geq 1 : s(t') = S_i, s(t'') = S_j, 0 \leq \sum_{t^*=t'}^{t''-1} j_k(t^*) \leq 4\}\Big], \tag{18}$$

where $s(t)$ is the SF occupation state and $j_k(t)$ is the number of ion jumps at time t (see Figure S1), was computed. The last condition restricts the calculations to transitions within the same permeation cycle.

The permeation cycle analysis was performed using KPerm, a Python package developed by us. Libraries including MDAnalysis [101, 102], NumPy [103], and SciPy [104] were used to process and analyze simulation trajectories. NetworkX [105] was used to generate graphs of permeation cycles. Errors of MFPTs are bias-corrected and accelerated (BCa) 95% bootstrap intervals ($B = 10000$). Unless otherwise specified, errors are 95% confidence intervals based on the t-distribution.

4.3. Results

4.3.1. Selectivity Filter Occupancy

To probe the occupancy of SF during ion permeation, we carried out MD simulations of the pore of MthK WT, KcsA E71A, NaK2K F92A, and TRAAK WT in a 1 M KCl solution at 323 K and 300 mV. Mutants of KcsA [106] and NaK2K [107] were chosen to

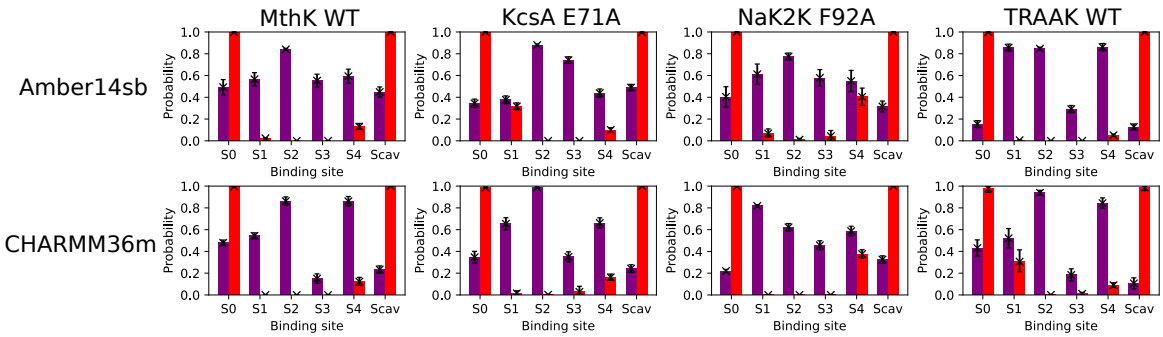

Figure 7: K^+ (purple) and water (red) occupancy in SF binding sites of channels simulated at 323 K and 300 mV in 1 M KCl solution.

obtain more permeation events as they have been shown to have higher conductance than WT. Since hundreds of K^+ permeation events in total for each system were recorded from independent simulations (Table S1, S2, S3, and S4), the average occupancy is not merely a consequence of the initially full K^+ occupancy of the SF but the preference of permeant ions and water molecules for SF binding sites during ion permeation.

S0 and Scav are exposed to water and thus have a nearly full water occupancy throughout the simulations of all channels (Figure 7). The inner binding sites S2 and S3 are mostly shielded from water. In MthK, S2 and S3 are completely dehydrated in simulations using Amber14sb and CHARMM36m. Non-zero water occupancy in S2 and S3, caused by rare events of water entering S2 or S3 from the cytosolic side in a few trajectories, is found in other channels. Water molecules hopping between S0 and S1 and between S4 and Scav happens, contributing to the water occupancy in S1 and S4, respectively. The high K^+ density in S1 to S4 and the dehydration of S2 and S3 suggest that the K^+ permeation happens predominately without water co-permeation. However, how water molecules contribute to the water-free K^+ permeation and under what conditions water co-permeation is triggered are not fully understood.

There are variations in K^+ and water occupancy between the channels with a highly conserved SF. The average occupancy of K^+ and water is also sensitive to the choice of force fields. For instance, the K^+ occupancy of S3 in CHARMM36m simulations tends to be substantially lower than that in Amber14sb simulations. S1 water occupancy of ∼30% is found in simulations of KcsA E71A using Amber14sb and simulations of TRAAK WT using CHARMM36m, but not in simulations using their counterpart force fields. The presence of water in the SF binding sites and variations in SF occupancy due to force fields and structural differences between channels prompt the questions about permeation

mechanisms in these systems and call for a dissection of the permeation processes in the SF.

4.3.2. Permeation Cycles

In search of the dynamical details of permeation processes in the SF of K^+ channels, we turned to Markov state modeling and expressed ion permeation events during the MD simulations as transitions between SF occupation states. The resulting Markov state models (MSMs) contain the arrays of six-character code that represent the occupancy of the six binding sites. Reduced permeation cycles were obtained by isolating permeation events from the trajectories and removing trivial oscillations between the states that do not result in net ion movement. An example of reduced permeation cycles can be found in Figure 6C. A closed loop in a permeation cycle depicts the sequence of SF occupation states for a permeation event in which the SF occupancy is restored to its initial configuration, thus completing a permeation event. With that, one K^+ has reached the extracellular side of the membrane through the SF.

The currents in MthK WT, with the simulated conditions, are 15.4 ± 2.2 pA and 6.8 ± 2.0 pA for Amber14sb and CHARMM36m, respectively. Errors represent 95% confidence intervals using the t-distribution. The reduced permeation cycles for MthK WT are displayed in Figure 8. The state WKK0KW was chosen to be the initial and final state of the cycles as it is one of the states with the highest probability under different simulation settings, including channels, force fields, K^+ concentration, temperature, and membrane voltage. For instance, 98% and 100% of the permeation events can be expressed as cycles starting and ending in WKK0KW for MthK WT using Amber14sb and CHARMM36m, respectively, at 300 mV and 323 K in a 1 M KCl solution. The permeation cycles are consistent with the plots using net fluxes as the weights of the edges (Figure S9).

Starting in WKK0KW, as the permeation proceeds, the first transition is predominantly to C0K0KW for both force fields. The transition represents the K^+ in S1 moving to S0 and sharing the same binding site with water. It was found in $48 \pm 3\%$ and $73 \pm 4\%$ of the reduced permeation cycles for Amber14sb and CHARMM36m, respectively (note that these probabilities are different from the transition probabilities in the MSMs). Three routes, ultimately converging to C0KKWC, branch out of C0K0KW. Two steps in common are involved: a K^+ and a water molecule in S4 and Scav hopping collectively to S3 and

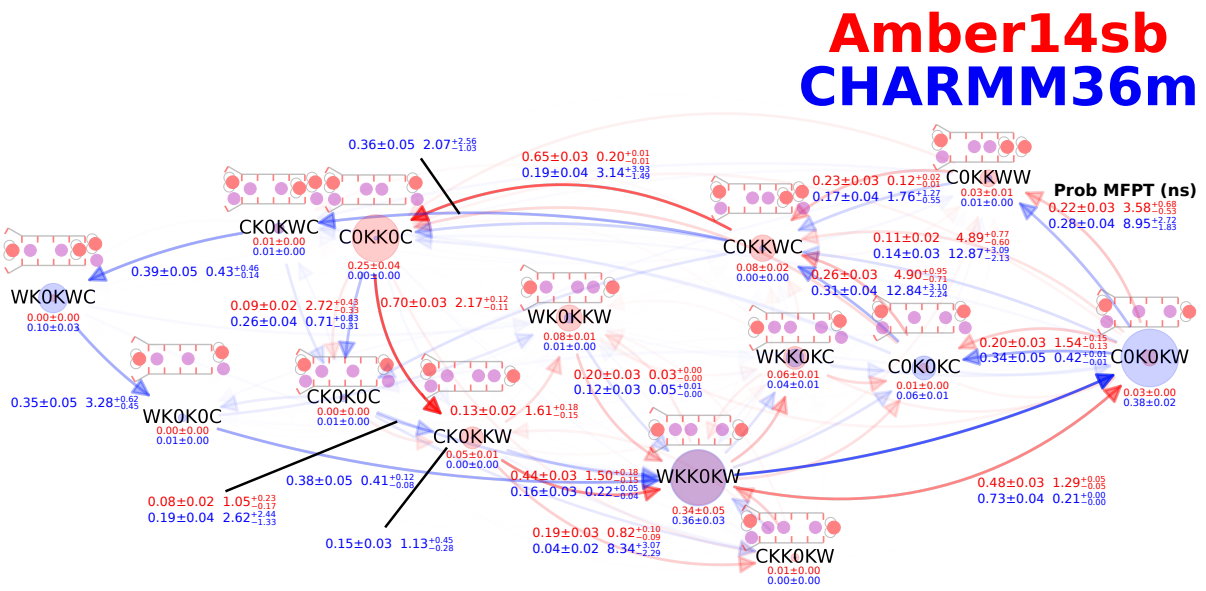

Figure 8: Permeation cycles and MFPTs of SF occupation state transitions for MthK WT at 300 mV and 323 K in 1 M KCl solution. Only states involved in more than 10% of the observed permeation cycles are shown. The steady-state distributions of the SF occupation states are stated below the nodes. The probabilities of observing the transitions given a reduced permeation cycle and the associated MFPTs are stated next to the edges. Cycles of 98% and 100% of the permeation events for Amber14sb and CHARMM36m, respectively, were identified and are shown.

S4 at the same time, respectively, and a K^+ approaching from the channel cavity to Scav. One of the three routes is the direct transition C0K0KW → C0KKWC, in which the two steps happen simultaneously for a lag time of 20 ps. The other two routes, which occur approximately twice as frequently as the direct transition, differ in the order of the two steps. C0K0KW → C0K0KC → C0KKWC represents the formation of a central ion pair in S2 and S3 with the presence of a K^+ in Scav. The last route C0K0KW → C0KKWW → C0KKWC suggests the possibility of spontaneous formation of a central ion pair without head-on collisions by a third K^+ in Scav.

Critical differences in permeation cycles between Amber14sb and CHARMM36m emerge at C0KKWC. For Amber14sb, the cycles continue with the depletion of a transient water molecule in S4 (C0KKWC → C0KK0C, $65 \pm 3\%$), followed by a concerted forward movement of two ions, moving from S2 to S1 and Scav to S4 (C0KK0C → CK0KKW, $70 \pm 3\%$), respectively. The dominant cycle is eventually closed by the dissociation of K^+ in S0 and the forward movement of K^+ from S3 to S2. The majority of the permeation events for Amber14sb can be represented by a single loop that splits at CK0KKW and

converges at C0KKWC. In contrast, a divergence into two distinct permeation routes at C0KKWC was observed for CHARMM36m. One of the two routes is similar to the Amber14sb permeation route, involving water depletion in S4, except that CK0K0C plays a more significant role in connecting C0KK0C and WKK0KW. Compared to the first permeation route, the depletion of transient water in S4 happens later in the second route. Ion movement facilitated by ion-ion repulsion (C0KKWC → CK0KWC → WK0KWC) finishes earlier than water depletion (WK0KWC → WK0K0C). The cycle ends with the K^+ coming from Scav to S4 and the K^+ in S3 moving to S2 (WK0K0C → WKK0KW). Mean first passage times (MFPTs) of the transitions were computed. The permeation cycles are comprised of transitions on a broad range of timescales between tens of picoseconds and tens of nanoseconds. For both force fields, the rate-limiting step is the formation of a central ion pair in S2 and S3 with vacant S1 (C0KKxx), likely due to the barrier posed by the strong Coulomb repulsion between the two K^+s. Consistent with the lower current in CHARMM36m simulations, most rate-limiting permeation steps are considerably slower in CHARMM36m simulations than in Amber14sb simulations. All the slowest steps in the three transition routes from C0K0KW to C0KKWC for CHARMM36m are about 2.5 times as slow as for Amber14sb. No permeation cycle finishes substantially faster than the others, suggesting that there is unlikely a permeation "short-cut" at a significantly higher rate that the channel may exploit to regulate ion conduction rate by switching between different permeation routes.

The permeation cycles in MthK represent the direct knock-on permeation, characterized by the close K^+ contact and the absence of water in S2 and S3. Despite the presence of water in S1 and S4, no water permeation event was observed. The water occupancy in S1 does not contribute to K^+ permeation, as no relevant SF occupation state is found in the permeation cycles. The transient S4 water occupancy shown in Figure 7 can be explained by the high probability of finding states with a water molecule in S4, including C0KKWC and WK0KWC, in a reduced permeation cycle. C0KKWC is achieved by a water molecule entering the SF during the formation of a central ion pair. The escorting water molecule enters the channel simultaneously with a K^+ jumping from S4 to S3. It appears to facilitate the formation of a central ion pair essential for the subsequent ion permeation steps. After forming the central ion pair, the water molecule escapes from S4 to Scav in spite of the presence of K^+ in the adjacent binding sites S3 and Scav. This

lingering water molecule may be due to the high cost of complete dehydration of K^+ when traversing through the SF.

The permeation patterns are sensitive to the choice of force fields. With the identified permeation cycles, we can explain the lower K^+ occupancy, compared to Amber14sb, in S3 for CHARMM36m. There is a higher probability of finding states such as C0KK0C, C0KKWC, CK0KKW, or WK0KKW, which has a K^+ in S3, in Amber14sb simulations then in CHARMM36m simulations. The permeation routes sampled by the two force fields manifest the direct knock-on mechanism, yet variations in the details of the permeation cycles exist.

4.3.3. Diversity of Permeation Cycles

We examined the permeation cycles individually. As shown in Figure 9, the most frequently observed permeation cycles account for only 4.0% and 4.9% of the total observed cycles in Amber14sb and CHARMM36m simulations, respectively. Upon closer examination of the permeation cycles, the apparently highly diversified permeation cycles exhibit many common features. For instance, the cycles converge to the same route as the permeation proceeds. The observed cycles share multiple intermediate SF states that emerge in the same order in time to connect the cycles. While there are numerous non-identical permeation cycles, the ion permeation is not about random occupancy of the SF but collective motions of K^+ and water with patterns. The observed permeation cycles carry a lot of common features that one can extract to analyze the underlying conduction mechanisms in the simulations.

4.3.4. Effects of Potassium Concentration

The permeation cycle analysis allows a systematic investigation into the effects of physical factors, such as K^+ concentration, temperature, and membrane voltage, on the permeation mechanisms in K^+ channels. While it is expected that increasing K^+ concentration leads to increased ionic current, microscopic details of the impacts of K^+ concentration on ion conduction remain elusive. We, therefore, carried out simulations of MthK WT in a KCl solution of concentrations ranging from 0.1 M to 2.0 M and analyzed the permeation cycles (Figure 10).

The channel remains conductive in all simulations. No significant conformational change

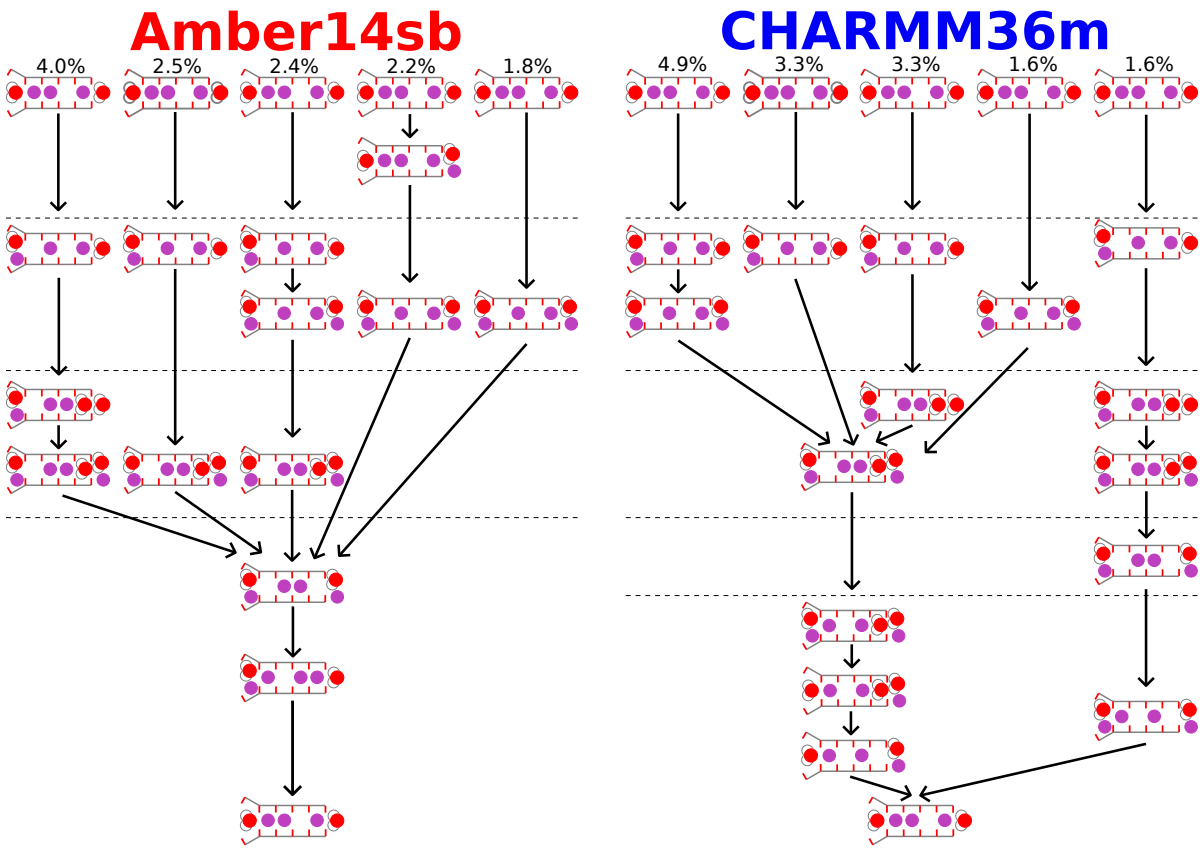

Figure 9: Diversity of permeation cycles. The first five most frequently observed permeation cycles are shown.

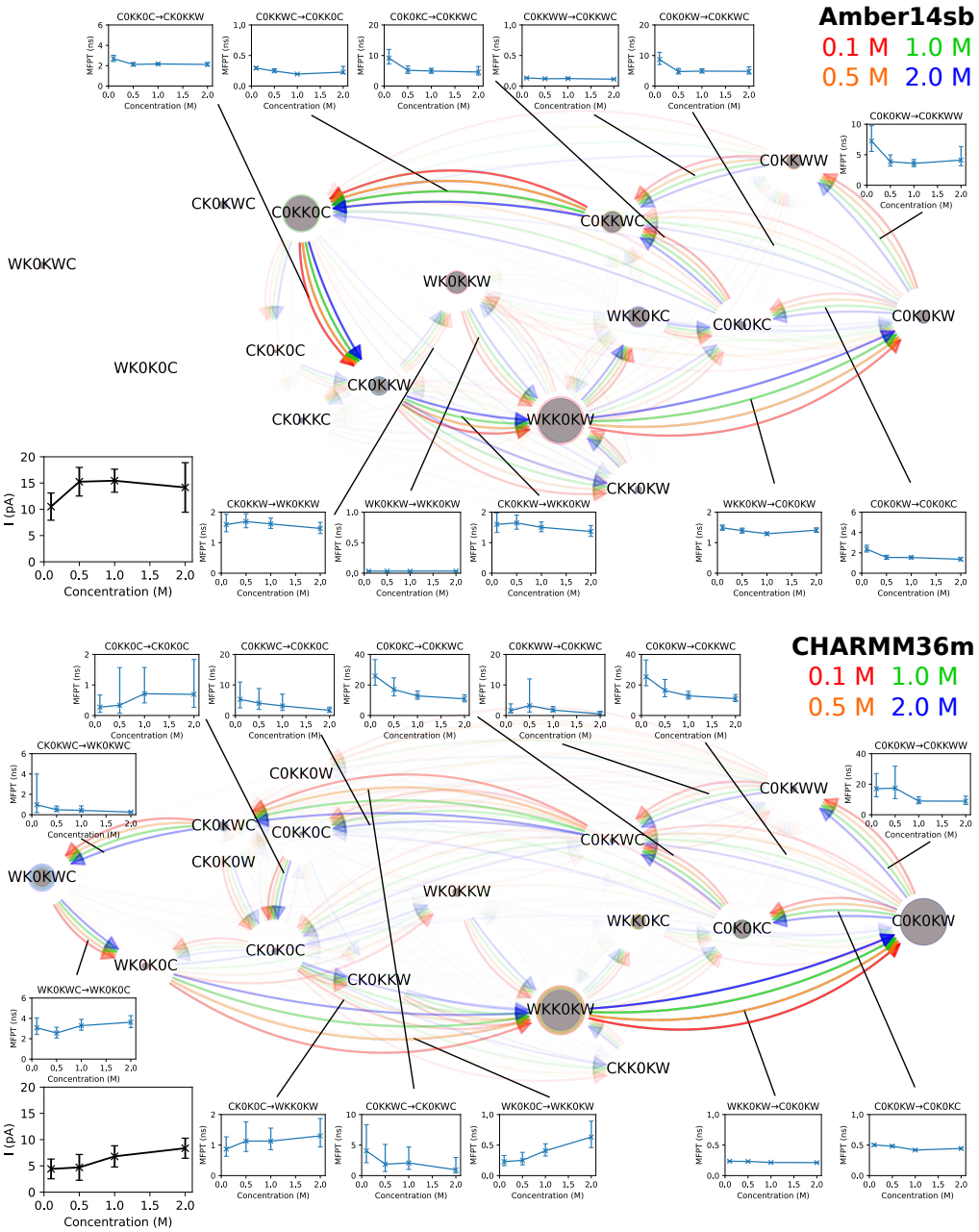

Figure 10: Permeation cycles, MFPTs of SF occupation state transitions, and currents for MthK at 300 mV and 323 K in KCl of different concentrations. See the description in Figure 8 for the meaning of nodes and edges. Insets are the currents and the MFPTs of the transitions as a function of KCl concentration. Cycles of 98%, 97%, 98%, and 97% for Amber14sb and 99%, 100%, 100%, and 96% for CHARMM36m of the permeation events in a 0.1, 0.5, 1.0, 2.0 M KCl solution, respectively, were identified and are shown.

of the SF was observed, even for simulations which show low K^+ permeation counts, suggesting that the pore domain of MthK is stable over a wide range of KCl concentrations for at least 500 ns. Surprisingly, even with a 20-fold increase in KCl concentration, many details of the permeation, including the preferred transition paths and the steady-state probabilities of SF occupation states, remain largely unaffected. The acceleration in ion permeation is mainly attributed to the shorter MFPTs of the rate-limiting steps, approximately reduced by half when increasing the K^+ concentration from 0.1 M to 2.0 M. Although the two force fields sample different permeation routes, similar effects of salt concentration on ion permeation were observed in Amber14sb and CHARMM36m simulations.

Interestingly, one water permeation event happens in one of the CHARMM36m simulations with a K^+ concentration of 2.0 M. A water molecule stalls the channel for ∼250 ns until it has crossed the SF. Afterward, the channel resumes the water-free direct knock-on permeation and remains conductive to K^+ for the rest of the simulation. Therefore, water permeation is possible yet extremely rare under the given simulation conditions.

4.3.5. Effects of Temperature

The temperature dependence of permeation cycles in MthK was also probed. As shown in Figure 11, similar to the K^+ concentration dependence, the permeation patterns exhibited by the channel are largely invariant even when elevating the temperature drastically from 283 K to 333 K (well above 270 K, the phase transition temperature of pure POPC bilayers [108]). While increasing the K^+ concentration primarily speeds up the rate-limiting steps of ion conduction, the higher temperature accelerates most SF occupation state transitions relevant to permeation. Although the ion conduction rate increases substantially at higher temperatures, no water co-permeation was observed. We conclude that the permeation mechanism of the pore domain of MthK is insensitive to temperatures between 283 K and 333 K.

The free energy differences between SF occupation states of KcsA were found to be insensitive to the temperature for CHARMM36m [109]. Given the structural similarities between the SF of KcsA and MthK, we believe that the conductance of MthK increases with temperature primarily due to more frequent attempts of ions overcoming the barriers during all permeation steps.

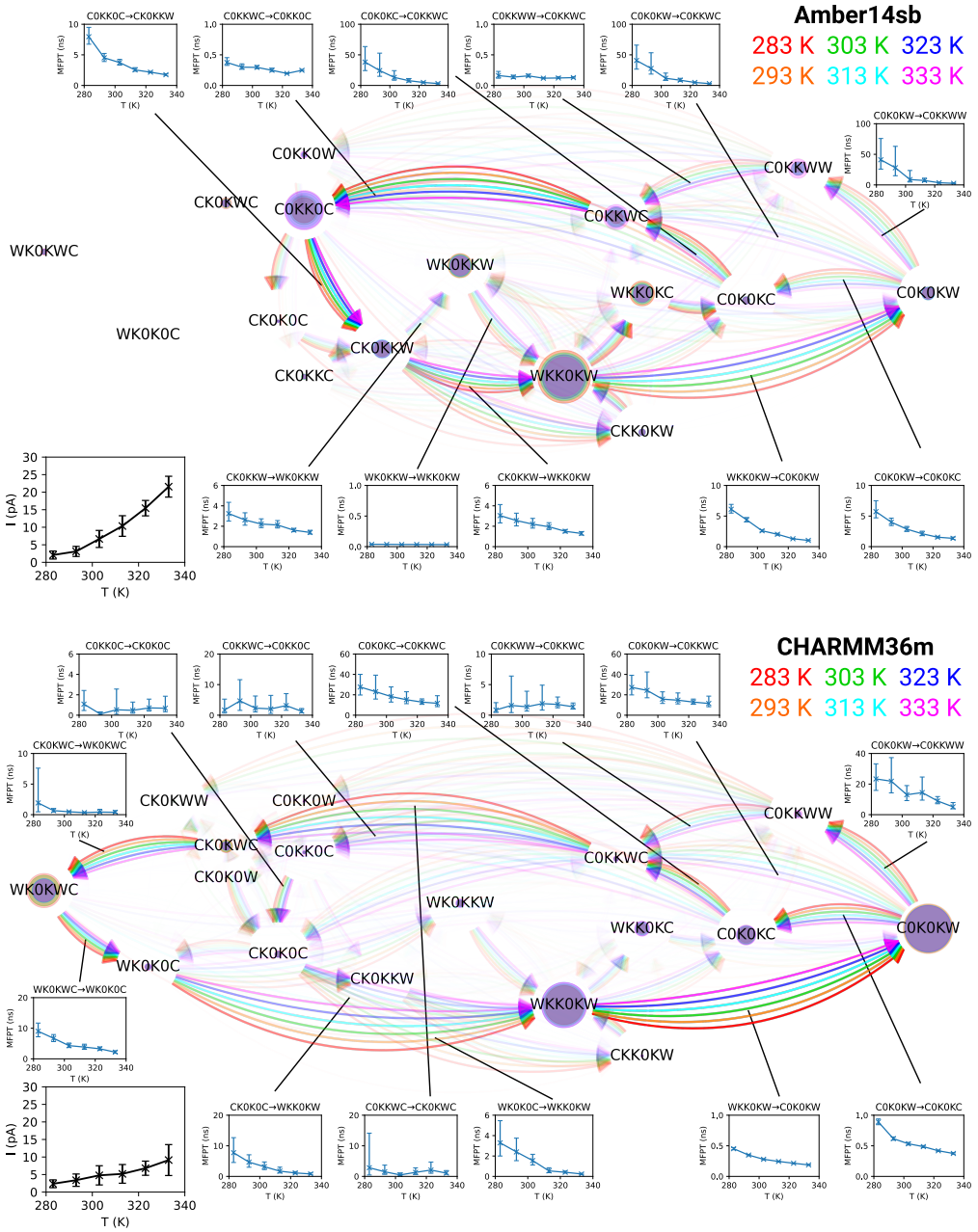

Figure 11: Permeation cycles, MFPTs of SF occupation state transitions, and currents for MthK at 300 mV and different temperatures in 1 M KCl. See the description in Figure 8 for the meaning of nodes and edges. Insets are the currents and the MFPTs of the transitions as a function of temperature. Cycles of 97%, 98%, 97%, 98%, 98%, and 98% for Amber14sb and 100%, 100%, 100%, 100%, 100%, and 100% for CHARMM36m of the permeation events at 283, 293, 303, 313, 323, and 333 K, respectively, were identified and are shown.

4.3.6. Effects of Membrane Voltage

Membrane voltage influences the rates of most of the permeation steps (Figure 12). As the membrane voltage increases, transition pathways and SF occupation states are redistributed, more significant than what was identified when varying K^+ concentration or temperature. While the permeation patterns are moderately conserved at a membrane voltage below 300 mV, there is a shift in permeation pathways toward the alternative route C0KKWC → CK0KWC → WK0KWC for both force fields at high voltages (450 mV and 600 mV). In CHARMM36m simulations, a high voltage promotes this route which is present under most of the conditions we explored. In Amber14sb simulations, this alternative route emerges only at high voltages. The route is connected with states WWKKWC and WWKK0C, which have high water content and are irrelevant to permeation under most of the explored conditions. The permeation at high voltages is more chaotic, as only 96% and 90% for Amber14sb and 95% and 87% for CHARMM36m of the permeation events can be described in closed cycles that start and end in WKK0KW at 450 mV or 600 mV, respectively. A few water co-permeation events were identified at high voltages. The tendency of water traversing the SF is mechanistically similar to the so-called water finger protrusion that happens before pore formation induced by a strong electric field in lipid bilayers [110]. Since the voltage drop happens mainly in the SF, the electric field $E_z = -\frac{\partial V}{\partial z}$ along the channel axis inside the SF increases with the applied membrane voltage. The force exerted on a dipole increases with the increase in electric field strength inside the SF. The strengthened coupling of dipoles to the electric field drives water into the SF [111]. The current not increasing with the voltage at a high limit is likely due to the chaotic permeation triggered by the propensity of water co-permeation at an exceedingly high voltage, which slows down the ion permeation.

4.3.7. Permeation Cycles in Different Channels

Next, we explored how the permeation mechanisms differ for different channels with a SF with an identical or slightly different amino acid sequence. The observed currents for MthK WT, KcsA E71A, NaK2K F92A, and TRAAK WT are different (Figure 13). Noticeable differences in the steady-state distribution and preferred transitions between SF occupation states during ion permeation were also found. Starting from WKK0KW, C0K0KW is usually visited before C0KKWW for MthK WT. In contrast, KcsA E71A,

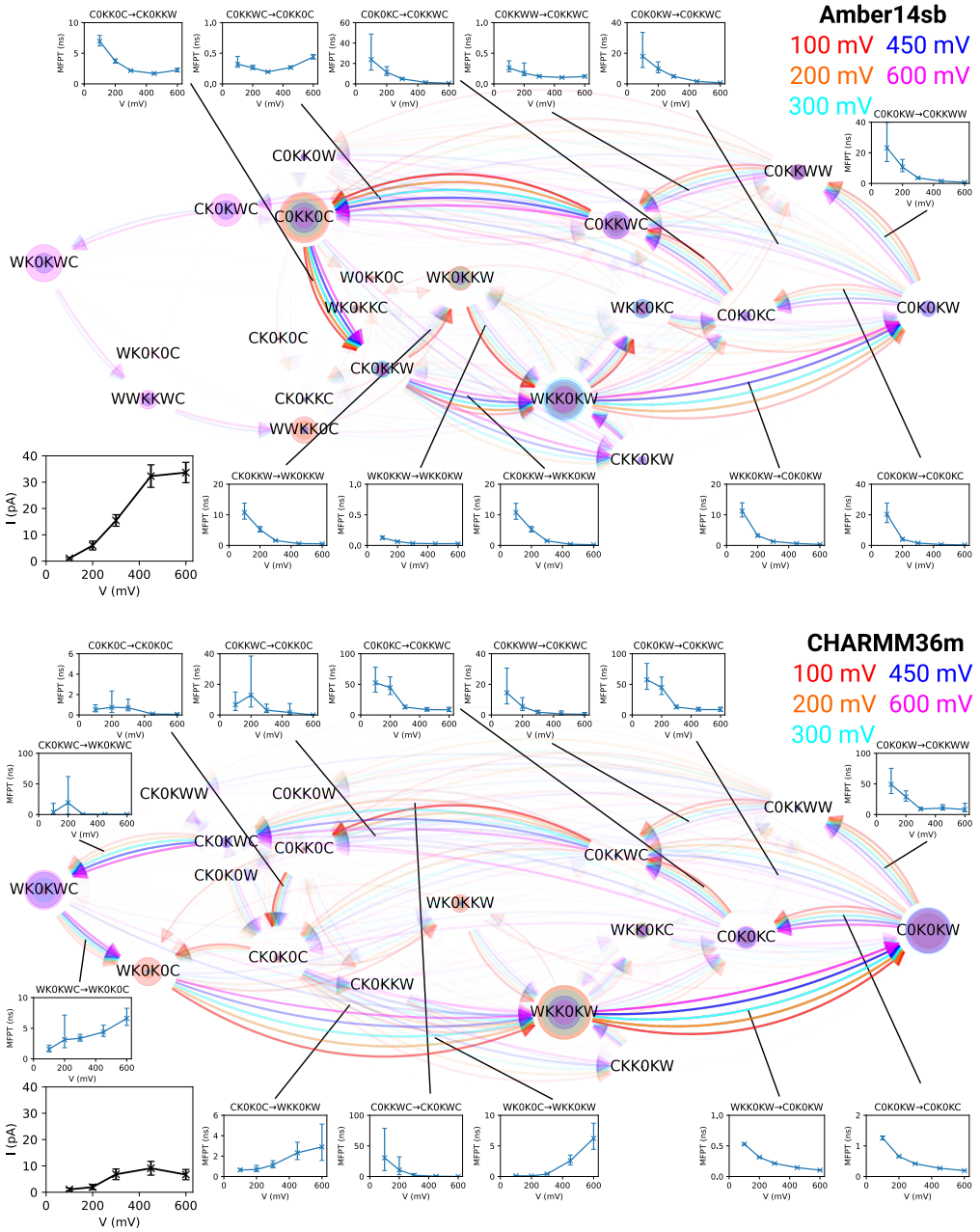

Figure 12: Permeation cycles, MFPTs of SF occupation state transitions, and currents for MthK at different membrane voltage and 323 K in 1 M KCl. See the description in Figure 8 for the meaning of nodes and edges. Insets are the currents and the MFPTs of the transitions as a function of voltage. Cycles of 88%, 98%, 98%, 96%, and 90% for Amber14sb and 100%, 100%, 100%, 95%, and 87% for CHARMM36m of the permeation events at 100, 200, 300, 450, and 600 mV, respectively, were identified and are shown.

NaK2K F92A, and TRAAK WT can skip C0K0KW, transitioning from WKK0KW to C0KKWW directly in one step for a lag time of 20 ps. Another deviation from MthK WT is that all other channels prefer C0K0KW → C0KKWW → C0KKWC to C0K0KW → C0K0KC → C0KKWC, but these two paths are equally populated in MthK WT. The path C0KKWC → CK0KWC → WK0KWC → WK0K0C → WKK0KW present in CHARMM36m simulations is prevalent in MthK WT and NaK2K F92A, but it is almost absent in KcsA E71A and TRAAK WT. In Amber14sb simulations, KcsA E71A uses an alternative path C0KK0C → CWKK0C → WWKK0C → WWKKKW → WKK0KW for K^+ permeation.

Along with hundreds of K^+ permeation events, a few water permeation events were identified in simulations of KcsA E71A and TRAAK WT using CHARMM36m. This observation reveals again that water permeation is a possible yet rare event. Different channels may have different voltage tolerance as water co-permeation is a signature of channels subjected to an exceedingly high membrane voltage. Most observed permeation events involve no water permeation, implying the dominance of the water-free direct knock-on mechanism in K^+ channels. The formation of the central ion pair remains the slowest permeation step for all channels, except for KcsA E71A simulated with CHARMM36m, as several slowest permeation steps have similar MFPTs. We conclude that there are channel-specific variations in permeation cycles among the channels, but the direct knock-on permeation mechanism and most permeation patterns remain highly conserved.

4.3.8. Charge Strength Dependence of Permeation Cycles

Modifying intermolecular interaction parameters of a force field to reproduce realistic behaviors of biological systems is a popular technique for force field optimization [112, 113]. One possible way is to scale the charges of charged molecular groups, such as charged residues and ions [114]. Since we have demonstrated that different permeation patterns arise from Amber14sb and CHARMM36m, scaling the charges is expected to alter the conductance and permeation patterns of the channels. To continue exploring the charge strength dependence of permeation cycles, we performed simulations of MthK WT with different charge scaling factors q/q_0 for charged residues and ions. The external electric field strength was kept at 0.035 V nm^{-1}, equivalent to 300 mV for the unmodified system. The calculated currents were based on the number of ion jumps j_k through the SF and not

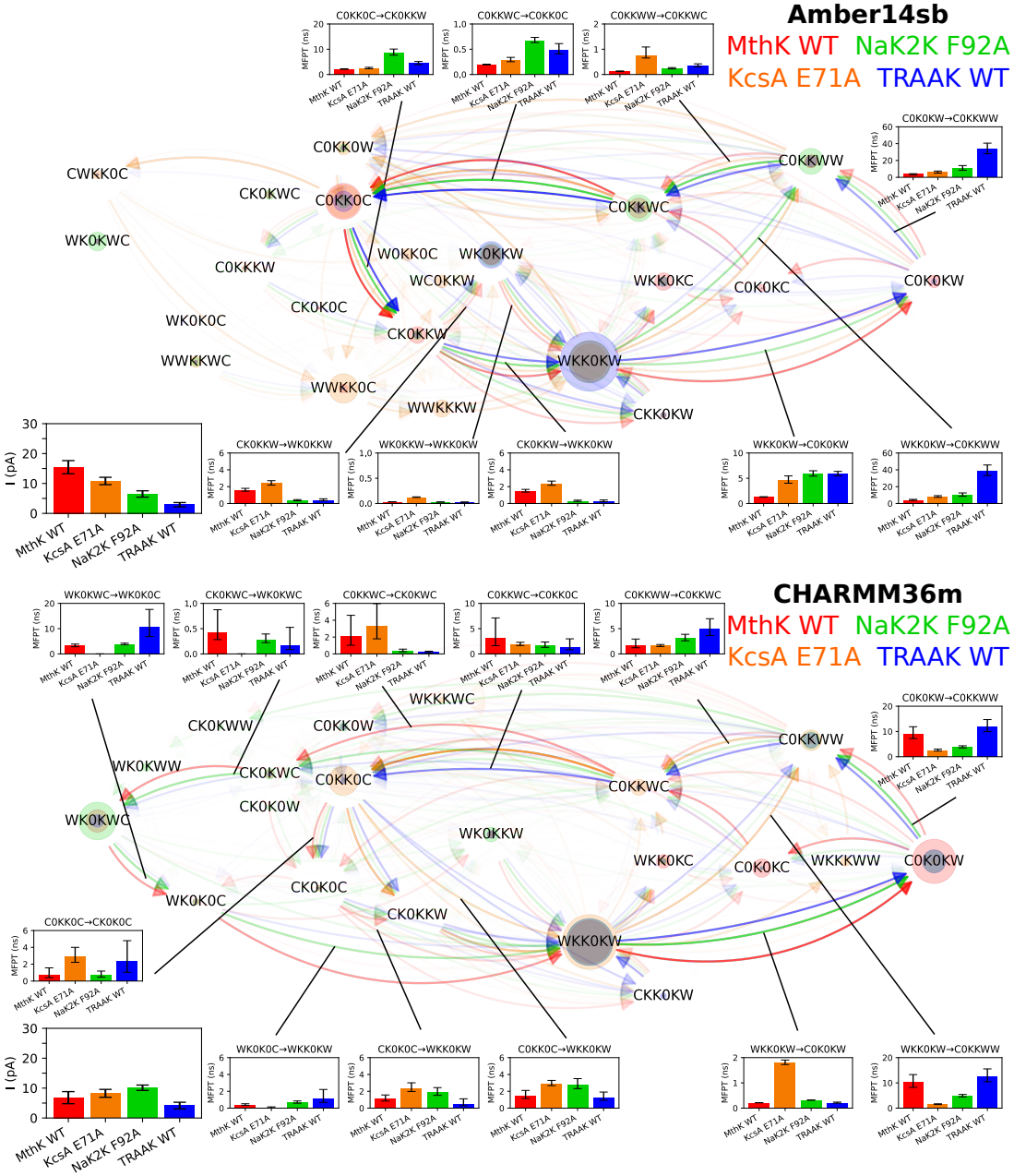

Figure 13: Permeation cycles, MFPTs of SF occupation state transitions, and currents for MthK WT, KcsA E71A, NaK2K F92A, and TRAAK at 300 mV and 323 K in 1 M KCl solution. See the description in Figure 8 for the meaning of nodes and edges. Insets are the currents and the MFPTs of the transitions. Cycles of 95%, 93%, 91%, and 86% for Amber14sb and 94%, 89%, 95%, and 83% for CHARMM36m of the permeation events in MthK WT, KcsA E71A, NaK2K F92A, and TRAAK, respectively, were identified and are shown.

corrected for the scaled charges. Using Amber14sb, the conductance of MthK fluctuates when q/q_0 decreases from 1.00 to 0.70. For CHARMM36m, the conductance drops from 6.81 ± 2.01 pA to 0.32 ± 0.24 pA when q/q_0 decreases from 1.00 to 0.90 and rises drastically to 138.9 ± 18.1 pA when q/q_0 decreases to 0.70 (Figure 14). There are substantial shifts in the permeation patterns as the charges are reduced, causing the state WKK0KW to no longer be visited as frequently, especially when the factor is small (≤ 0.75). As a result, not most of the permeation events can be represented as cycles that start and end in WKK0KW. Instead, the net fluxes in different systems are compared. For both force fields, routes involving a high number of ions inside the SF dominate the permeation cycles when the charges are scaled down, consistent with the intuition that the reduced charges lead to weakened electrostatic repulsion between ions and favor more ions occupying the binding sites simultaneously.

4.4. Discussion

4.4.1. Conduction Properties under Different Conditions

Unlike KcsA, which has the same signature sequence TVGYG as MthK for the SF, X-ray crystallography revealed that the SF of MthK remained structurally unchanged at a low (1 mM) or even zero K^+ concentration, suggesting that the SF maintains a conductive conformation at an extremely low concentration of K^+ [85, 115]. MD simulations showed that the SF of MthK collapsed in 0 mM K^+, yet the introduction of one K^+ in either S1, S2, or S3 prevented SF from collapsing and helped maintain a conductive conformation [115]. Due to the small size of the simulation box used in our study, we could not decrease the KCl concentration further to probe the ion permeation and the conformational changes of MthK WT at a K^+ concentration lower than 0.1 M while keeping a reasonable number of mobile ions for neutralizing the system and maintaining ionic fluxes through the channel. Our MD simulations demonstrate that the pore of MthK allows continuous K^+ permeation in a KCl solution at a concentration as low as 0.1 M and as high as 2.0 M.

Single-channel recordings of MthK revealed a high temperature sensitivity between 294 K and 312 K. N-terminal deletion constructs of MthK in the presence of 0.1 mM calcium showed a 20-fold increase in open probability (P_o) by increasing the temperature [116]. The temperature dependence was found to originate from the coupling between the pore domain and the RCK domain. As the temperature increased, the coupling appeared to

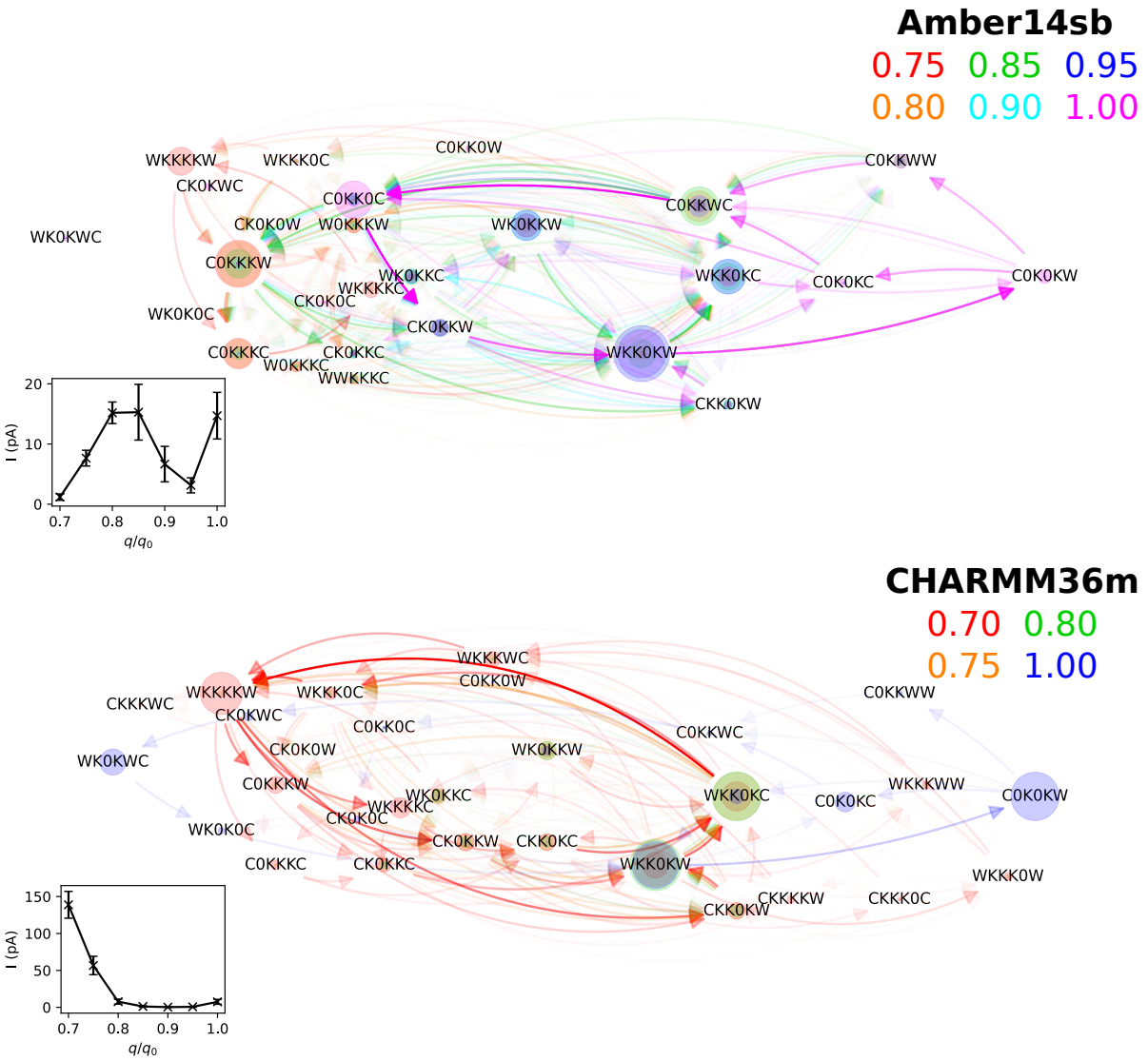

Figure 14: Net fluxes between SF occupation states for MthK at 0.035 V nm^{-1} and 323 K in 1 M KCl with different charge scaling factor q/q_0. Node sizes scale with the steady-state distributions of the SF occupation states. Edges represent the net fluxes between states. Only the net fluxes larger than 0.15 and 0.03 of the maximum among all net fluxes are shown for Amber14sb and CHARMM36m, respectively.

be disrupted. The same temperature dependence was not observed from the pore-only structure of MthK, a truncated construct in which the N-terminal segment and the RCK domain were absent, similar to the structure we simulated. At −100 mV, increasing the temperature from 293 K to 309 K led to an approximately 4-fold decrease in P_o while the unitary conductance increased slightly. We observed no pore closure during the simulations. The discrepancy may be due to the difference between the microsecond timescale of our MD simulations and the millisecond timescale of open-closed transitions in the experiment, deduced from the mean open time and the mean closed time. In agreement with the experimental observation of increased single-channel conductance, the pore domain of MthK displays higher currents at +300 mV upon elevated temperature over the range between 283 K to 333 K in our MD simulations. Note that direct comparison of conductance computed by $G = I/V$ is not straightforward as MthK demonstrates voltage-dependent rectification at positive potentials [12].

Even though MthK lacks a canonical voltage-sensing domain [117], it possesses a voltage-dependent gate reminiscent of the C-type inactivation gate located at the selectivity filter [118]. At negative potentials, P_o remains high and increases slightly with voltage. Upon depolarization, a drastic reduction in P_o with voltage was observed. Again, no event of channel closing was observed from our simulations, likely because of the much shorter timescale sampled by the MD simulations. Furthermore, increasing external K^+ concentration increases P_o at positive potentials, stabilizing MthK in the open state [119]. Observing no significant conformational change of the selectivity filter at a high voltage that characterizes a transition from the open state to the closed state during our simulations could result from the stabilization by the high K^+ concentration. In qualitative agreement with the single-channel recording [120, 119], the simulated currents in MthK WT channels increase with the magnitude of the applied voltage between +100 mV and +200 mV.

4.4.2. Robustness of Direct Knock-on

Consensus on whether soft knock-on or direct knock-on is the dominant permeation mechanism used by most K^+ channels is, as of now, not fully reached [18]. Markov state modeling allows for an in-depth analysis of the conduction events and the associated mechanisms in K^+ channels [47, 121]. Here, for both Amber14sb and CHARMM36m,

most permeation events observed in our simulations of MthK WT over a wide range of physical conditions, including K^+ concentration, temperature, and membrane voltage, happen via direct knock-on. Direct knock-on is also the major permeation mechanism in KcsA E71A, NaK2K F92A, and TRAAK WT, all of which share a largely conserved SF with MthK WT. Permeation events can be represented by cycles of transitions between SF occupation states. The identified cycles are apparently diversified yet have many features in common. For Amber14sb, most permeation cycles can be collapsed into a single loop. Two loops, one overlapping with the loop of Amber14sb, explain most of the observed cycles in CHARMM36m simulations. Under most conditions, the rate-limiting step involves the formation of a central ion pair in S2 and S3. Water is found occasionally in S1 and S4. Our analysis suggests that, except for KcsA E71A using Amber14sb, S1 water occupancy is irrelevant to ion permeation when a positive membrane voltage is applied. Transient occupancy of a water molecule in S4 is involved in the permeation, but no water molecule passes through the SF in most cases.

Rectangular voltage pulses of 450 mV induce electroporation of a synthetic POPC bilayer in 10 μs [122]. At extremely high voltages (450 mV or above), we observed deviations in permeation cycles from the typical ones, accompanied by a few water permeation events reminiscent of the water finger protrusion that happens before the pore formation in lipid bilayers [110]. Simulations of KcsA E71A and TRAAK WT using CHARMM36m also reveal rare water co-permeation events. There were reports of water-mediated permeation events, where ions and water molecules permeated through the channel under an applied membrane voltage. However, the effective membrane voltages in their studies were much higher than the physiologically relevant voltages [123, 124, 125, 126], confirming the propensity of water permeation at high voltages. At lower voltages, direct knock-on was observed in independent studies using MD simulations [17, 82, 10, 127, 121].

Experimental evidence appears to be in favor of direct knock-on over soft knock-on in general [18]. For instance, single wavelength anomalous dispersion X-ray diffraction data revealed full occupancy of S1 to S4 by K^+ in NaK2K [22] and TREK-1 [21], making the traditional interpretation of the electron density map as a superposition of KWKW and WKWK for S1 to S4 less appealing. Solid-state nuclear magnetic resonance measurements support the idea of water-free binding sites, at least for S3 and S4, in NaK2K [19]. Electrophysiological measurements with Rb^+ and Cs^+ suggest that 3 to 4 ions are required

to enter the SF to activate the filter for the voltage-dependent gating in K2P channels which lack a canonical voltage-sensing domain [20]. That said, fitting MD snapshots to two-dimensional infrared spectroscopy data probing the occupancy of S1 to S3 in KcsA revealed that both states representing soft knock-on and states representing direct knock-on derived from MD could explain the data equally well [17]. Despite the poor signal-to-noise ratio, different experimental conditions, and difficulties in interpreting streaming potential measurements, the data arguably support the co-permeation of water through K^+ channels and are compatible with the soft knock-on mechanism [23, 24, 25]. More efforts are required to distinguish under what conditions one permeation mechanism overtakes the other. We believe that direct knock-on is an overall better hypothesis explaining and reconciling various independent experimental and computational findings than soft knock-on regarding ion permeation in K^+ channels under physiological conditions.

Variations in conductance and permeation cycles were observed from MthK WT, KcsA E71A, NaK2K F92A, and TRAAK WT. It implies that the amino acid sequence of the SF is not the only determining factor for K^+ permeation across the SF. Since ion permeation is sensitive to the precise geometry of the SF [80], residues in the vicinity of the SF likely contribute to the conformational dynamics of the SF and influence the movement of ions through the SF. In KcsA, E71A is a substitution of the glutamic acid behind the SF. The mutation prevents the inactivation of KcsA, possibly by disrupting the carboxyl-carboxylate interactions between D80 and E71 [106]. Such a mutation may alter the conductance of the channel by influencing the geometry of the SF, and the impacts would be reflected in the permeation cycles. The analysis framework presented in this work allows for a systematic comparison of permeation cycles in different simulated systems to study the underlying permeation mechanisms quantitatively. With our framework, studies such as exploring the permeation mechanisms used by different mutants of K^+ channels in the future become possible.

4.4.3. Charge Strength Dependence of Permeation Cycles

It is crucial to emphasize that our findings were based on non-polarizable fixed-charge atomistic models. Polarizable force fields, such as AMOEBA [128], are not as popular as the fixed-charge force fields, such as Amber14sb and CHARMM36m, in part due to higher computational cost. However, improving the existing non-polarizable fixed-charge

force fields is desirable as the simulated conductance of K^+ channels is often underestimated [127]. The estimated currents from our simulations are approximately one order of magnitude lower than the experimental values [119, 120]. An alternative to introducing polarizability to fixed-charge force fields is to model the electronic polarization effects using a mean-field approximation via charge scaling, known as the electronic continuum correction (ECC) [114]. Our simulations reveal new permeation cycles with higher ion occupancy by scaling the charges of charged residues and ions to 0.7 of the original charges. For CHARMM36m, there is a 20-fold increase in the conductance of MthK WT. In line with our charge scaling simulations, it has been shown that using AMOEBA or CHARMM36m with ECC favors full ion occupation over water/ion alternate occupation in the SF, likely further promoting water-free ion permeation [109]. While the authors computed the free energy profile for the single-vacancy mechanism [129], the single-vacancy permeation pathway was not necessarily the dominant pathway used by the channel, as we have shown that the permeation pathways depend on the actual implementation of the force field. The quantitative framework for analyzing permeation cycles presented in our work can serve as a complementary tool for identifying permeation pathways adopted by ion channels, which can be then used to calculate the associated free energy profiles to obtain a comprehensive view of the ion permeation processes. We expect that the conduction rates and permeation patterns will differ when switching from a fixed-charge force field to a polarizable force field.

The precise details of the ion permeation mechanism are sensitive to the choice of force field. Amber14sb and CHARMM36m, being fixed-charge and non-polarizable force fields, result in different conduction rates and permeation patterns cycles. Despite overlapping pathways, our Markov state models reveal that the dominant, direct knock-on-based permeation pathways observed in Amber14sb and CHARMM36m simulations are not identical. It is highly advised, if possible, to use different force fields for comparison as far as ion permeation is concerned. The differences in permeation details between the two force fields suggest that determining optimal force field parameters is of paramount importance. Our framework for analyzing permeation cycles provides additional insights into the quantitative details of ion permeation events that help guide the calibration of force field parameters for properly characterizing the ion permeation processes in MD simulations. An optimization strategy for developing a non-polarizable force field dedicated

to reproducing desired conduction properties in K^+ channels is to match the conductance, permeation cycles, and the MFPTs of permeation steps for channels simulated using a polarizable force field. From our results, applying charge scaling to CHARMM36m can be a promising starting point for this purpose.

4.4.4. Conclusions

Using molecular dynamics simulations and Markov state modeling, we computed permeation cycles representing ion permeation events in the selectivity filter of potassium channels. The permeation cycles demonstrate the robustness of the direct knock-on permeation mechanism over a wide range of conditions, including potassium concentration, temperature, and voltage. These factors primarily influence ion conduction rates, while the impacts on selective filter occupancy and permeation pathways were relatively insignificant. Water co-permeation and deviations from the typical ion permeation cycles were almost only observed at supraphysiological voltages. Additional simulations suggest that direct knock-on remains the dominant permeation mechanism in different potassium channels with a highly conserved selective filter. Lastly, we show the charge strength dependence of permeation cycles via charge scaling and demonstrate the possibility of force field optimization using the framework presented in this work. Our results reveal the underlying details of permeation processes in the selectivity filter and help answer long-standing questions regarding permeation mechanisms in potassium channels.

4.4.5. Acknowledgment

We thank Maximilian Vossel for his exploratory work regarding permeation cycle analysis, Wojciech Kopec for the simulation setups and the insightful discussion, Chenggong Hui for the advice on charge scaling simulations, and Andrei Mironenko for the initial structures of KcsA.

5. Identification of Gating-Sensitive Residues in TREK-2

Abstract

TREK-2, a two-pore domain potassium (K2P) channel, responds to a wide range of stimuli, such as pH, membrane tension, and binding of small ligands. The crystallographic up and the down conformations have been resolved, where their main difference lies in the position and orientation of the transmembrane helix M4. However, molecular explanations for gating mechanisms and whether transitions between these two conformations play an essential role in gating remain elusive. Here, we use molecular dynamics (MD) simulations and free energy calculations to determine how the equilibrium between the up and the down conformations of TREK-2 is shifted by mutations. We identified mutants that exhibit a considerable shift away from the down state. Most conformational shifts due to mutations can be attributed to induced steric clashes or weakened favorable interactions in the cytoplasmic part of M2, M3, and M4. These findings are in excellent agreement with functional analysis and norfluoxetine (NFx) inhibition measurement of TREK-1 WT and mutants, shedding light on the molecular roles of the identified residues in governing transitions between the two conformations and suggesting a possibility of conformational switching between the up and down states as a gating mechanism for TREK-1 and TREK-2.

5.1. Introduction

The background and the gating hypothesis of K2P channels are summarized in Section 1.2. Here, we aim to investigate the possibility of switching between the up and down states as a gating mechanism for TREK-1 and TREK-2. To this end, we first identified residues that contribute to the conformational equilibrium between the two states of TREK-2 using molecular dynamics (MD) simulations and free energy calculations, providing molecular explanations for their roles in maintaining the stability of the two states. Experimental measurements, including conductance upon pH activation and norfluoxetine (NFx) inhibition, are performed for TREK-1 WT and mutants in parallel to assess the functional relevance of the residues. Our combined results will elucidate the gating sensitivity of residues in TREK-1 and TREK-2 and represent evidence for whether conformational switching between the up and down states is a valid gating mechanism for these channels.

5.2. Methods

5.2.1. System Construction

The up (PDB ID: 4BW5) and the down (PDB ID: 4XDJ) crystal structures of TREK-2 were used as the starting structures for the MD simulations [29]. Missing loops and residues were introduced using LOOPY [130] and PyMOL [131]. The resulting structures were truncated at K333. CHARMM-GUI [83, 56, 84] was used to embed TREK-2 into a 1-palmitoyl-2-oleoyl-sn-glycero-3-phosphocholine (POPC) membrane bilayer. The systems were solvated and neutralized by a 500 mM KCl solution. Two force fields, Amber14sb [55] and CHARMM36m [57] were used. For Amber14sb, Slipids [132], the TIP3P water model [90], and Joung and Cheatham ion parameters [91] were used. For CHARMM36m, CHARMM36 lipids [92], CHARMM36 TIP3P water model [93] and CHARMM36 ion parameters [94] were used. No membrane voltage was applied. An integration timestep of 2 fs was used for all simulations. All simulations were performed in GROMACS 2019 or GROMACS 2020 [98, 99].

5.2.2. Free Energy Calculations

Mutants that carried hybrid residues for the free energy calculations were generated with pmx [133]. 10,000 energy minimization steps were performed with a steepest descent

algorithm preceding the simulations. Harmonic position restraints with a force constant of 1,000 kJ mol^{-1} nm^{-2} were applied to all backbone atoms of the channel. All bonds were constrained with the LINCS algorithm [53]. For CHARMM36m simulations, Newton's equations of motion were integrated with a leap-frog stochastic dynamics integrator at 300 K. Pressure was coupled with the Parrinello–Rahman barostat [97] at 1 bar. Van der Waals forces were switched smoothly to zero between 1.0 to 1.2 nm. The particle mesh Ewald (PME) method [60] with a 1.2 nm distance cutoff was used for electrostatic interactions. For Amber14sb simulations, a leap-frog algorithm was used as the integrator. Temperature and pressure were kept at 300 K with the velocity rescaling algorithm [61] and 1 bar with the Parrinello–Rahman barostat. A cutoff of 1.5 nm was used for van der Waals interactions. The PME algorithm with a 1.5 nm distance cutoff was used for electrostatic interactions.

For every combination of systems, ten 20-ns equilibrium simulations were carried out. For the non-equilibrium simulations, starting snapshots were taken from the equilibrium runs every 80 ps (the first 1 ns was discarded). During the non-equilibrium simulations, as TREK-2 is a dimer, two residues were morphed into target ones alchemically in 100 ps. The work values associated with the non-equilibrium transitions were computed via thermodynamic integration (TI). Combining the work values computed from the forward and the backward transitions via the Crooks fluctuation theorem [134] and the Bennett Acceptance Ratio (BAR) method [71] yielded the free energy differences $\Delta G_{up}^{mutation}$ and $\Delta G_{down}^{mutation}$ (Figure 16A). Point estimates of the free energy differences were obtained by including all the computed forward and backward work values. Uncertainties were estimated as the standard error of the ten independent estimates of ΔGs, each coming from a unique pair of the distributions of forward and backward work values. For CHARMM36m calculations, $\Delta G_{up}^{mutation}$ and $\Delta G_{down}^{mutation}$ for glycine mutants were not provided because it is not yet possible to take the contributions of the grid-based energy correction maps (CMAP) into account when computing $\frac{\partial H}{\partial \lambda}$ in GROMACS, and that the CMAP for glycine is different from those of other amino acids. As a result, the CHARMM36m free energy estimates for glycine mutants calculated with the current protocol would be invalid.

5.2.3. Conventional MD Simulations

Mutants for 1-microsecond conventional (unbiased) simulations were generated with PyMOL [131]. The simulation setting was identical to that of the free energy calculations except for the following: only bonds associated with hydrogen atoms were constrained with the LINCS algorithm in the conventional MD simulations. For CHARMM36m simulations, a leap-frog algorithm was used as the integrator, and the Nosé–Hoover thermostat [95, 96] and the Parrinello–Rahman barostat were used to maintain the systems at 300 K and 1 bar, respectively. For every combination of systems, 10,000 energy minimization steps with the steepest descent algorithm followed by 4 to 10 independent 1-μs equilibrium simulations were carried out.

5.2.4. Residue Interaction Networks

RING 2.0 web server [135] was used to generate the residue interaction networks for TREK-2 in the crystallographic up and down states. Only main chain-side chain and side chain-side chain interactions satisfying the default distance thresholds were kept in the interaction map.

5.2.5. Difference Vector Projection

The difference vector between the up and down states was constructed from the two crystallographic conformations using the GROMACS module covar. Only C_α atoms of TREK-2 not belonging to the extracellular cap domain were used for the construction. The conventional MD simulation trajectories were then projected onto the difference vector using the GROMACS module anaeig. The projection values were re-centered and re-scaled such that a projection value of 0 and 1 mean that the conformation of TREK-2 is identical to the crystallographic down state and the crystallographic up state, respectively.

5.2.6. Intrasubunit M2/M4 Distance Profiles

d_1, d_2 and d_3 were defined as the intrasubunit distances between C_α atoms of residues 208 and 318, C_α atoms of residues 212 and 322, and C_α atoms of residues 216 and 326, respectively. d_4 was defined as the intrasubunit distances between C_α atoms of residues 280 and 316. d_5 was defined as the intersubunit distances between C_α atoms of residues 189 and 320. The first 0.5 μs of the simulations were excluded in the calculation of the

probability density functions of the distances. Errors are the 95% bootstrap confidence bands with 200 iterations of resampling.

5.2.7. Data Analysis

NumPy, pandas were used for data analysis. Matplotlib was used to generate plots. VMD [136, 137] was used to render figures for molecular visualizations. Sequence alignment was done using Jalview2 [138].

5.3. Results

5.3.1. Slow Transitions between "Up" and "Down"

Four to ten individual conventional MD simulations were carried out for the wild type (WT) and mutants of TREK-2 starting in the up or the down state. Two force fields, Amber14sb and CHARMM36m, were used. In order to identify the conformational dynamics of TREK-2, simulation trajectories were projected onto the difference vector constructed from the up and the down crystallographic conformations. A projection value of 0 and 1 mean that the conformation of TREK-2 is identical to the crystallographic down and the crystallographic up states, respectively. As illustrated in Figure 15, 35, and 36, WT and most of the mutants initially adopting the up state are highly stable in Amber14sb simulations, without undergoing a significant conformational change. In contrast, TREK-2 starting in the down state shows different degrees of instability. The difference vector projection of some simulations fluctuates about 0, representing that either both subunits are undergoing the transition between the two states or one subunit is in the up state while another subunit is in the down state. More significant conformational motions deviating from the two states are observed in CHARMM36m simulations. The projection suggests that residues such as R237 and A318, at which a stronger tendency of down-to-up transitions upon mutation is demonstrated, potentially shape the conformational equilibrium between the two states and that conformational shifts away from the down state may be induced by mutations at these residues. Although partial or complete transitions from the down state to the up state were, yet rarely, observed, no reversible transitions between the up and down states happen in any of the 1-μs simulations. The long timescale of transitions between the two conformations pose challenges to quantifying the extent of conformation shift induced by mutation using only conventional MD simulations. To

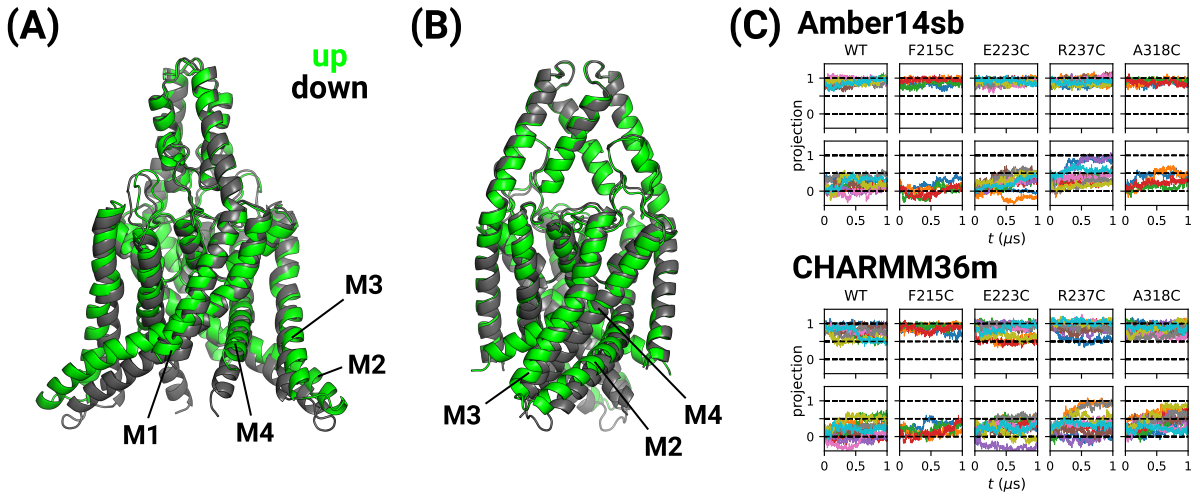

Figure 15: (**A**) Front and (**B**) side view of crystallographic up and down conformations of TREK-2. (**C**) Projection of TREK-2 onto difference vector for WT, F215C, E223C, R237C and A318C.

avoid being misguided by insufficient sampling, non-equilibrium free energy calculations were carried out to provide a complementary view of the conformational shifts brought by the mutations.

5.3.2. Destabilization of the Down State by Weakening Favorable Interactions

The non-equilibrium free energy calculations aim to estimate the free energy differences ($\Delta\Delta G$) between the crystallographic up and the crystallographic down states for TREK-2 mutants relative to WT (Figure 16A). The predicted conformational shifts due to mutations expressed in the form of $\Delta\Delta G$s are tabulated in Table 1. As position restraints were applied to backbone C_α atoms of TREK-2 during the free energy calculations to avoid them from drifting away from either the up or the down state, $\Delta\Delta G$s represent the shift in conformational preference of restrained mutants. The true extent of the shift under physiological conditions should be less significant than these estimates. Nevertheless, these $\Delta\Delta G$ estimates offer insights into the direction and magnitude of conformational shifts and allow systematic identification of residues sensitive to the conformational stability of TREK-2.

Side chains of M322 and W326 in M4 and R237 in M3 are stacked when TREK-2 is in the down state (Figure 16C). The packing of these residues is absent in the up state as M4 is kinked and rotated, causing W326 to move away from M2 and M3 of the same subunit (Figure 16B). We speculated that mutating these residues into a cysteine may disrupt the

favorable interactions that are formed exclusively in the down state and thereby shifting the conformational equilibrium away from the down state. As shown in Table 1, M322C and W326C demonstrate consistently substantial conformational shifts away from the down state ($\Delta\Delta G > 1$ kcal mol^{-1}, or 4.2 kJ mol^{-1}, for both force fields). To avoid technical complications due to the introduction of a net charge when mutating a charged residue during non-equilibrium simulations, the free energy calculation for R237C was not performed. In two of the ten Amber14sb and two of the ten CHARMM36m conventional MD simulations, R237C undergoes a transition from the down state to the up state for both monomers within the first 0.5 μs, while no complete transition in the same direction was observed in any of the simulations for WT (Figure 15C). In line with the difference vector projection, helix separation profiles (Figure 16D), which quantify the local details of the dissociation between M2 and M4 from the same subunit, reveal that the mutation R237C destabilizes the down state and facilitates a down-to-up transition while affecting the stability of the up state only slightly. The instability of the down state for these mutants is consistent with the reduced stretch activation of R237A, M322A, and W326A [29], supporting our hypothesis that the relevant residues are crucial for the conformational stability of TREK-2 and that the conformational shifts upon mutation lead to altered ion conductance of the mutants.

E223 on M2 may contribute to the conformational stability of the down state via ionic interactions with R237 on M3. However, not only does the mutation E223C, which in principle abolishes the ionic interactions, not trigger a complete transition from the down state to the up state, the mutant starting in the down state even adopts a more compact down-like conformation (difference vector projection < 0) in one Amber14sb and one CHARMM36m simulation (Figure 15C). Still, there is no strong evidence suggesting the direction of the conformational shift brought by E223C. This residue deserves a closer examination in the future as the sequence alignment for TREK-1 and TREK-2 reveals a non-conserved sequence segment appending the equivalent glutamic acid (Figure 46). While E223 in TREK-2 is followed by a cluster of positively charged residues (K224, R227, K227, and K228), three of the four equivalent appending residues are substituted by a negatively charged and two hydrophobic residues in TREK-1. The drastic difference in charge distribution may lead to a differential gating sensitivity of this residue between TREK-1 and TREK-2.

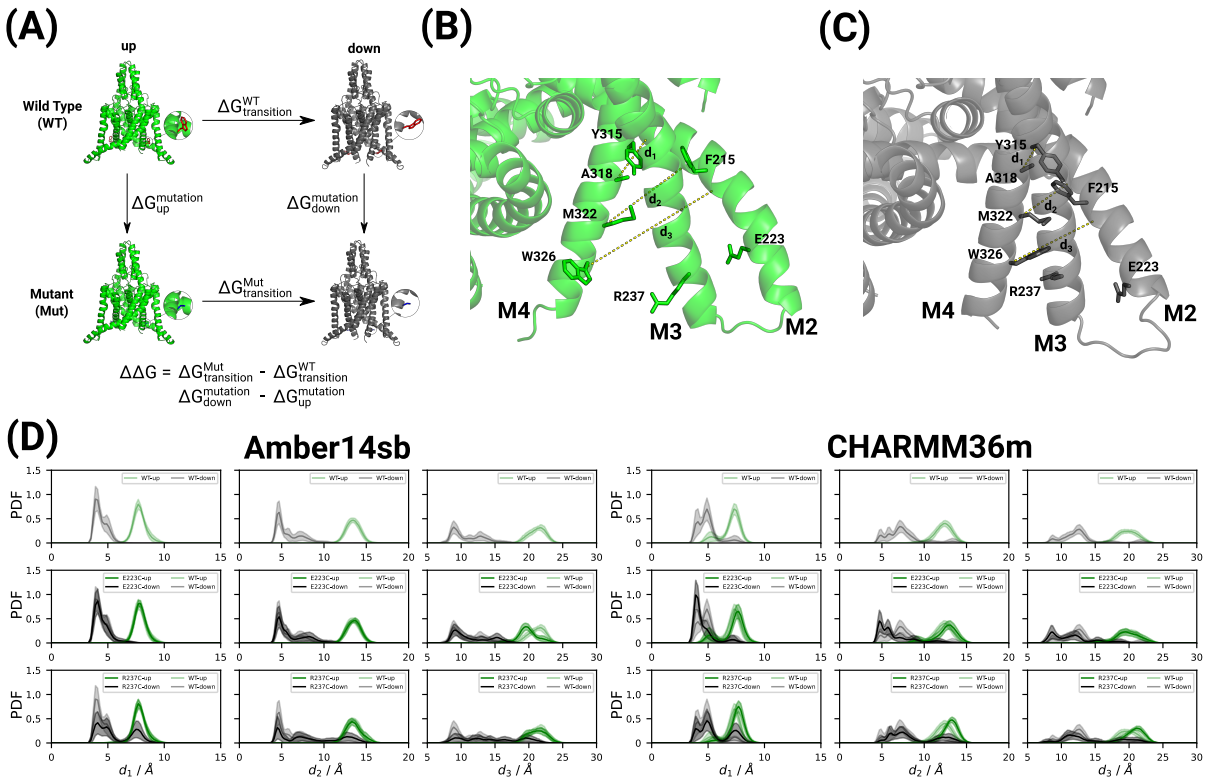

Figure 16: (**A**) Thermodynamic cycle for computing relative free energy difference $\Delta\Delta G$ between up and down states. Residues contributing to conformational equilibrium for TREK-2 WT shown in (**B**) up state and (**C**) down state. **(D)** Probability density function of d_1, d_2 and d_3 for WT, R237C and W326C.

Above the interaction core formed by R237, M322, and W326, there is another core of hydrophobic residues, including F215 and Y315 (Figure 16B and C). Mutations such as F215A and Y315A were found to reduce the stretch activation of TREK-2 significantly [29]. In good agreement with the experimental observations, our free energy calculations for F215C and Y315C suggest strong destabilization of the less conductive down state. While no significant change in conformational stability was observed from the difference vector projection for F215C, a subtle collapse of the interaction core was identified in CHARMM36m simulations starting with the down conformation (Figure 43), and the up state remained largely unaffected in both Amber14sb and CHARMM36m simulations. The observed destabilization of the down state by the two mutations can be attributed to the disruption of favorable interactions between the transmembrane helices and the reduced occlusion by the side chain at residue 215 and 315 when substituted by a shorter amino acid such as cysteine.

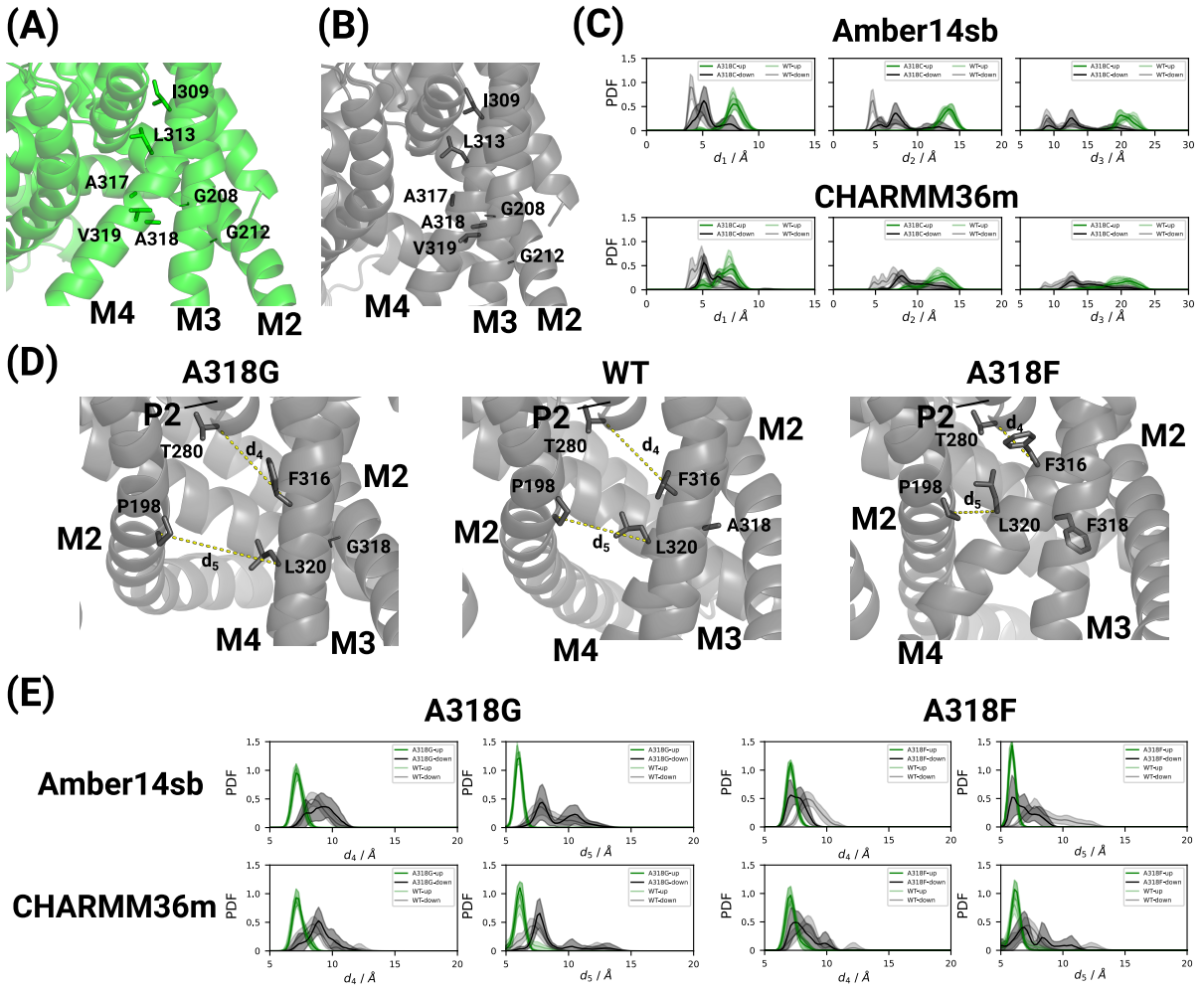

Figure 17: Residues for TREK-2 WT shown in (**A**) up state and in (**B**) down state. (**C**) Probability density function of d_1, d_2 and d_3 for A318C. (**D**) Fenestration site for NFx in A318G, WT, and A318F and (**E**) probability density function of d_4, and d_5 for A318G and A318F. The snapshot of WT in (**D**) was taken from the down crystal structure.

5.3.3. Induced Steric Clashes Shifting Conformational Equilibrium Away From Down

Supported by the free energy calculations, A318C is another mutation that destabilizes the down state substantially. Despite also being buried in the helices (Figure 17A and B), the residue interaction map (Table 8) suggests that A318 does not form interactions with surrounding residues as extensively as residues such as F215, Y315, M322, and W326. The substantial conformational shift away from the down state by A318C is accompanied by a stronger tendency of M2/M4 dissociation in the down state relative to WT shown in the distance profiles (Figure 17C). In conventional MD simulations, the conformational change of mutant A318C is driven by strengthened steric clashes inside

the interaction cores due to mutation. The additional thiol group introduced by the mutation is tolerated by the helices in the up state. However, the clashes cannot be resolved when TREK-2 is in the down state due to the tight packing of M2, M3, and M4. As a result, the mutation destabilizes and shifts the conformational equilibrium away from the down state. Several mutations at the same residue were investigated. A318F leads to a more positive value of $\Delta\Delta G$, implying even stronger destabilization of the down state. Additionally, conventional MD simulations for mutants having a longer side chain at residue 318, such as A318V, A318N, A318F, and A318Y, demonstrate a drastic increase of intrasubunit M2/M4 distances for TREK-2 starting in the down state, indicating a stronger tendency of down-to-up transitions (Figure 39, 40, 43, and 44). The free energy calculation for A318G also results in a positive $\Delta\Delta G$. Conventional MD simulations reveal that A318G undergoes a contraction of lower part of M2, M3, and M4 and adopts an even more compact conformation than the crystallographic down conformation (Figure 39 and 43). The propensity for the more compact down state is more prominent in CHARMM36m simulations. Therefore, the positive $\Delta\Delta G$ for A318G can be rationalized as the conformational shift from the down state to a more compact down-like (down+) conformation. We conclude that A318 is another critical residue determining the conformational equilibrium between the two states.

Given the strong conformational shifts included by mutations at residue 318, we calculated the opening of the fenestration site for norfluoxetine (NFx), located below P2, induced by A318G and A318F (Figure 17). Upon A318G mutation, reduced occlusion by the side chain leads to a slight increase in d_4 and d_5, indicating an expansion of the fenestration site, which would increase the accessibility of NFx to the binding site and thereby increasing the NFx sensitivity. An opposite response was observed from A318F, where the mutation induces a more compact intrasubunit P2M4 and intersubunit M2M4 packing and shrinks the fenestration site. The tight packing of the transmembrane helices around the fenestration site is comparable to that in the up state. As a result, we predict an increase and a decrease in NFx sensitivity upon mutation A318G and A318F, respectively. Our predictions are in excellent agreement with the NFx dose-response function of A318G and A318F, where the curve for the normalized current shifts towards a lower concentration and a higher concentration of NFx, respectively.

5.3.4. Mutations Altering Stability of Both Conformations

Likewise, G208 and G212 are another two sites buried in the helical bundle. From our free energy calculations, mutations G208A and G208C are predicted to destabilize the up state, while G208M is predicted to demonstrate no clear conformational shift in any direction, and G208I and G208F are predicted to destabilize the down state. The reversal of direction of the conformational shift is supported by the structural changes in the helical bundle during the conventional MD simulations: mutation G208A leads to the shortened M2/M4 separation for the up state (Figure 37 and 41). The stability of the down state is less affected by the mutation. For G208C, similar patterns, except for the slightly more prominent destabilization of the down state, were observed. We noticed comparable destabilization of the two conformations for G208M. For G208I and G208F, the destabilization of the up state is less significant than that of the down state. Unlike most identified mutations that only destabilize the down state primarily, mutations at residue 208 may alter the conformational equilibrium by influencing the stability of either or both the up state and the down state. The free energy calculations predict that G212A and G212C lower the stability of the down state. It is further supported by the apparent shift of intrasubunit M2/M4 distances in simulations starting in the down state. The free energy calculation for G212F suggests otherwise. We speculate that while the substitution of glycine by phenylalanine facilitates the expansion of the lower helical bundle in the down state due to occlusion by the side chain, the side chain of the phenylalanine strengthens the hydrophobic interactions in the core. G212F may be a mutation driving the conformational shift away from the up state by weakly stabilizing the the down state. The free energy calculations predict that the mutants L211A, L211C, and L211F would shift the equilibrium away from the up state. Intriguingly, the mutations trigger helical rearrangement in both the up and down states (Figure 38 and 42). Similar to G208, L211 may contribute to the stability of both conformations. Nevertheless, as L211 is partially exposed to the lipid bilayer, we believe that the prediction for L211 in part suffers from the drawbacks of our protocols, such as slow equilibration of lipids.

5.3.5. Facilitating Down-to-up Transitions by Reducing Side Chain Exclusion

A recent study describes L282 in TREK-1 as a fulcrum, allowing upward movement of the M4 C-terminus when switching from the down state to the up state [139]. Shortening

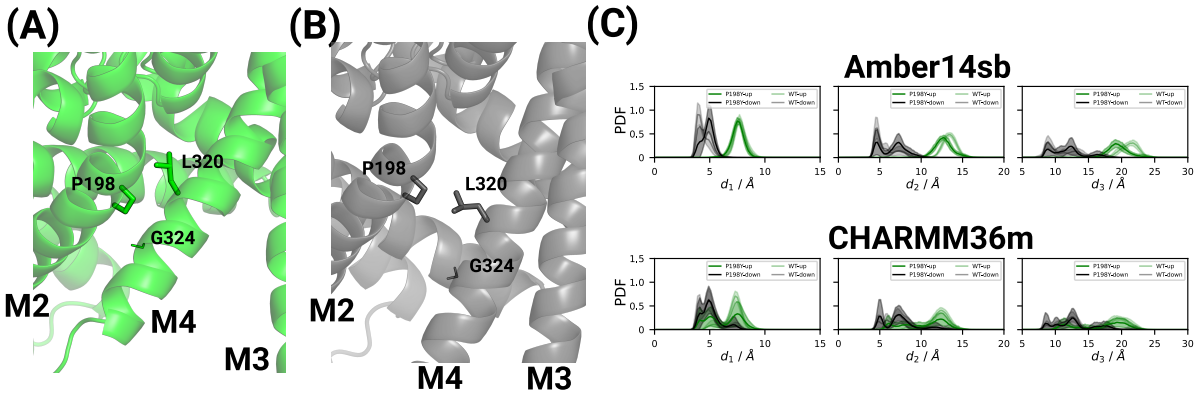

Figure 18: P198, L320, and G324 in (**A**) the up state and (**B**) the down state. **(C)** Probability density function of d_1, d_2 and d_3 for P198Y.

the side chain of this residue may promote closer contact for M4 with M2 of another subunit. We investigated the equivalent residue L313 in TREK-2. In all four CHARMM36m simulations and one of the four Amber14sb simulations, the mutant L313C initially in the down state ends in a conformation resembling the up state, consistent with the free energy calculation results that the mutation destabilizes the down state. By the same token, I309 in TREK-2 is potentially a gating-sensitive residue using the same mechanism.

5.3.6. Mutations Resulting in No Conformational Shift

We identified A317 and V319, despite being close to the interaction cores, as insensitive to conformational switching between the two conformations. The findings are consistent with the low number of conformation-dependent inter-residue interactions (Table 8). It implies that the difference between the local environment around A317 and V319 in the two conformations is minuscule. Therefore, we predict that mutations at these two residues unlikely alter the conformational equilibrium considerably.

5.3.7. Destabilization of Up by Disrupting Intersubunit M2/M4 Interface

In the up state, P198 in M2 is in close contact with residues such as L320 and G324 in M4 of the opposite subunit (Figure 18A). Mutations at these residues may undermine the stability of the up state by disrupting favorable interactions or introducing clashes on the intersubunit M2/M4 interface. Due to technical difficulties in mutating proline, only conventional MD simulations were carried out for P198Y and P198F. Shortened intrasubunit M2/M4 distances were observed for the two mutants starting in the up state

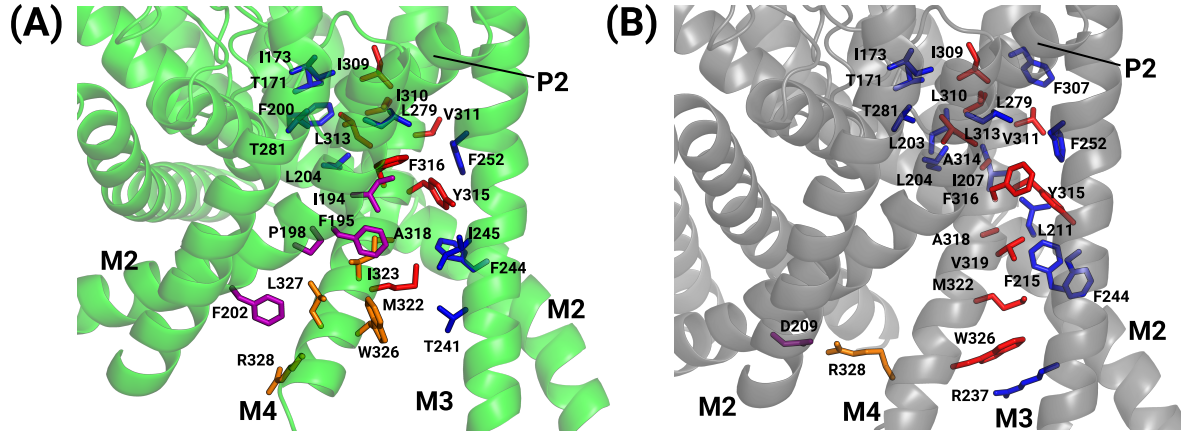

Figure 19: Residues contributing to intrasubunit and intersubunit interactions in (**A**) up state and (**B**) down state. Residues in the lower M4 segment involved in the intrasubunit and intersubunit interactions are in red and orange, respectively. Residues not in the lower M4 segment involved in the intrasubunit and intersubunit interactions are in blue and purple, respectively.

(Figure 18C, 37, and 41). Most of the identified gating-sensitive residues do not show destabilization of the up state consistently, but P198Y and P198F demonstrate consistent destabilization of exclusively the up state in Amber14sb and CHARMM36m simulations. While no significant motions of M4 were observed for L320C and G324C in the up state, free energy calculations suggest that the two mutations induce strong destabilization of the up state. As a result, P198, L320, and G324 may be essential for maintaining the stability of the up state.

5.3.8. Differences in Conformational Stability Explained by Contact Analysis

Many of the mutations in the lower M4 segment were found to destabilize the down state, and only a few mutations in M2 or M3 were consistently predicted to destabilize the up state. To explain the apparent bias of conformational stability, we turned to contact analysis, specifically identifying intrasubunit and intersubunit residue interactions in the lower M4 segment (residues 309 to 333) for TREK-2 in the two states (Figure 19 and Table 2). Our initial speculation was that the residue network formed by the down state was more extensive than the up state, therefore it was easier to find a substitution that disrupted the network and weakened the stability of the down state. However, the contact analysis suggests that both networks are comparable in terms of the total number of interaction pairs and residues involved in the network.

To investigate the apparently higher stability of the up state against mutations, we inspec-

ted the composition of the two networks and compared the intrasubunit and intersubunit interactions. There are only a small number (6) of intersubunit interaction pairs, formed between I323, W326, L327, and R328 from M4 and I194, F195, P198, and F202 from M2, likely responsible for the stability of the up state. This is in stark constant with the much higher number (20) of intrasubunit interaction pairs in the down state. In other words, it is harder to find a mutation that disrupts the intersubunit interaction in the up state, destabilizing the up state exclusively without affecting the down state, than finding a mutation that disrupts the intrasubunit interactions which promote the stability of the down state, thereby destabilizing the down state without affecting the up state.

While the network in the up state is more extended and involves residues of or close to the SF, the network in the down state is more concentrated in the compact bundle of M2, M3, and M4 from the same subunit. For instance, W326 rotates and forms a hydrophobic contact with intrasubunit residues such as M322 and R237 upon transition from the up state to the down state. The distance analysis reveals the compactness of the M2, M3, and M4 residues from the same subunit, which contributes to the stability of the down state. These suggest that mutations in the compact bundle would have a stronger influence on the conformational stability of the down state than the up state, in line with our computational results that many of the mutations at the involved residues shift the equilibrium away from the down state. Mutations at residues that belong to the up state network and are close to or part of SF may alter the stability of the up state while affecting the down state little. However, many of those are not investigated by us as the mutations are very likely to perturb the SF gate directly, which is not the focus of this work. As a result, there can be a selection bias where the up state is seemingly much more resistant than the down state against mutations. Here, based on the contact analysis, we conclude that the up state is more resistant to mutations that shift the equilibrium between the up state and the down state only and do not perturb the SF gate directly.

5.4. Discussion

Using conventional MD simulations and free energy calculations, residues contributing to the equilibrium between the crystallographic up and down states were identified. Mutations such as F215C, Y315C, M332C, and W326C destabilize the down state by weakening hydrophobic interactions between M2, M3, and M4 that are more extensively formed in

the down state. A318C is an example of mutations that induce a substantial conformational shift away from the down state by introducing unfavorable steric interactions that cannot be resolved effectively in the down state. Mutations at P198, L320, and G324 on the intersubunit M2/M4 interface destabilize the up state. From a protein engineering perspective, it is easier to find a destabilizing point mutation than a point mutation that stabilizes a certain protein conformation [140, 141]. As a result, most of the identified mutations that trigger the conformational shifts appear destabilizing. Despite the modest size of K2P channels, they can be modulated by a large class of modulators that bind in different sites of the channels. NFx is an inhibitor that can bind to a side fenestration site that is exposed when the channel is in the down state. Thus NFx can be used as a state-dependent probe [29, 42] to evaluate how mutations alter the conformational equilibrium between the two conformations by measuring the channel inhibition differential. Combined with the functional analysis and NFx inhibition measurements of TREK-1 mutants, our findings provide a molecular explanation for the observed change in channel activity of mutants, and suggest the possibility of gating via conformational switching between the up and the down states for K2P channels.

Multiple models highlighting the primary role of the SF of K2P channels in gating have been proposed [20, 21, 28]. It was also identified that the down state comes with a less stable selectivity filter that becomes non-conductive temporarily due to a higher frequency of carbonyl oxygen flips for TREK-2 [40]. A recent study concludes that the basal and mechanically activated conductance of TRAAK is characterized by the open, low conductance down state and the open, high conductance up state, respectively. Membrane tension activates TRAAK by increasing the population and lengthening the dwell time of the up state [142]. All these observations reinforce our hypothesis that the movement of M4 influences the SF gate, which acts as the primary gate for K2P channel gating.

W275S in TREK-1, equivalent to W306S in TREK-2, is a gain-of-function mutation that increases the open probability of TREK-1 [46]. We observed a moderate shift by W306C and a slight shift by L203C, T213C, and I214C away from the up state (Table 8). The relevant residues are not expected to influence the conformational equilibrium much, as they are not located in the interaction cores of M2, M3, and M4 on the cytoplasmic side of the membrane. These residues and L211 are exposed to the surrounding lipids and thus may be sensitive to the lipid arrangement around the channel. Given the short (20 ns)

equilibration prior to the non-equilibrium free energy calculations and the relatively slow dynamics of lipids, the initial conditions of the lipids and the channel may be a source of error in the calculations for residues exposed to the lipids. Additionally, the cytoplasmic domain of TREK-2 is absent in the simulations as TREK-2 crystal structures are resolved only up to the proximal C-terminus. Impacts on the gating sensitivity of these residues and the thermodynamics and kinetics of TREK-2 due to the absence of the cytoplasmic domain are yet to be established.

The free energy calculations suffer from the limitations due to applying restraints to the channel. On the one hand, backbone restraints help confine the system in the end states defined in the thermodynamic cycle to evaluate the free energy differences properly. Without the restraints, the channel often drifts quickly away from the two crystallographic conformations. On the other hand, with the restraints, only a small region of the conformational space around the two crystallographic states is taken into account. It is possible that TREK-2 explores other conformational states, such as having a partially unfolded M2-M3 loop [47], that may be relevant to the conductance of the channel. As a result, a representative ensemble for the more conductive states, including the crystallographic up state conformation, and the less conductive down states, including the crystallographic down state conformation, is required to incorporate the conformational flexibility in the free energy calculations for estimating the true extent of conformational shifts between the up state and the down state. Another downside is the overestimation of the magnitude of the conformational shifts, as there are unresolved steric clashes that should have been resolved if the position restraints on the C_α atoms of channel were not applied. In light of their limitations, we used conventional MD simulations and free energy calculations simultaneously to obtain a complementary view of conformational shifts by mutations.

5.5. Conclusions

To identify residues that determine the equilibrium between the crystallographic up state and the crystallographic down state of TREK-2, we estimated the conformational shifts brought by mutations using MD simulations and free energy calculations. Many studied mutations, which induce conformational shifts, destabilize the down state. Due to the tighter packing of residues, the down state is more vulnerable to destabilization by a point mutation at the interaction cores formed by M2, M3, and M4 from the same subunit

than the up state. The destabilization results from weakened hydrophobic interactions or induced steric clashes inside the interaction cores. Mutations that destabilize the up state exclusively or both conformations were also identified. These findings are in excellent agreement with the functional analysis and NFx sensitivity measurement of TREK-1 WT and mutants. Our work explain the molecular roles of the identified residues in the conformational equilibrium of TREK-2 and suggest that conformational switching between the up and the down state is a viable gating mechanism in TREK-1 and TREK-2.

5.6. Acknowledgment

We thank Marcus Schewe, Marianne Musinszki, and Thomas Baukrowitz for the eletrophysiology measurements of TREK-1 and TREK-2. We thank Wojciech Kopec for the discussion and advice on ion channel simulations, and Vytautas Gapsys for the advice on free energy calculations.

	$\Delta\Delta G$ (kJ/mol)			prediction			measurement†			
TREK-2	Amber14sb	CHARMM36m	free energy calculation	conventional MD	summary	TREK-1	relative P_o*	NFx IC_{50}**	consistent with MD
WT	-	-	-	-	-	WT	low Po	down	-
P198Y	-	-	-	up to down	up to down	P183Y	-	-	-
P198F	-	-	-	up to down	up to down	P183F	-	-	-
L203C	-1.06 ± 0.50	-3.15 ± 0.48	no shift	no shift	**irrelevant**	L188C	high Po	down	NFx
L204C	-4.90 ± 0.25	-2.62 ± 0.29	up to down / no shift	no shift	**irrelevant**	L189C	high Po	down	NFx
G208A	-14.97 ± 0.49		away from up	up to down	up to down	G193A	-	-	?
G208C	-17.36 ± 1.10		away from up	up to down	up to down	G193C	high Po	-	?
G208I	46.62 ± 3.04		away from down	down to up	down to up	G193I	-	-	?
G208M	-1.16 ± 1.49		no shift	both directions	?	G193M	-	-	?
G208F	32.71 ± 0.99		away from down	down to up	down to up	G193F	high Po	-	?
L211A	-7.61 ± 1.88	-12.45 ± 1.42	away from up	up to down	up to down	L196A	-	-	?
L211C	-10.32 ± 1.28	-11.42 ± 1.55	away from up	both directions	?	L196C	high Po	-	?
L211F	-42.63 ± 0.70	-37.71 ± 0.99	away from up	both directions	?	L196F	low Po	-	?
G212A	8.88 ± 0.34		away from down	?	?	G197A		-	?
G212C	9.97 ± 0.38		away from down	?	?	G197C	high Po	-	?
G212F	-5.89 ± 0.40		away from up	down to up	stabilizing new down?	G197F	high Po	-	?
T213C	-3.63 ± 0.65	-2.45 ± 0.52	no shift	no shift	**irrelevant**	T198C	high Po	down	NFx
I214C	-5.40 ± 1.82	1.45 ± 1.33	?	no shift	**irrelevant**	I199C	high Po	down	NFx
F215C	36.03 ± 0.96	26.73 ± 1.28	away from down	no shift	**down to up**	F200C	high Po	-	Po
E223C	-	-	-	no shift	no shift	E208C	high Po	up	X / ?
R237C	-	-	-	down to up	**down to up**	R222C	high Po	up	Po+NFx
W306C	-8.23 ± 3.43	-3.84 ± 1.86	away from up / no shift	no shift	**irrelevant**	W290C	high Po	down	Po+NFx
I309C	3.92 ± 0.73	4.67 ± 0.73	away from down / no shift	no shift	**down to up**	I293C	high Po	-	Po
L313C	1.25 ± 0.32	6.31 ± 0.52	away from down / no shift	down to up	**down to up**	L297C	high Po	-	Po
Y315C	12.30 ± 1.47	6.69 ± 1.21	away from down	no shift	**away from down**	Y299C	high Po	-	Po
A317C	-1.37 ± 0.35	0.34 ± 0.96	no shift	no shift	no shift	A301C	high Po	-	X
A318G	7.69 ± 0.24	-	away from down	down to down+	**down to down+**	A302G	low Po	-	Po
A318C	15.99 ± 1.63	31.69 ± 0.93	away from down	down to up	**down to up**	A302C	high Po	-	Po
A318F	73.44 ± 2.83	94.39 ± 2.55	away from down	down to up	**down to up**	A302F	high Po	-	Po
V319C	3.65 ± 0.68	-2.35 ± 0.55	no shift	no shift	**no shift**	V303C	low Po	-	Po
L320C	-21.33 ± 1.16	-8.71 ± 0.60	away from up	no shift	up to down	L304C	low Po	-	Po
M322C	24.81 ± 0.80	18.26 ± 0.83	away from down	no shift	**down to up**	M306C	high Po	-	Po
G324C	-38.19 ± 0.88	-	away from up	no shift	up to down	G308C	low Po	-	Po
W326C	10.23 ± 2.44	8.35 ± 2.13	away from down	down to up	**down to up**	W310C	high Po	up	Po+NFx

Table 1: Relative free energy differences $\Delta\Delta G$ between up and down states, and prediction of direction of equilibrium shift. The conformational equilibrium is shifted away from the crystallographic down conformation when $\Delta\Delta G > 0$. *Determined by relative open probability $P_o = \frac{I_{\text{pH8.0}}}{I_{\text{pH5.0}}}$, where $I_{\text{pH8.0}}$ and $I_{\text{pH5.0}}$ are the current at pH 8.0 and pH 5.0, respectively. **Determined by half maximal inhibitory concentration (IC_{50}) of NFx. †Measurement data provided by Marcus Schewe *et al.*.

	# interaction pairs		# residues 309-333		# residues not 309-333	
conformation	Intra	Inter	Intra	Inter	Intra	Inter
up	17	6	9	4	11	4
down	20	1	11	1	14	1

Table 2: Intrasubunit and intersubunit contact analysis for lower segment of M4 (residue 309-333). There is an interaction pair if at least one interaction between one of the residues in the lower M4 segment and one of the residues not in the lower M4 segment is identified by the residue interaction network. Only interactions that exist in both subunits are included.

6. Conclusions

The two projects elucidate the conduction properties of potassium channels from different perspectives.

6.1. Ion Conduction Mechanisms in Potassium Channels Revealed by Permeation Cycles

A systematic investigation into the multi-ion permeation processes happening in the selectivity filter of potassium channels was carried out. Using molecular dynamics simulations and Markov state modeling, permeation cycles representing ion permeation events in the selectivity filter were computed. The permeation cycles demonstrate the robustness of the direct knock-on permeation mechanism over a wide range of conditions, including potassium concentration, temperature, and voltage. These factors primarily influence ion conduction rates, while the impacts on selective filter occupancy and permeation pathways are relatively insignificant. Water co-permeation and deviations from the typical ion permeation cycles were almost only observed at voltages beyond the physiological range. Additional simulations show that direct knock-on remains the dominant permeation mechanism in different potassium channels with a highly conserved selective filter. Lastly, the charge strength dependence of permeation cycles via charge scaling and the possibility of force field optimization using the framework presented in this work were illustrated. Our results reveal the underlying details of permeation processes in the selectivity filter and help answer long-standing questions regarding permeation mechanisms in potassium channels.

6.2. Identification of Gating-Sensitive Residues in TREK-2

In the second part of the thesis, determining mutations that contribute to the rearrangement of transmembrane helices, which has been suggested to represent a gating mechanism, in TREK-2 is the main focus. To identify residues that determine the equilibrium between the crystallographic up state and the crystallographic down state of TREK-2, conformational shifts brought by mutations using MD simulations and free energy calculations were estimated. Many studied mutations, which induce a conformational shift, destabilize the down state. Due to the tighter packing of residues, the down state is

more vulnerable to destabilization by a point mutation at the interaction cores formed by M2, M3, and M4 from the same subunit than the up state. The destabilization results from weakened hydrophobic interactions or induced steric clashes inside the interaction cores. Mutations that destabilize the up state exclusively or both conformations were also identified. These findings are in excellent agreement with the functional analysis and NFx sensitivity measurement of TREK-1 WT and mutants. Our work explain the molecular roles of the identified residues in the conformational equilibrium of TREK-2 and suggest that conformational switching between the up and the down state is a viable gating mechanism in TREK-1 and TREK-2.

7. Outlook

7.1. Ion Conduction Mechanisms in Potassium Channels Revealed by Permeation Cycles

With the permeation cycle framework and its implementation in the package KPerm we develop, one can identify the effects of mutation on ion permeation. For instance, mutation F92A increases the conductance of NaK2K substantially [107], but the molecular explanation remains elusive. MD simulations with the permeation cycle analysis will provide valuable mechanistic insights. Similar analyses can be readily carried out in the future to improve our understanding of different mutants of potassium channels.

While the theoretical framework and the package are established and available for investigating the collective movement of ions in the SF, one can pursue some improvements to make the framework even more versatile. Theoretically, the framework can be easily extended to SFs with an arbitrary number of binding sites. With some adaptation in KPerm, it can analyze simulation trajectories of mutants with a non-canonical SF. The improvement will enable comparative studies such as studying KcsA mutants G77A and G77C, which were found to have a WKWK configuration in the SF. It was shown that the ion selectivity and potassium binding affinity of G77A were similar to those of KcsA WT. Thus G77A and G77C were considered as evidence supporting the water-mediated ion permeation mechanism [143]. Since the mutations occur at the SF, the mutations possibly alter the conformation of SF and distort the binding sites. As a result, MD simulations and permeation cycle analysis can reveal how the mutations influence the SF conformation and details of ion permeation mechanisms.

Next, as the conformations of the SF play a key role in ion permeation, it is desirable to incorporate structural information of the SF into the analysis to identify structural factors determining channel conductance. The outline of hierarchical Markov models is as follows: Since ion permeation is a non-equilibrium process, a variational approach for Markov processes (VAMP) can be used to identify metastable conformational states of the SF, which the transitions between these states represent the slowest dynamics in the system [77]. A Markov state model of ion occupation states is constructed for each metastable SF conformation. One can then compare the kinetics of ion permeation for each SF conformational state of SF to look for geometric details of SF for efficient ion

conduction.

7.2. Identification of Gating-Sensitive Residues in TREK-2

MD simulations and free energy calculations of TREK-2 were performed to identify residues that contribute to the stability of the up and down states. Experimental measurements of the conduction properties of TREK-1/2 WT and mutants were done by our collaborators in parallel. Both computational and experimental results suggest that many equivalent residues in TREK-1 and TREK-2 play the same role in the conduction properties, suggesting that the gating mechanism is likely conserved in TREK-1 and TREK-2. Other K2P channels may employ the same gating mechanism. For example, analogous up and down conformations of TRAAK, which share many common structural features with the two TREK-2 conformations, were resolved [38]. Therefore, the same computational and experimental protocols can be used to investigate other K2P channels to evaluate the possibility of conformational switching as a gating mechanism in K2P channel family.

Bibliography

[1] Sylvain Feliciangeli, Frank C Chatelain, Delphine Bichet, and Florian Lesage. The family of k2p channels: salient structural and functional properties. *The Journal of physiology*, 593(12):2587–2603, 2015.

[2] Char-Chang Shieh, Michael Coghlan, James P Sullivan, and Murali Gopalakrishnan. Potassium channels: molecular defects, diseases, and therapeutic opportunities. *Pharmacological reviews*, 52(4):557–594, 2000.

[3] Mark E Curran, Igor Splawski, Katherine W Timothy, G Michael Vincen, Eric D Green, and Mark T Keating. A molecular basis for cardiac arrhythmia: Herg mutations cause long qt syndrome. *Cell*, 80(5):795–803, 1995.

[4] Alan D Wickenden, Roger Kaprielian, Zamaneh Kassiri, James N Tsoporis, Robert Tsushima, Glenn I Fishman, and Peter H Backx. The role of action potential prolongation and altered intracellular calcium handling in the pathogenesis of heart failure. *Cardiovascular research*, 37(2):312–323, 1998.

[5] Ruth A Schwalbe, Laura Bianchi, Eric A Accili, and Arthur M Brown. Functional consequences of romk mutants linked to antenatal bartter's syndrome and implications for treatment. *Human molecular genetics*, 7(6):975–980, 1998.

[6] S-L Shyng and CG Nichols. Octameric stoichiometry of the katp channel complex. *The Journal of general physiology*, 110(6):655–664, 1997.

[7] T Yamada, PL McGeer, KG Baimbridge, and EG McGeer. Relative sparing in parkinson's disease of substantia nigra dopamine neurons containing calbindin-d28k. *Brain research*, 526(2):303–307, 1990.

[8] Qie Kuang, Pasi Purhonen, and Hans Hebert. Structure of potassium channels. *Cellular and molecular life sciences*, 72(19):3677–3693, 2015.

[9] Christopher Miller. An overview of the potassium channel family. *Genome biology*, 1(4):1–5, 2000.

[10] Wojciech Kopec, Brad S Rothberg, and Bert L de Groot. Molecular mechanism of a

potassium channel gating through activation gate-selectivity filter coupling. *Nature communications*, 10(1):1–15, 2019.

[11] Jianbo Dong, Ning Shi, Ian Berke, Liping Chen, and Youxing Jiang. Structures of the mthk rck domain and the effect of ca2+ on gating ring stability. *Journal of Biological Chemistry*, 280(50):41716–41724, 2005.

[12] Yang Li, Ian Berke, Liping Chen, and Youxing Jiang. Gating and inward rectifying properties of the mthk k+ channel with and without the gating ring. *The Journal of general physiology*, 129(2):109–120, 2007.

[13] Mehabaw G Derebe, David B Sauer, Weizhong Zeng, Amer Alam, Ning Shi, and Youxing Jiang. Tuning the ion selectivity of tetrameric cation channels by changing the number of ion binding sites. *Proceedings of the National Academy of Sciences*, 108(2):598–602, 2011.

[14] Declan A Doyle, Joao Morais Cabral, Richard A Pfuetzner, Anling Kuo, Jacqueline M Gulbis, Steven L Cohen, Brian T Chait, and Roderick MacKinnon. The structure of the potassium channel: molecular basis of k+ conduction and selectivity. *science*, 280(5360):69–77, 1998.

[15] Yufeng Zhou and Roderick MacKinnon. The occupancy of ions in the k+ selectivity filter: charge balance and coupling of ion binding to a protein conformational change underlie high conduction rates. *Journal of molecular biology*, 333(5):965–975, 2003.

[16] Simone Furini and Carmen Domene. Atypical mechanism of conduction in potassium channels. *Proceedings of the National Academy of Sciences*, 106(38):16074–16077, 2009.

[17] David A Köpfer, Chen Song, Tim Gruene, George M Sheldrick, Ulrich Zachariae, and Bert L de Groot. Ion permeation in k+ channels occurs by direct coulomb knock-on. *Science*, 346(6207):352–355, 2014.

[18] Andrei Mironenko, Ulrich Zachariae, Bert L de Groot, and Wojciech Kopec. The persistent question of potassium channel permeation mechanisms. *Journal of Molecular Biology*, 433(17):167002, 2021.

[19] Carl Öster, Kitty Hendriks, Wojciech Kopec, Veniamin Chevelkov, Chaowei Shi, Dagmar Michl, Sascha Lange, Han Sun, Bert L de Groot, and Adam Lange. The conduction pathway of potassium channels is water free under physiological conditions. *Science advances*, 5(7):eaaw6756, 2019.

[20] Marcus Schewe, Ehsan Nematian-Ardestani, Han Sun, Marianne Musinszki, Sönke Cordeiro, Giovanna Bucci, Bert L de Groot, Stephen J Tucker, Markus Rapedius, and Thomas Baukrowitz. A non-canonical voltage-sensing mechanism controls gating in k2p k+ channels. *Cell*, 164(5):937–949, 2016.

[21] Marco Lolicato, Andrew M Natale, Fayal Abderemane-Ali, David Crottès, Sara Capponi, Ramona Duman, Armin Wagner, John M Rosenberg, Michael Grabe, and Daniel L Minor Jr. K2p channel c-type gating involves asymmetric selectivity filter order-disorder transitions. *Science advances*, 6(44):eabc9174, 2020.

[22] Patricia S Langan, Venu Gopal Vandavasi, Kevin L Weiss, Pavel V Afonine, Kamel El Omari, Ramona Duman, Armin Wagner, and Leighton Coates. Anomalous x-ray diffraction studies of ion transport in k+ channels. *Nature communications*, 9(1):1–5, 2018.

[23] Hiroyuki Ando, Miyuki Kuno, Hirofumi Shimizu, Ikunobu Muramatsu, and Shigetoshi Oiki. Coupled k+–water flux through the herg potassium channel measured by an osmotic pulse method. *The Journal of general physiology*, 126(5):529–538, 2005.

[24] Sapar M Saparov and Peter Pohl. Beyond the diffusion limit: Water flow through the empty bacterial potassium channel. *Proceedings of the National Academy of Sciences*, 101(14):4805–4809, 2004.

[25] Torben Hoomann, Nadin Jahnke, Andreas Horner, Sandro Keller, and Peter Pohl. Filter gate closure inhibits ion but not water transport through potassium channels. *Proceedings of the National Academy of Sciences*, 110(26):10842–10847, 2013.

[26] Andrew M Natale, Parker E Deal, and Daniel L Minor Jr. Structural insights into the mechanisms and pharmacology of k2p potassium channels. *Journal of molecular biology*, 433(17):166995, 2021.

[27] Stephen G Brohawn, Josefina Del Mármol, and Roderick MacKinnon. Crystal structure of the human k2p traak, a lipid-and mechano-sensitive k+ ion channel. *Science*, 335(6067):436–441, 2012.

[28] Marco Lolicato, Cristina Arrigoni, Takahiro Mori, Yoko Sekioka, Clifford Bryant, Kimberly A Clark, and Daniel L Minor. K2p2. 1 (trek-1)–activator complexes reveal a cryptic selectivity filter binding site. *Nature*, 547(7663):364–368, 2017.

[29] Yin Yao Dong, Ashley CW Pike, Alexandra Mackenzie, Conor McClenaghan, Prafulla Aryal, Liang Dong, Andrew Quigley, Mariana Grieben, Solenne Goubin, Shubhashish Mukhopadhyay, et al. K2p channel gating mechanisms revealed by structures of trek-2 and a complex with prozac. *Science*, 347(6227):1256–1259, 2015.

[30] Karin EJ Rödström, Aytuğ K Kiper, Wei Zhang, Susanne Rinne, Ashley CW Pike, Matthias Goldstein, Linus J Conrad, Martina Delbeck, Michael G Hahn, Heinrich Meier, et al. A lower x-gate in task channels traps inhibitors within the vestibule. *Nature*, 582(7812):443–447, 2020.

[31] Alexandria N Miller and Stephen B Long. Crystal structure of the human two–pore domain potassium channel k2p1. *Science*, 335(6067):432–436, 2012.

[32] François Maingret, Amanda J Patel, Florian Lesage, Michel Lazdunski, and Eric Honoré. Mechano-or acid stimulation, two interactive modes of activation of the trek-1 potassium channel. *Journal of Biological Chemistry*, 274(38):26691–26696, 1999.

[33] Asi Cohen, Yuval Ben-Abu, Shelly Hen, and Noam Zilberberg. A novel mechanism for human k2p2. 1 channel gating: facilitation of c-type gating by protonation of extracellular histidine residues. *Journal of Biological Chemistry*, 283(28):19448–19455, 2008.

[34] Guillaume Sandoz, Dominique Douguet, Franck Chatelain, Michel Lazdunski, and Florian Lesage. Extracellular acidification exerts opposite actions on trek1 and trek2 potassium channels via a single conserved histidine residue. *Proceedings of the National Academy of Sciences*, 106(34):14628–14633, 2009.

[35] Amanda J Patel, Eric Honoré, François Maingret, Florian Lesage, Michel Fink, Fabrice Duprat, and Michel Lazdunski. A mammalian two pore domain mechano-gated s-like k+ channel. *The EMBO journal*, 17(15):4283–4290, 1998.

[36] Yangmi Kim, Carmen Gnatenco, Hyoweon Bang, and Donghee Kim. Localization of trek-2 k+ channel domains that regulate channel kinetics and sensitivity to pressure, fatty acids and phi. *Pflügers Archiv*, 442(6):952–960, 2001.

[37] Marcus Schewe, Han Sun, Ümit Mert, Alexandra Mackenzie, Ashley CW Pike, Friederike Schulz, Cristina Constantin, Kirsty S Vowinkel, Linus J Conrad, Aytug K Kiper, et al. A pharmacological master key mechanism that unlocks the selectivity filter gate in k+ channels. *Science*, 363(6429):875–880, 2019.

[38] Stephen G Brohawn, Ernest B Campbell, and Roderick MacKinnon. Physical mechanism for gating and mechanosensitivity of the human traak k+ channel. *Nature*, 516(7529):126–130, 2014.

[39] Stephen G Brohawn. How ion channels sense mechanical force: insights from mechanosensitive k2p channels traak, trek1, and trek2. *Annals of the New York Academy of Sciences*, 1352(1):20–32, 2015.

[40] Julian T Brennecke and Bert L de Groot. Mechanism of mechanosensitive gating of the trek-2 potassium channel. *Biophysical Journal*, 114(6):1336–1343, 2018.

[41] Conor McClenaghan, Marcus Schewe, Prafulla Aryal, Elisabeth P Carpenter, Thomas Baukrowitz, and Stephen J Tucker. Polymodal activation of the trek-2 k2p channel produces structurally distinct open states. *Journal of General Physiology*, 147(6):497–505, 2016.

[42] Peter Proks, Marcus Schewe, Linus J Conrad, Shanlin Rao, Kristin Rathje, Karin EJ Rödström, Elisabeth P Carpenter, Thomas Baukrowitz, and Stephen J Tucker. Norfluoxetine inhibits trek-2 k2p channels by multiple mechanisms including state-independent effects on the selectivity filter gate. *Journal of General Physiology*, 153(8):e202012812, 2021.

[43] Louise E Kennard, Justin R Chumbley, Kishani M Ranatunga, Stephanie J Armstrong, Emma L Veale, and Alistair Mathie. Inhibition of the human two-pore

domain potassium channel, trek-1, by fluoxetine and its metabolite norfluoxetine. *British journal of pharmacology*, 144(6):821, 2005.

[44] Gary Yellen. The voltage-gated potassium channels and their relatives. *nature*, 419(6902):35–42, 2002.

[45] Francisco V Sepúlveda, L Pablo Cid, Jacques Teulon, and María Isabel Niemeyer. Molecular aspects of structure, gating, and physiology of ph-sensitive background k2p and kir k+-transport channels. *Physiological Reviews*, 95(1):179–217, 2015.

[46] Sviatoslav N Bagriantsev, Rémi Peyronnet, Kimberly A Clark, Eric Honoré, and Daniel L Minor Jr. Multiple modalities converge on a common gate to control k2p channel function. *The EMBO journal*, 30(17):3594–3606, 2011.

[47] Matthew P Harrigan, Keri A McKiernan, Veerabahu Shanmugasundaram, Rajiah Aldrin Denny, and Vijay S Pande. Markov modeling reveals novel intracellular modulation of the human trek-2 selectivity filter. *Scientific reports*, 7(1):1–8, 2017.

[48] Y Zhao, S Inayat, DA Dikin, JH Singer, RS Ruoff, and JB Troy. Patch clamp technique: review of the current state of the art and potential contributions from nanoengineering. *Proceedings of the Institution of Mechanical Engineers, Part N: Journal of Nanoengineering and Nanosystems*, 222(1):1–11, 2008.

[49] Owen P Hamill, A Marty, Erwin Neher, Bert Sakmann, and Frederick J Sigworth. Improved patch-clamp techniques for high-resolution current recording from cells and cell-free membrane patches. *Pflügers Archiv*, 391(2):85–100, 1981.

[50] Martin Karplus and J Andrew McCammon. Molecular dynamics simulations of biomolecules. *Nature structural biology*, 9(9):646–652, 2002.

[51] Scott A Hollingsworth and Ron O Dror. Molecular dynamics simulation for all. *Neuron*, 99(6):1129–1143, 2018.

[52] Max Born and W Heisenberg. Zur quantentheorie der molekeln. *Original Scientific Papers Wissenschaftliche Originalarbeiten*, pages 216–246, 1985.

[53] Berk Hess, Henk Bekker, Herman JC Berendsen, and Johannes GEM Fraaije. Lincs: a linear constraint solver for molecular simulations. *Journal of computational chemistry*, 18(12):1463–1472, 1997.

[54] K Anton Feenstra, Berk Hess, and Herman JC Berendsen. Improving efficiency of large time-scale molecular dynamics simulations of hydrogen-rich systems. *Journal of computational chemistry*, 20(8):786–798, 1999.

[55] James A Maier, Carmenza Martinez, Koushik Kasavajhala, Lauren Wickstrom, Kevin E Hauser, and Carlos Simmerling. ff14sb: improving the accuracy of protein side chain and backbone parameters from ff99sb. *Journal of chemical theory and computation*, 11(8):3696–3713, 2015.

[56] Bernard R Brooks, Charles L Brooks III, Alexander D Mackerell Jr, Lennart Nilsson, Robert J Petrella, Benoît Roux, Youngdo Won, Georgios Archontis, Christian Bartels, Stefan Boresch, et al. Charmm: the biomolecular simulation program. *Journal of computational chemistry*, 30(10):1545–1614, 2009.

[57] Jing Huang, Sarah Rauscher, Grzegorz Nawrocki, Ting Ran, Michael Feig, Bert L De Groot, Helmut Grubmüller, and Alexander D MacKerell. Charmm36m: an improved force field for folded and intrinsically disordered proteins. *Nature methods*, 14(1):71–73, 2017.

[58] Alexander D MacKerell Jr. Empirical force fields for biological macromolecules: overview and issues. *Journal of computational chemistry*, 25(13):1584–1604, 2004.

[59] Viktor Hornak, Robert Abel, Asim Okur, Bentley Strockbine, Adrian Roitberg, and Carlos Simmerling. Comparison of multiple amber force fields and development of improved protein backbone parameters. *Proteins: Structure, Function, and Bioinformatics*, 65(3):712–725, 2006.

[60] Tom Darden, Darrin York, and Lee Pedersen. Particle mesh ewald: An n·log (n) method for ewald sums in large systems. *The Journal of chemical physics*, 98(12):10089–10092, 1993.

[61] Giovanni Bussi, Davide Donadio, and Michele Parrinello. Canonical sampling through velocity rescaling. *The Journal of chemical physics*, 126(1):014101, 2007.

[62] Herman JC Berendsen, JPM van Postma, Wilfred F Van Gunsteren, ARHJ DiNola, and Jan R Haak. Molecular dynamics with coupling to an external bath. *The Journal of chemical physics*, 81(8):3684–3690, 1984.

[63] Paulo CT Souza, Riccardo Alessandri, Jonathan Barnoud, Sebastian Thallmair, Ignacio Faustino, Fabian Grünewald, Ilias Patmanidis, Haleh Abdizadeh, Bart MH Bruininks, Tsjerk A Wassenaar, et al. Martini 3: a general purpose force field for coarse-grained molecular dynamics. *Nature methods*, 18(4):382–388, 2021.

[64] Siewert J Marrink, Valentina Corradi, Paulo CT Souza, Helgi I Ingolfsson, D Peter Tieleman, and Mark SP Sansom. Computational modeling of realistic cell membranes. *Chemical reviews*, 119(9):6184–6226, 2019.

[65] Carsten Kutzner, Helmut Grubmüller, Bert L De Groot, and Ulrich Zachariae. Computational electrophysiology: the molecular dynamics of ion channel permeation and selectivity in atomistic detail. *Biophysical journal*, 101(4):809–817, 2011.

[66] Carsten Kutzner, David A Köpfer, Jan-Philipp Machtens, Bert L De Groot, Chen Song, and Ulrich Zachariae. Insights into the function of ion channels by computational electrophysiology simulations. *Biochimica et Biophysica Acta (BBA)-Biomembranes*, 1858(7):1741–1752, 2016.

[67] James Gumbart, Fatemeh Khalili-Araghi, Marcos Sotomayor, and Benoît Roux. Constant electric field simulations of the membrane potential illustrated with simple systems. *Biochimica et Biophysica Acta (BBA)-Biomembranes*, 1818(2):294–302, 2012.

[68] Josef Melcr, Daniel Bonhenry, Stepan Timr, and Pavel Jungwirth. Transmembrane potential modeling: comparison between methods of constant electric field and ion imbalance. *Journal of Chemical Theory and Computation*, 12(5):2418–2425, 2016.

[69] Zoe Cournia, Bryce Allen, and Woody Sherman. Relative binding free energy calculations in drug discovery: recent advances and practical considerations. *Journal of chemical information and modeling*, 57(12):2911–2937, 2017.

[70] Daniel Seeliger and Bert L De Groot. Protein thermostability calculations using alchemical free energy simulations. *Biophysical journal*, 98(10):2309–2316, 2010.

[71] Charles H Bennett. Efficient estimation of free energy differences from monte carlo data. *Journal of Computational Physics*, 22(2):245–268, 1976.

[72] Michael R Shirts, Eric Bair, Giles Hooker, and Vijay S Pande. Equilibrium free energies from nonequilibrium measurements using maximum-likelihood methods. *Physical review letters*, 91(14):140601, 2003.

[73] Thomas J Lane, Gregory R Bowman, Kyle Beauchamp, Vincent A Voelz, and Vijay S Pande. Markov state model reveals folding and functional dynamics in ultra-long md trajectories. *Journal of the American Chemical Society*, 133(45):18413–18419, 2011.

[74] Qin Qiao, Gregory R Bowman, and Xuhui Huang. Dynamics of an intrinsically disordered protein reveal metastable conformations that potentially seed aggregation. *Journal of the American Chemical Society*, 135(43):16092–16101, 2013.

[75] Jan-Hendrik Prinz, Hao Wu, Marco Sarich, Bettina Keller, Martin Senne, Martin Held, John D Chodera, Christof Schütte, and Frank Noé. Markov models of molecular kinetics: Generation and validation. *The Journal of chemical physics*, 134(17):174105, 2011.

[76] Guillermo Pérez-Hernández, Fabian Paul, Toni Giorgino, Gianni De Fabritiis, and Frank Noé. Identification of slow molecular order parameters for markov model construction. *The Journal of chemical physics*, 139(1):07B604_1, 2013.

[77] Hao Wu and Frank Noé. Variational approach for learning markov processes from time series data. *Journal of Nonlinear Science*, 30(1):23–66, 2020.

[78] Fabian Paul, Hao Wu, Maximilian Vossel, Bert L de Groot, and Frank Noé. Identification of kinetic order parameters for non-equilibrium dynamics. *The Journal of chemical physics*, 150(16):164120, 2019.

[79] J Troy Littleton and Barry Ganetzky. Ion channels and synaptic organization: analysis of the drosophila genome. *Neuron*, 26(1):35–43, 2000.

[80] Chaowei Shi, Yao He, Kitty Hendriks, Bert L de Groot, Xiaoying Cai, Changlin Tian, Adam Lange, and Han Sun. A single nak channel conformation is not enough for non-selective ion conduction. *Nature communications*, 9(1):1–8, 2018.

[81] Joao H Morais-Cabral, Yufeng Zhou, and Roderick MacKinnon. Energetic optimization of ion conduction rate by the k+ selectivity filter. *Nature*, 414(6859):37–42, 2001.

[82] Wojciech Kopec, David A Köpfer, Owen N Vickery, Anna S Bondarenko, Thomas LC Jansen, Bert L De Groot, and Ulrich Zachariae. Direct knock-on of desolvated ions governs strict ion selectivity in k+ channels. *Nature chemistry*, 10(8):813–820, 2018.

[83] Sunhwan Jo, Taehoon Kim, Vidyashankara G Iyer, and Wonpil Im. Charmm-gui: a web-based graphical user interface for charmm. *Journal of computational chemistry*, 29(11):1859–1865, 2008.

[84] Jumin Lee, Xi Cheng, Jason M Swails, Min Sun Yeom, Peter K Eastman, Justin A Lemkul, Shuai Wei, Joshua Buckner, Jong Cheol Jeong, Yifei Qi, et al. Charmm-gui input generator for namd, gromacs, amber, openmm, and charmm/openmm simulations using the charmm36 additive force field. *Journal of chemical theory and computation*, 12(1):405–413, 2016.

[85] Sheng Ye, Yang Li, and Youxing Jiang. Novel insights into k+ selectivity from high-resolution structures of an open k+ channel pore. *Nature structural & molecular biology*, 17(8):1019–1023, 2010.

[86] Luis G Cuello, D Marien Cortes, and Eduardo Perozo. The gating cycle of a k+ channel at atomic resolution. *Elife*, 6, 2017.

[87] Stephen G Brohawn, Ernest B Campbell, and Roderick MacKinnon. Domain-swapped chain connectivity and gated membrane access in a fab-mediated crystal of the human traak k+ channel. *Proceedings of the National Academy of Sciences*, 110(6):2129–2134, 2013.

[88] Oliver Berger, Olle Edholm, and Fritz Jähnig. Molecular dynamics simulations of a fluid bilayer of dipalmitoylphosphatidylcholine at full hydration, constant pressure, and constant temperature. *Biophysical journal*, 72(5):2002–2013, 1997.

[89] Arnau Cordomí, Gianluigi Caltabiano, and Leonardo Pardo. Membrane protein

simulations using amber force field and berger lipid parameters. *Journal of chemical theory and computation*, 8(3):948–958, 2012.

[90] William L Jorgensen, Jayaraman Chandrasekhar, Jeffry D Madura, Roger W Impey, and Michael L Klein. Comparison of simple potential functions for simulating liquid water. *The Journal of chemical physics*, 79(2):926–935, 1983.

[91] In Suk Joung and Thomas E Cheatham III. Determination of alkali and halide monovalent ion parameters for use in explicitly solvated biomolecular simulations. *The journal of physical chemistry B*, 112(30):9020–9041, 2008.

[92] Jeffery B Klauda, Richard M Venable, J Alfredo Freites, Joseph W O'Connor, Douglas J Tobias, Carlos Mondragon-Ramirez, Igor Vorobyov, Alexander D MacKerell Jr, and Richard W Pastor. Update of the charmm all-atom additive force field for lipids: validation on six lipid types. *The journal of physical chemistry B*, 114(23):7830–7843, 2010.

[93] Alex D MacKerell Jr, Donald Bashford, MLDR Bellott, Roland Leslie Dunbrack Jr, Jeffrey D Evanseck, Martin J Field, Stefan Fischer, Jiali Gao, H Guo, Sookhee Ha, et al. All-atom empirical potential for molecular modeling and dynamics studies of proteins. *The journal of physical chemistry B*, 102(18):3586–3616, 1998.

[94] Dmitrii Beglov and Benoit Roux. Finite representation of an infinite bulk system: solvent boundary potential for computer simulations. *The Journal of chemical physics*, 100(12):9050–9063, 1994.

[95] Shuichi Nosé. A unified formulation of the constant temperature molecular dynamics methods. *The Journal of chemical physics*, 81(1):511–519, 1984.

[96] William G Hoover. Canonical dynamics: Equilibrium phase-space distributions. *Physical review A*, 31(3):1695, 1985.

[97] Michele Parrinello and Aneesur Rahman. Polymorphic transitions in single crystals: A new molecular dynamics method. *Journal of Applied physics*, 52(12):7182–7190, 1981.

[98] David Van Der Spoel, Erik Lindahl, Berk Hess, Gerrit Groenhof, Alan E Mark, and Herman JC Berendsen. Gromacs: fast, flexible, and free. *Journal of computational chemistry*, 26(16):1701–1718, 2005.

[99] Mark James Abraham, Teemu Murtola, Roland Schulz, Szilárd Páll, Jeremy C Smith, Berk Hess, and Erik Lindahl. Gromacs: High performance molecular simulations through multi-level parallelism from laptops to supercomputers. *SoftwareX*, 1:19–25, 2015.

[100] Frank Noé, Christof Schütte, Eric Vanden-Eijnden, Lothar Reich, and Thomas R Weikl. Constructing the equilibrium ensemble of folding pathways from short off-equilibrium simulations. *Proceedings of the National Academy of Sciences*, 106(45):19011–19016, 2009.

[101] Naveen Michaud-Agrawal, Elizabeth J Denning, Thomas B Woolf, and Oliver Beckstein. Mdanalysis: a toolkit for the analysis of molecular dynamics simulations. *Journal of computational chemistry*, 32(10):2319–2327, 2011.

[102] Richard J Gowers, Max Linke, Jonathan Barnoud, Tyler JE Reddy, Manuel N Melo, Sean L Seyler, Jan Domanski, David L Dotson, Sébastien Buchoux, Ian M Kenney, et al. Mdanalysis: a python package for the rapid analysis of molecular dynamics simulations. In *Proceedings of the 15th python in science conference*, volume 98, page 105. SciPy Austin, TX, 2016.

[103] Charles R. Harris, K. Jarrod Millman, Stéfan J. van der Walt, Ralf Gommers, Pauli Virtanen, David Cournapeau, Eric Wieser, Julian Taylor, Sebastian Berg, Nathaniel J. Smith, Robert Kern, Matti Picus, Stephan Hoyer, Marten H. van Kerkwijk, Matthew Brett, Allan Haldane, Jaime Fernández del Río, Mark Wiebe, Pearu Peterson, Pierre Gérard-Marchant, Kevin Sheppard, Tyler Reddy, Warren Weckesser, Hameer Abbasi, Christoph Gohlke, and Travis E. Oliphant. Array programming with NumPy. *Nature*, 585(7825):357–362, September 2020.

[104] Pauli Virtanen, Ralf Gommers, Travis E. Oliphant, Matt Haberland, Tyler Reddy, David Cournapeau, Evgeni Burovski, Pearu Peterson, Warren Weckesser, Jonathan Bright, Stéfan J. van der Walt, Matthew Brett, Joshua Wilson, K. Jarrod Millman, Nikolay Mayorov, Andrew R. J. Nelson, Eric Jones, Robert Kern, Eric Larson,

C J Carey, İlhan Polat, Yu Feng, Eric W. Moore, Jake VanderPlas, Denis Laxalde, Josef Perktold, Robert Cimrman, Ian Henriksen, E. A. Quintero, Charles R. Harris, Anne M. Archibald, Antônio H. Ribeiro, Fabian Pedregosa, Paul van Mulbregt, and SciPy 1.0 Contributors. SciPy 1.0: Fundamental Algorithms for Scientific Computing in Python. *Nature Methods*, 17:261–272, 2020.

[105] Aric A. Hagberg, Daniel A. Schult, and Pieter J. Swart. Exploring network structure, dynamics, and function using networkx. In Gaël Varoquaux, Travis Vaught, and Jarrod Millman, editors, *Proceedings of the 7th Python in Science Conference*, pages 11 – 15, Pasadena, CA USA, 2008.

[106] Julio F Cordero-Morales, Luis G Cuello, Yanxiang Zhao, Vishwanath Jogini, D Marien Cortes, Benoît Roux, and Eduardo Perozo. Molecular determinants of gating at the potassium-channel selectivity filter. *Nature structural & molecular biology*, 13(4):311–318, 2006.

[107] David B Sauer, Weizhong Zeng, John Canty, Yeeling Lam, and Youxing Jiang. Sodium and potassium competition in potassium-selective and non-selective channels. *Nature communications*, 4(1):1–9, 2013.

[108] Sukit Leekumjorn and Amadeu K Sum. Molecular characterization of gel and liquid-crystalline structures of fully hydrated popc and pope bilayers. *The Journal of Physical Chemistry B*, 111(21):6026–6033, 2007.

[109] Zhifeng Jing, Joshua A Rackers, Lawrence R Pratt, Chengwen Liu, Susan B Rempe, and Pengyu Ren. Thermodynamics of ion binding and occupancy in potassium channels. *Chemical science*, 12(25):8920–8930, 2021.

[110] Mounir Tarek. Membrane electroporation: a molecular dynamics simulation. *Biophysical journal*, 88(6):4045–4053, 2005.

[111] Rainer A Böckmann, Bert L De Groot, Sergej Kakorin, Eberhard Neumann, and Helmut Grubmüller. Kinetics, statistics, and energetics of lipid membrane electroporation studied by molecular dynamics simulations. *Biophysical journal*, 95(4):1837–1850, 2008.

[112] Jejoong Yoo and Aleksei Aksimentiev. New tricks for old dogs: improving the accuracy of biomolecular force fields by pair-specific corrections to non-bonded interactions. *Physical Chemistry Chemical Physics*, 20(13):8432–8449, 2018.

[113] Igor Leontyev and Alexei Stuchebrukhov. Accounting for electronic polarization in non-polarizable force fields. *Physical Chemistry Chemical Physics*, 13(7):2613–2626, 2011.

[114] Elise Duboue-Dijon, M Javanainen, P Delcroix, P Jungwirth, and H Martinez-Seara. A practical guide to biologically relevant molecular simulations with charge scaling for electronic polarization. *The Journal of Chemical Physics*, 153(5):050901, 2020.

[115] Céline Boiteux, David J Posson, Toby W Allen, and Crina M Nimigean. Selectivity filter ion binding affinity determines inactivation in a potassium channel. *Proceedings of the National Academy of Sciences*, 117(47):29968–29978, 2020.

[116] Yihao Jiang, Vinay Idikuda, Sandipan Chowdhury, and Baron Chanda. Activation of the archaeal ion channel mthk is exquisitely regulated by temperature. *Elife*, 9:e59055, 2020.

[117] Youxing Jiang, Alice Lee, Jiayun Chen, Martine Cadene, Brian T Chait, and Roderick MacKinnon. Crystal structure and mechanism of a calcium-gated potassium channel. *Nature*, 417(6888):515–522, 2002.

[118] David J Posson, Jason G McCoy, and Crina M Nimigean. The voltage-dependent gate in mthk potassium channels is located at the selectivity filter. *Nature structural & molecular biology*, 20(2):159–166, 2013.

[119] Andrew S Thomson and Brad S Rothberg. Voltage-dependent inactivation gating at the selectivity filter of the mthk k+ channel. *Journal of General Physiology*, 136(5):569–579, 2010.

[120] Brittany Zadek and Crina M Nimigean. Calcium-dependent gating of mthk, a prokaryotic potassium channel. *The Journal of general physiology*, 127(6):673–685, 2006.

[121] Carmen Domene, Riccardo Ocello, Matteo Masetti, and Simone Furini. Ion conduction mechanism as a fingerprint of potassium channels. *Journal of the American Chemical Society*, 143(31):12181–12193, 2021.

[122] Gregory C Troiano, Leslie Tung, Vinod Sharma, and Kathleen J Stebe. The reduction in electroporation voltages by the addition of a surfactant to planar lipid bilayers. *Biophysical Journal*, 75(2):880–888, 1998.

[123] Morten Ø Jensen, David W Borhani, Kresten Lindorff-Larsen, Paul Maragakis, Vishwanath Jogini, Michael P Eastwood, Ron O Dror, and David E Shaw. Principles of conduction and hydrophobic gating in k+ channels. *Proceedings of the National Academy of Sciences*, 107(13):5833–5838, 2010.

[124] Williams E Miranda, Kevin R DeMarco, Jiqing Guo, Henry J Duff, Igor Vorobyov, Colleen E Clancy, and Sergei Yu Noskov. Selectivity filter modalities and rapid inactivation of the herg1 channel. *Proceedings of the National Academy of Sciences*, 117(6):2795–2804, 2020.

[125] Takashi Sumikama and Shigetoshi Oiki. Digitalized k+ occupancy in the nanocavity holds and releases queues of k+ in a channel. *Journal of the American Chemical Society*, 138(32):10284–10292, 2016.

[126] Takashi Sumikama and Shigetoshi Oiki. Queueing arrival and release mechanism for k+ permeation through a potassium channel. *The Journal of Physiological Sciences*, 69(6):919–930, 2019.

[127] Riccardo Ocello, Simone Furini, Francesca Lugli, Maurizio Recanatini, Carmen Domene, and Matteo Masetti. Conduction and gating properties of the traak channel from molecular dynamics simulations with different force fields. *Journal of chemical information and modeling*, 60(12):6532–6543, 2020.

[128] Jay W Ponder, Chuanjie Wu, Pengyu Ren, Vijay S Pande, John D Chodera, Michael J Schnieders, Imran Haque, David L Mobley, Daniel S Lambrecht, Robert A DiStasio Jr, et al. Current status of the amoeba polarizable force field. *The journal of physical chemistry B*, 114(8):2549–2564, 2010.

[129] Mark F Schumaker and Roderick MacKinnon. A simple model for multi-ion permeation. single-vacancy conduction in a simple pore model. *Biophysical journal*, 58(4):975–984, 1990.

[130] Cinque S Soto, Marc Fasnacht, Jiang Zhu, Lucy Forrest, and Barry Honig. Loop modeling: Sampling, filtering, and scoring. *Proteins: Structure, Function, and Bioinformatics*, 70(3):834–843, 2008.

[131] Schrödinger, LLC. The PyMOL molecular graphics system, version 2.3.4. November 2015.

[132] Joakim PM Jambeck and Alexander P Lyubartsev. An extension and further validation of an all-atomistic force field for biological membranes. *Journal of chemical theory and computation*, 8(8):2938–2948, 2012.

[133] Vytautas Gapsys, Servaas Michielssens, Daniel Seeliger, and Bert L De Groot. pmx: Automated protein structure and topology generation for alchemical perturbations, 2015.

[134] Gavin E Crooks. Path-ensemble averages in systems driven far from equilibrium. *Physical review E*, 61(3):2361, 2000.

[135] Damiano Piovesan, Giovanni Minervini, and Silvio CE Tosatto. The ring 2.0 web server for high quality residue interaction networks. *Nucleic acids research*, 44(W1):W367–W374, 2016.

[136] William Humphrey, Andrew Dalke, and Klaus Schulten. VMD – Visual Molecular Dynamics. *Journal of Molecular Graphics*, 14:33–38, 1996.

[137] John Stone. *An Efficient Library for Parallel Ray Tracing and Animation*. Master's thesis, Computer Science Department, University of Missouri-Rolla, April 1998.

[138] Andrew M Waterhouse, James B Procter, David MA Martin, Michèle Clamp, and Geoffrey J Barton. Jalview version 2—a multiple sequence alignment editor and analysis workbench. *Bioinformatics*, 25(9):1189–1191, 2009.

[139] Qiansen Zhang, Jie Fu, Shaoying Zhang, Peipei Guo, Shijie Liu, Juwen Shen, Jiangtao Guo, Huaiyu Yang, and Xuebiao Yao. 'c-type'closed state and gating mech-

anisms of k2p channels revealed by conformational changes of the trek-1 channel. *Journal of molecular cell biology*, 14(1):mjac002, 2022.

[140] Mark A DePristo, Daniel M Weinreich, and Daniel L Hartl. Missense meanderings in sequence space: a biophysical view of protein evolution. *Nature Reviews Genetics*, 6(9):678–687, 2005.

[141] Linda Foit, Gareth J Morgan, Maximilian J Kern, Lenz R Steimer, Annekathrin A von Hacht, James Titchmarsh, Stuart L Warriner, Sheena E Radford, and James CA Bardwell. Optimizing protein stability in vivo. *Molecular cell*, 36(5):861–871, 2009.

[142] Robert A Rietmeijer, Ben Sorum, Baobin Li, and Stephen G Brohawn. Physical basis for distinct basal and mechanically gated activity of the human k+ channel traak. *Neuron*, 109(18):2902–2913, 2021.

[143] Cholpon Tilegenova, D Marien Cortes, Nermina Jahovic, Emily Hardy, Parameswaran Hariharan, Lan Guan, and Luis G Cuello. Structure, function, and ion-binding properties of a k+ channel stabilized in the 2, 4-ion–bound configuration. *Proceedings of the National Academy of Sciences*, 116(34):16829–16834, 2019.

A. Ion Conduction Mechanisms in Potassium Channels Revealed by Permeation Cycles

Data: SF occupancy $s[t]$ at time t in a MD trajectory of length L, number of net ion jumps $j_k[t]$ at time t of length $L-1$, chosen initial and final state S_c of the cycles
Result: list l of sub-trajectories $e_i[t']$, each representing an independent permeation cycle of length T_i

$l \leftarrow$ empty list;
$t \leftarrow 0$;
while $t < L-1$ **do**
  if $s[t] = S_c$ **then**
    $T \leftarrow 0$;
    $found \leftarrow$ **false**;
    while $T < L - t - 1$ ***and*** $found =$ ***false*** **do**
      $T \leftarrow T + 1$;
      if $s[t+T] = S_c$ **then**
        `/* compute cumulative net K+ jumps between t and t+T */`
        $n_k \leftarrow \sum_{t'=t}^{t'=t+T-1} j_k[t']$;
        if $n_k = 5$ **then**
          `/* five net ion jumps and returning to the initial state make one cycle */`
          append $s[t : t+T+1]$ to l;
          $found \leftarrow$ **True**;
        else if $n_k \leq -5$ ***or*** $n_k \geq 10$ **then**
          `/* not save it as the sub-trajectory contains more than one cycle */`
          $found \leftarrow$ **True**;
    end
    $t \leftarrow t + T - 1$;
  end
  $t \leftarrow t + 1$;
end

Algorithm 1: Identification of permeation events. See Figure 20 for the explanation of the number of net ion jumps j_k.

Data: sub-trajectory $e_i[t]$ expressing one independent permeation cycle of length T_i, and number of net ion jumps $j_{k,i}[t]$ at time t of length $T_i - 1$ corresponding to $e_i[t]$
Result: simplified sub-trajectory e_r containing one reduced permeation cycle
$t \leftarrow 0$;
$e_r \leftarrow$ empty list;
while $t < T_i - 1$ **do**
  $s_t \leftarrow e_i[t]$;
  if s_t ***not in*** e_r **then**
    append s_t to e_r;
    $I \leftarrow \{\ t' \mid e_i[t'] = s_t\}$;
    sort I in descending order;
    foreach $t' \in I$ **do**
      if $\sum_{t''=t}^{t'-1} j_{k,i}[t''] = 0$ **then**
        `/* skip transitions that eventually return to the initial state with no net ion jump */`
        $t \leftarrow t'$;
        break;
      end
    end
  end
  $t \leftarrow t + 1$;
end
append $e_i[T_i]$ to e_r;

Algorithm 2: Permeation cycle reduction. See Figure 20 for the explanation of the number of net ion jumps j_k.

name	K^+ (M)	T (K)	V (V)	$\frac{q}{q_0}$	# sims	t (ns)	# K^+ event	# water event
MthK WT	0.1	323	0.3	1.0	10	500	39,32,41,44,29, 32,14,34,15,48	0,0,0,0,0, 0,0,0,0,0
MthK WT	0.5	323	0.3	1.0	10	500	39,50,63,45,51, 30,32,66,54,46	0,0,0,0,0, 0,0,0,0,0
MthK WT	1.0	323	0.3	1.0	20	500	52,45,59,41,26, 27,52,63,72,22, 42,29,68,34,64, 57,52,51,50,58	0,0,0,0,0, 0,0,0,0,0, 0,0,0,0,0, 0,0,0,0,0
MthK WT	2.0	323	0.3	1.0	10	500	53,8,75,35,63, 29,59,58,26,36	0,0,0,0,0, 0,0,0,0,0
MthK WT	1.0	283	0.3	1.0	10	500	6,3,9,16,4, 3,14,2,2,6	0,0,0,0,0, 0,0,0,0,0
MthK WT	1.0	293	0.3	1.0	10	500	3,19,1,14,7, 1,13,13,13,13	0,0,0,0,0, 0,0,0,0,0
MthK WT	1.0	303	0.3	1.0	10	500	3,29,18,28,14, 18,27,6,25,36	0,0,0,0,0, 0,0,0,0,0
MthK WT	1.0	313	0.3	1.0	10	500	55,38,37,30,22, 16,32,37,27,13	0,0,0,0,0, 0,0,0,0,0
MthK WT	1.0	333	0.3	1.0	10	500	53,49,80,78,63, 73,75,59,56,87	0,0,0,0,0, 0,0,0,0,0
MthK WT	1.0	323	0.1	1.0	10	500	1,3,5,3,3,4,2,7,3,2	0,0,0,0,0, 0,0,0,0,0
MthK WT	1.0	323	0.2	1.0	10	500	19,14,15,34,20, 6,21,14,18,24	0,0,0,0,0, 0,0,0,0,0
MthK WT	1.0	323	0.45	1.0	10	500	82,92,106,112,97, 118,96,83,82,140	0,0,0,0,1, 0,0,0,0,0
MthK WT	1.0	323	0.6	1.0	10	500	115,109,77,88,97, 97,132,108,127,100	2,2,0,0,0, 0,1,1,0,0

Table 3: Summary of MD trajectories simulated using Amber14sb.

name	K^+ (M)	T (K)	V (V)	$\frac{q}{q_0}$	# sims	t (ns)	# K^+ event	# water event
KcsA E71A	1.0	323	0.3	1.0	20	500	19,33,37,56,30, 28,36,35,23,30, 37,34,39,24,39, 30,48,32,32,34	0,0,0,0,0, 0,0,0,0,0, 0,0,0,0,0, 0,0,0,0,0
NaK2K F92A	1.0	323	0.3	1.0	20	500	9,17,3,20,22, 27,30,20,26,31, 18,23,8,19,22, 27,23,19,22,19	0,0,0,0,0, 0,0,0,0,0, 0,0,0,0,0, 0,0,0,0,0
TRAAK WT	1.0	323	0.3	1.0	20	500	6,7,20,2,20, 7,13,8,2,7, 9,14,6,9,8, 9,7,11,7,9	0,0,0,0,0, 0,0,0,0,0, 0,0,0,0,0, 0,0,0,0,0
MthK WT	1.0	323	0.3	0.7	10	500	3,1,2,7,3,4,4,4,8,1	0,0,0,0,0, 0,0,0,0,0
MthK WT	1.0	323	0.3	0.75	10	500	28,22,31,22,22, 22,33,13,21,25	0,0,0,0,0, 0,0,0,0,0
MthK WT	1.0	323	0.3	0.8	10	500	50,31,46,44,55, 41,54,58,49,46	0,0,0,0,0, 0,0,0,0,0
MthK WT	1.0	323	0.3	0.85	10	500	33,67,13,56,64, 46,44,64,20,70	0,0,0,0,0, 0,0,0,0,0
MthK WT	1.0	323	0.3	0.9	10	500	25,24,36,13,11, 45,25,9,17,3	0,0,0,0,0, 0,0,0,0,0
MthK WT	1.0	323	0.3	0.95	10	500	13,14,20,7,11, 2,10,12,6,3	0,0,0,0,0, 0,0,0,0,0

Table 4: Summary of MD trajectories simulated using Amber14sb (continue).

name	K^+ (M)	T (K)	V (V)	$\frac{q}{q_0}$	# sims	t (ns)	# K^+ event	# water event
MthK WT	0.1	323	0.3	1.0	10	500	19,29,4,19,11, 6,9,10,8,23	0,0,0,0,0, 0,0,0,0,0
MthK WT	0.5	323	0.3	1.0	10	500	3,12,0,16,37, 14,8,22,12,23	0,0,0,0,0, 0,0,0,0,0
MthK WT	1.0	323	0.3	1.0	20	500	48,40,17,7,24, 25,19,14,36,3, 16,11,32,9,16, 17,49,8,24,10	0,0,0,0,0, 0,0,0,0,0, 0,0,0,0,0, 0,0,0,0,0
MthK WT	2.0	323	0.3	1.0	10	500	28,45,35,21,23, 20,21,28,18,22	1,0,0,0,0, 0,0,0,0,0
MthK WT	1.0	283	0.3	1.0	10	500	6,3,3,10,10, 11,11,1,3,16	0,0,0,0,0, 0,0,0,0,0
MthK WT	1.0	293	0.3	1.0	10	500	12,17,9,0,11, 2,27,6,13,9	0,0,0,0,0, 0,0,0,0,0
MthK WT	1.0	303	0.3	1.0	10	500	19,18,12,2,3, 15,13,4,20,43	0,0,0,0,0, 0,0,0,0,0
MthK WT	1.0	313	0.3	1.0	10	500	22,16,19,40,9, 2,22,23,5,4	0,0,0,0,0, 0,0,0,0,0
MthK WT	1.0	333	0.3	1.0	10	500	1,55,36,53,12, 27,14,41,39,7	0,0,0,0,0, 0,0,0,0,0
MthK WT	1.0	323	0.1	1.0	10	500	6,0,2,5,6,5,1,1,5,2	0,0,0,0,0, 0,0,0,0,0
MthK WT	1.0	323	0.2	1.0	10	500	7,6,2,5,0,6,6,4,16,9	0,0,0,0,0, 0,0,0,0,0
MthK WT	1.0	323	0.45	1.0	10	500	44,5,32,42,32, 29,28,15,28,29	0,0,0,0,1, 1,0,0,0,1
MthK WT	1.0	323	0.6	1.0	10	500	12,26,23,30,23, 31,28,7,14,14	1,1,0,0,0, 1,2,1,0,0

Table 5: Summary of MD trajectories simulated using CHARMM36m.

name	K^+ (M)	T (K)	V (V)	$\frac{q}{q_0}$	# sims	t (ns)	# K^+ event	# water event
KcsA E71A	1.0	323	0.3	1.0	20	500	26,28,20,37,8, 35,12,26,28,23, 25,41,31,41,18, 25,26,23,14,28	0,0,0,0,0, 0,0,0,0,0, 0,0,2,0,0, 0,0,2,0,0
NaK2K F92A	1.0	323	0.3	1.0	20	500	30,32,36,40,32, 35,17,37,38,30, 24,31,39,33,38, 22,31,33,27,27	0,0,0,0,0, 0,0,0,0,0, 0,0,0,0,0, 0,0,0,0,0
TRAAK WT	1.0	323	0.3	1.0	20	500	15,11,12,13,0, 10,26,16,9,15, 23,12,16,14,2, 6,14,4,1,30	1,0,0,0,0, 0,1,0,0,0, 0,0,0,0,0, 0,0,0,0,0
MthK WT	1.0	323	0.3	0.7	10	500	322,391,463,460,465, 520,426,294,447,545	0,0,0,0,0, 0,0,0,0,0
MthK WT	1.0	323	0.3	0.75	10	500	192,204,163,91,206, 127,149,136,278,222	0,0,0,0,0, 0,0,0,0,0
MthK WT	1.0	323	0.3	0.8	10	500	25,18,31,17,12, 10,15,13,50,49	0,0,0,0,0, 0,0,0,0,0
MthK WT	1.0	323	0.3	0.85	10	500	7,4,2,12,0,2,2,2,2,4	0,0,0,0,0, 0,0,0,0,0
MthK WT	1.0	323	0.3	0.9	10	500	2,0,3,2,0,1,1,0,1,0	0,0,0,0,0, 0,0,0,0,0
MthK WT	1.0	323	0.3	0.95	10	500	0,1,1,1,1,3,4,3,0,8	0,0,0,0,0, 0,0,0,0,0

Table 6: Summary of MD trajectories simulated using CHARMM36m (continue).

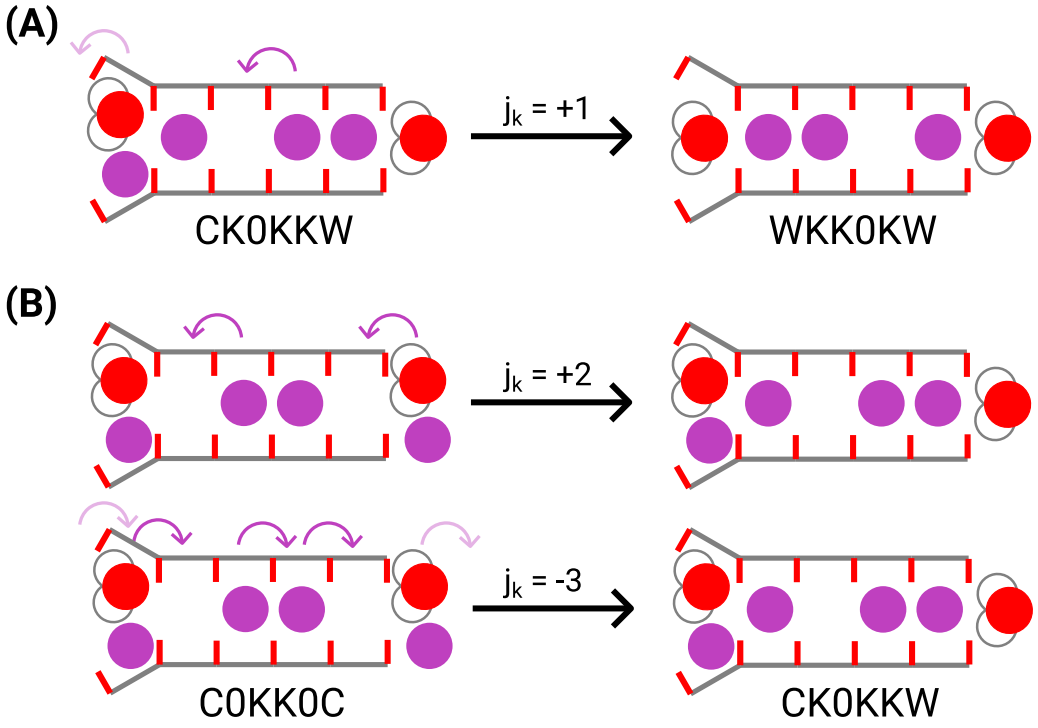

Figure 20: Ion jumps in SF.

In addition to the instantaneous SF occupation states, we kept track of the number of net ion jumps $j_k(t)$ at time t during the SF occupation state transitions. In our convention, only ion jumps to or from S1, S2, S3, or S4 are considered (Figure 20A). For example, there is a positive ion jump ($j_k = +1$) when an ion hops to the next binding site toward S0. Multiple ions hopping at the same time is possible. Water jumps $j_w(t)$ are also counted using the same convention. A complete permeation cycle is achieved by returning to the initial occupation state after time T with $\sum_{t^*=t}^{t+T-1} j_k(t^*) = +5$ net K^+ jumps in total.

Two possible transitions for C0KK0C $\rightarrow$ CK0KKW are illustrated in Figure 20B. The first transition involves two forward ion jumps, one from S2 to S1 and one from Scav to S4. This transition is relevant to the permeation cycles at a positive membrane potential. However, the second one, where three backward ion jumps are involved (the jumps from Scav to the cavity of the channel and from the extracellular side to S0 are excluded), is also possible. It implies that using only SF occupation states cannot describe permeation events uniquely. Therefore, we specified ion jumps $j_k(t)$ and water jumps $j_w(t)$ in the MSMs to avoid ambiguity.

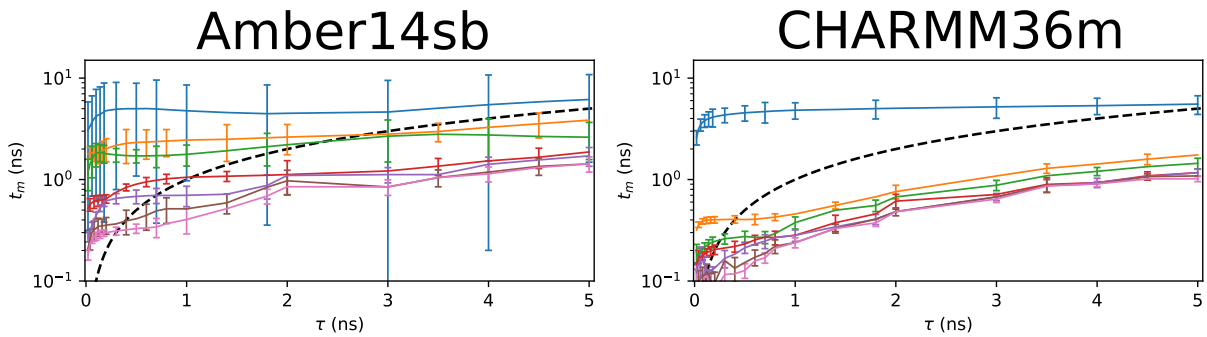

Figure 21: Relaxation time t_m of slowest dynamics ($2 \leq m \leq 7$) as function of lag time τ for MthK WT simulated at 323 K and 300 mV in 1 M KCl solution using Amber14sb and CHARMM36m. Errors are the normal-based 95% bootstrap intervals ($B = 100$). In each bootstrap iteration, MD trajectories were resampled with replacement to compute a transition matrix for eigendecomposition.

For an ideal MSM, the relaxation time t_m is a constant, independent of the choice of lag time τ. The relaxation times t_m for $m > 2$ increases with τ because τ is comparable to or longer than the relaxation times, therefore overestimating the timescales (Figure 21). We argue that using the convergence of the first M relaxation times to evaluate the deviation from the ideal Markov process is not comprehensive. It rests on the assumption that the motions of interest are the slowest motions in the simulated system. This assumption, however, does not hold in the context of ion permeation, as a complete ion permeation event consists of processes occurring on a wide range of timescales from tens of picoseconds to tens of nanoseconds. The fastest permeation step WK0KKW $\rightarrow$ WKK0KW has a MFPT of 30 ps and 50 ps for Amber14sb and CHARMM36m, respectively. Using a large τ results in an overestimation of the timescales of fast processes. Furthermore, inspecting components in the eigenvectors reveals that the slowest motion ($m = 2$) in AMBER simulations is irrelevant to ion permeation as this motion refers to the transitions between typical conductive states, such as WKK0KW, C0KK0C, and WK0KKW, and non-conductive states with S1 filled with water, such as CWK0KW and CWK0KC, that are absent in the permeation cycles. As a result, we did not choose the value of τ only based on the convergence of the first few relaxation times.

We instead performed Chapman-Kolmogorov test via observing the relaxation in the Markov chain (MC) simulations based on the transition matrices derived from MD data (Figures 22 and 23). We evaluated the probability of staying in one of the most frequently observed SF occupation states, given that the system started in the same state. This

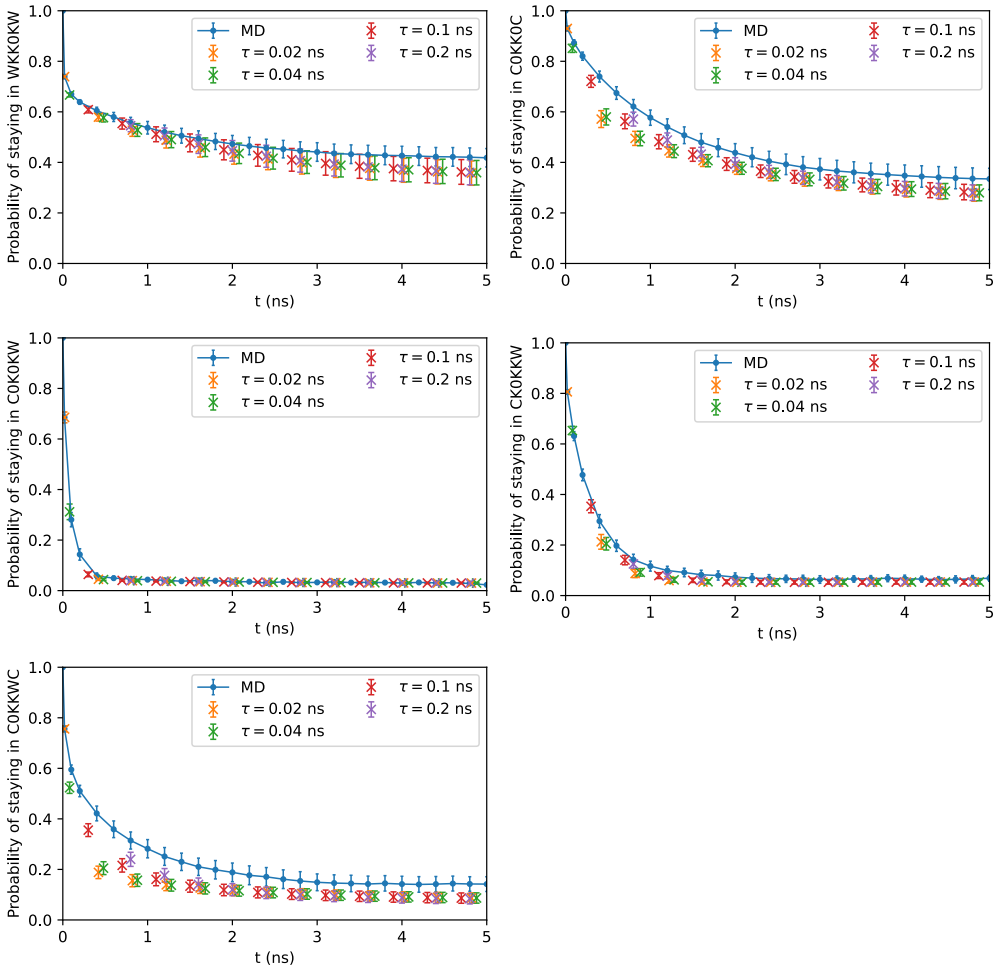

Figure 22: Chapman-Kolmogorov test for relaxation in Markov chains for MthK WT simulated at 300mV and 323 K in 1 M KCl using Amber14sb. The first three most abundant states were chosen. Errors represent 95% normal-based bootstrap intervals ($B = 100$). In each bootstrap iteration, MD trajectories were resampled with replacement to compute a transition matrix used by the MC simulation for the estimation of the probability. The dashed lines indicate the steady-state distributions of the selected SF occupation states.

is a harsh test for Markovianity, as a thorough sampling of transitions into and out of the metastable states is required [75, 78]. Furthermore, we compared the transition probabilities observed from MD and predicted by the MSMs using $\tau = 20$ ps (Figures 33 and 34). Since a lag time as small as 20 ps can reproduce the MD results reasonably well, τ was chosen to be 20 ps for all MSMs. A small τ is preferable to reduce the overestimation of the mean first passage times of fast permeation steps (Figure 24) and $\tau = 20$ ps reproduces the ionic currents very well (Figure 26 and 27).

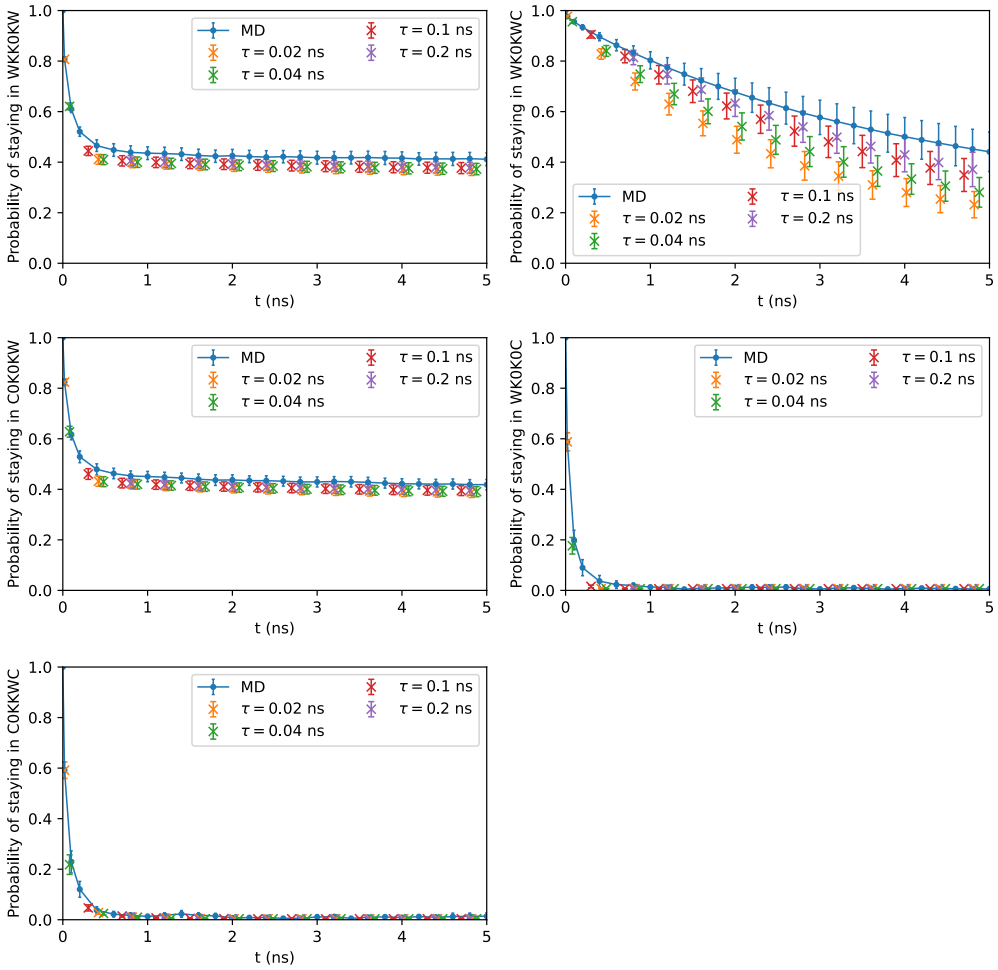

Figure 23: Chapman-Kolmogorov test for relaxation in Markov chains for MthK WT simulated at 300mV and 323 K in 1 M KCl using CHARMM36m. The first three most abundant states were chosen. Errors represent 95% normal-based bootstrap intervals ($B = 100$). In each bootstrap iteration, MD trajectories were re-sampled with replacement to compute a transition matrix used by the MC simulation for the estimation of the probability. The dashed lines indicate the steady-state distributions of the selected SF occupation states.

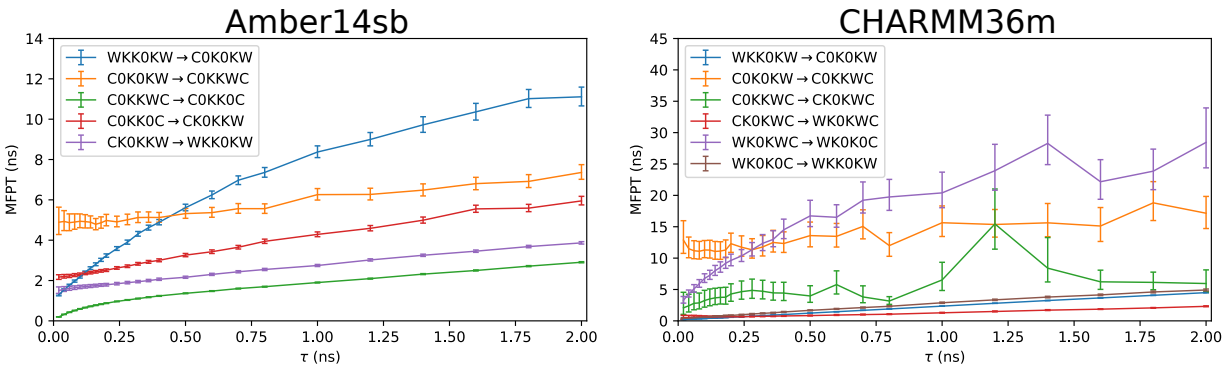

Figure 24: Mean first passage times of SF occupation state transitions as function of lag time τ for MthK WT simulated at 300mV and 323 K in 1 M KCl. Errors of MFPTs are bias-corrected and accelerated (BCa) 95% bootstrap intervals ($B = 10000$) computed from the observed values of first passage times in MD simulations.

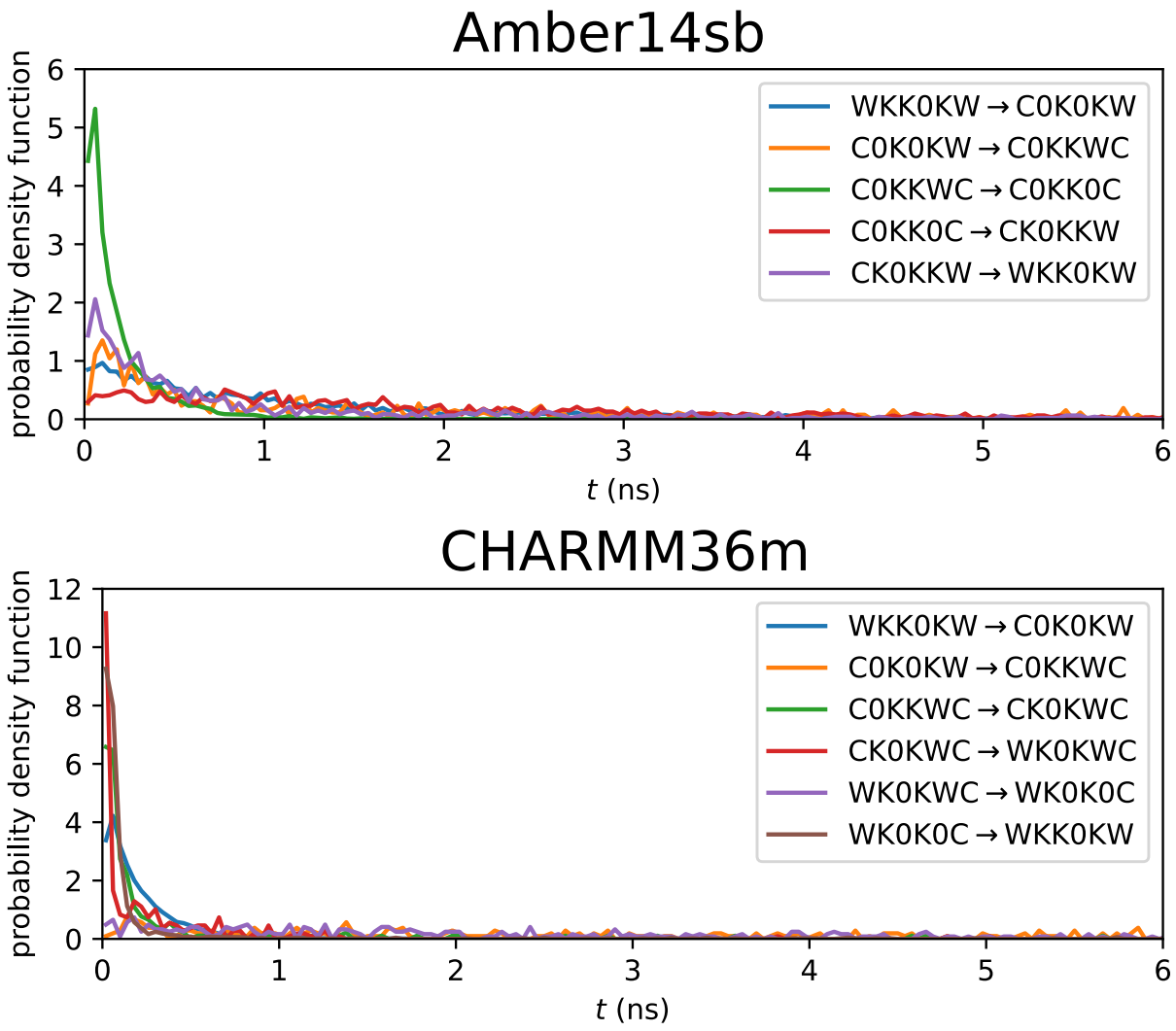

Figure 25: Probability density functions of first passage times of SF occupation state transitions for MthK WT simulated at 300mV and 323 K in 1 M KCl.

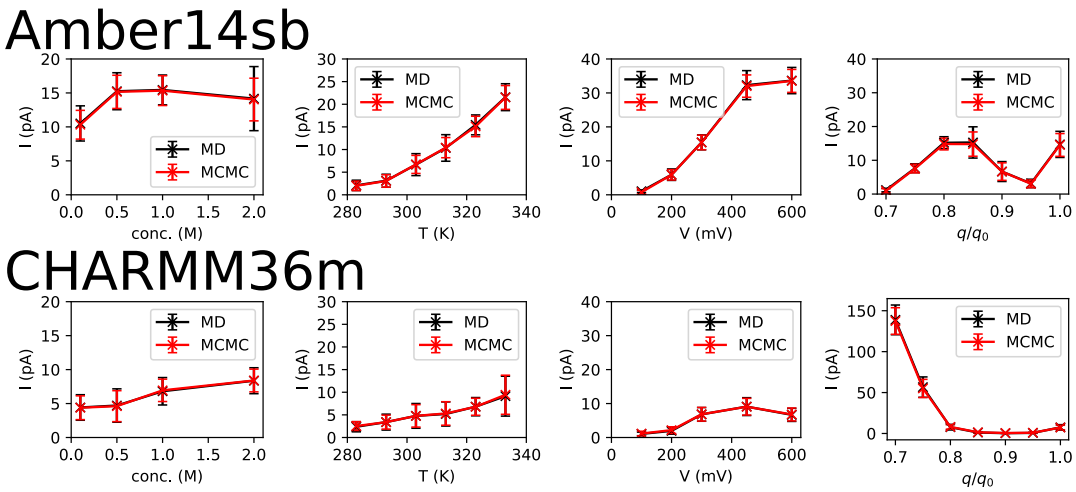

Figure 26: Currents observed in MD and MC simulations for MthK WT simulated at 300mV and 323 K in 1 M KCl. Uncertainty for the MD simulations is the 95% confidence intervals using the t-distribution. Uncertainty for the MC simulations is the 95% normal-based bootstrap intervals ($B = 100$). In each bootstrap iteration, MD trajectories were re-sampled with replacement to compute a transition matrix used by the MC simulation for the estimation of the current.

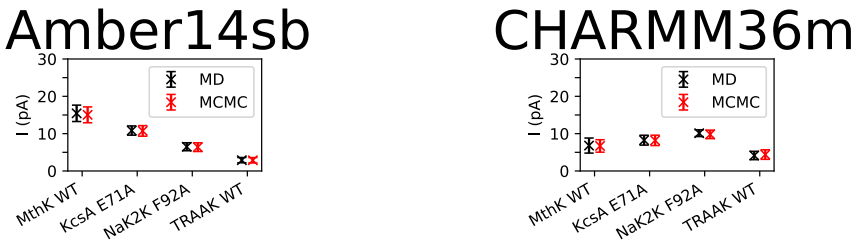

Figure 27: Currents in MD and MC simulations for MthK WT, KcsA E71A, NaK2K F92A, and TRAAK WT simulated at 300mV and 323 K in 1 M KCl. Uncertainty for the MD simulations is the 95% confidence intervals using the t-distribution. Uncertainty for the MD simulations is the 95% confidence intervals using the t-distribution. Uncertainty for the MC simulations is the 95% normal-based bootstrap intervals ($B = 100$). In each bootstrap iteration, MD trajectories were re-sampled with replacement to compute a transition matrix used by the MC simulation for the estimation of the current.

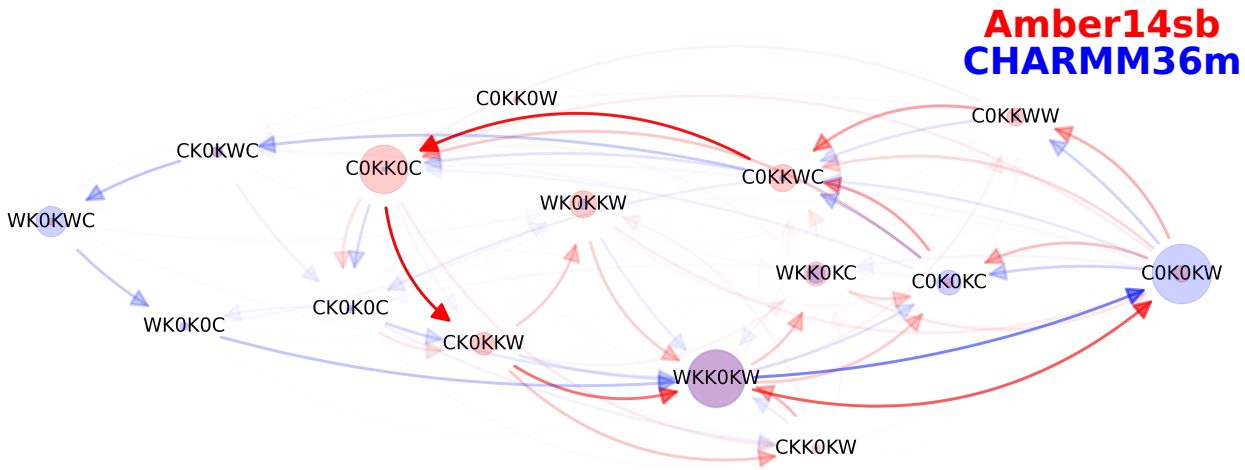

Figure 28: Net fluxes between SF occupation states for MthK WT at 300 mV and 323 K in 1 M KCl. Node sizes scale with the steady-state distributions of the SF occupation states. Edges represent the net fluxes between states. Only the net fluxes larger than 0.1 of the maximum among all net fluxes are shown.

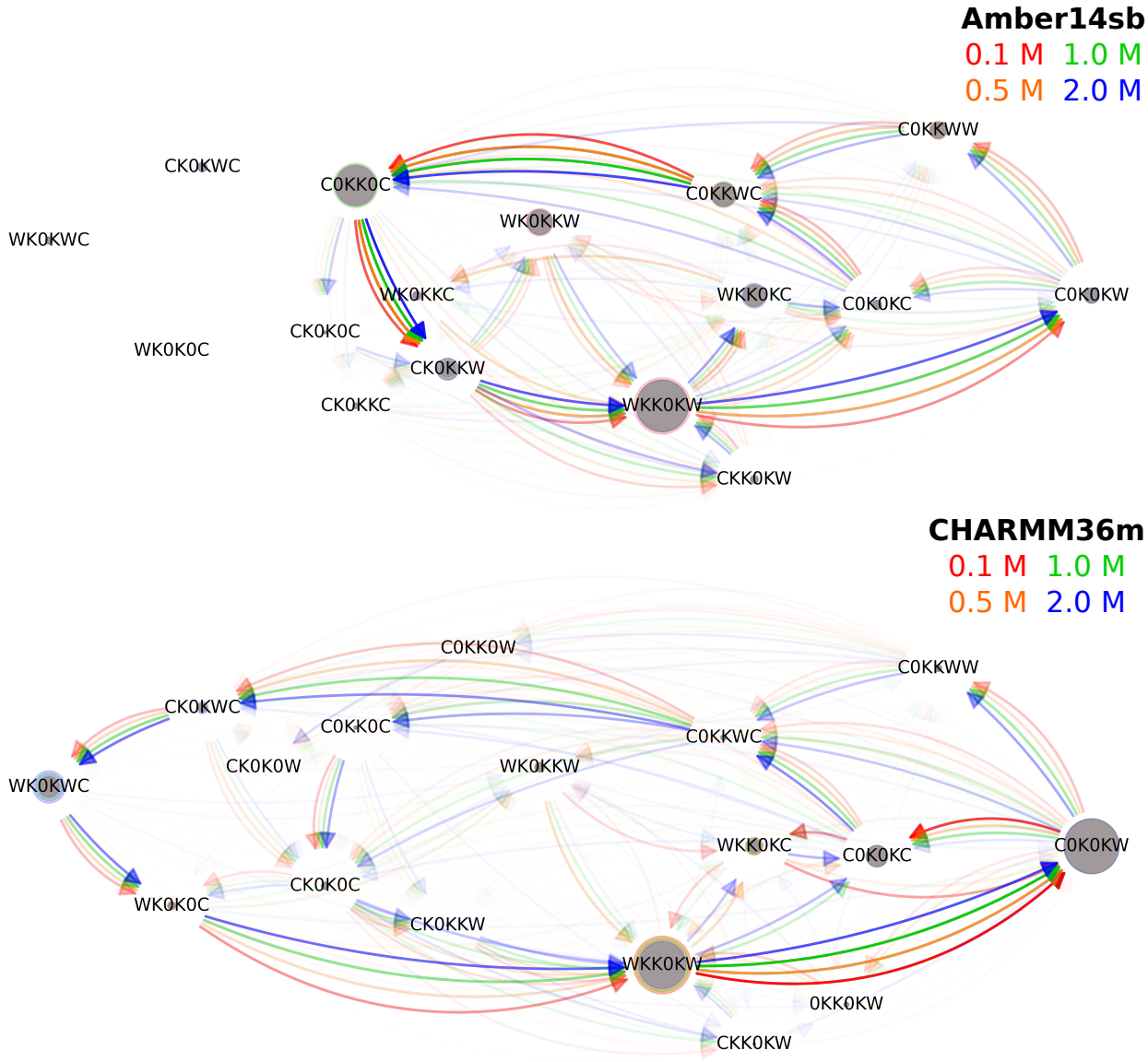

Figure 29: Net fluxes between SF occupation states for MthK WT at 300 mV and 323 K in KCl of different concentrations. Node sizes scale with the steady-state distributions of the SF occupation states. Edges represent the net fluxes between states. Only the net fluxes larger than 0.1 of the maximum among all net fluxes are shown.

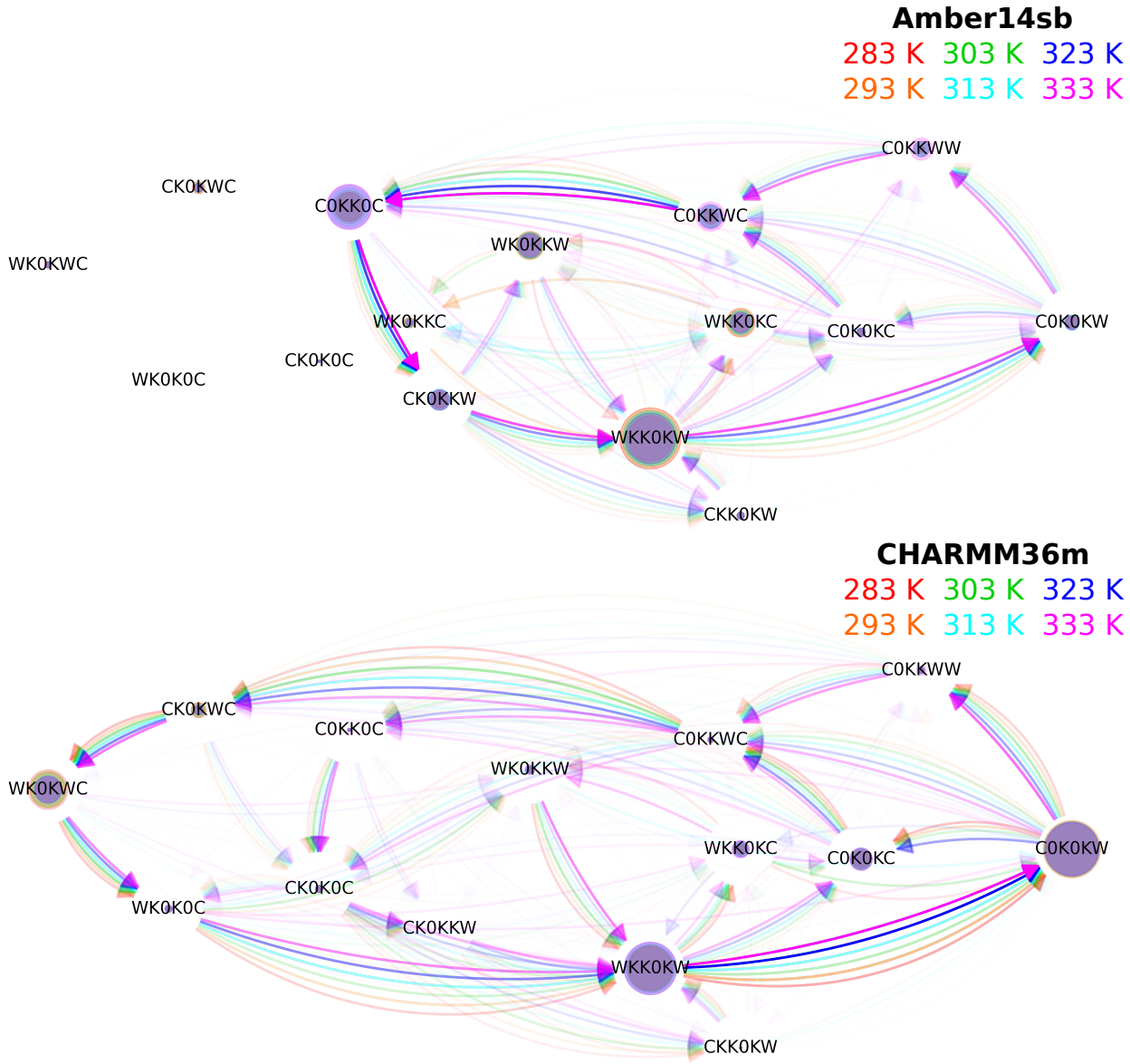

Figure 30: Net fluxes between SF occupation states for MthK WT at 300 mV and different temperature in 1 M KCl. Node sizes scale with the steady-state distributions of the SF occupation states. Edges represent the net fluxes between states. Only the net fluxes larger than 0.1 of the maximum among all net fluxes are shown.

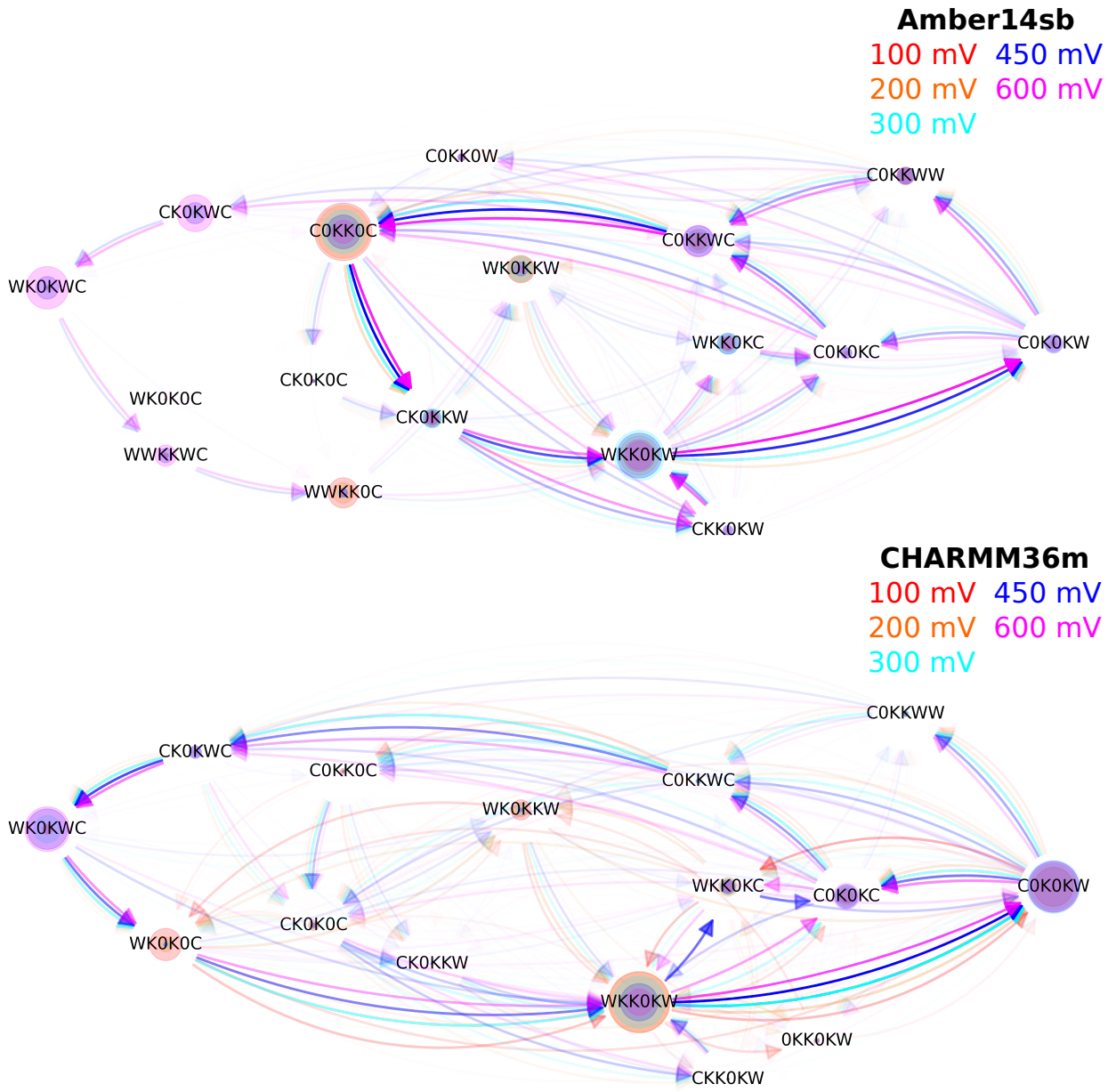

Figure 31: Net fluxes between SF occupation states for MthK WT at different membrane voltage and 323 K in 1 M KCl. Node sizes scale with the steady-state distributions of the SF occupation states. Edges represent the net fluxes between states. Only the net fluxes larger than 0.1 of the maximum among all net fluxes are shown.

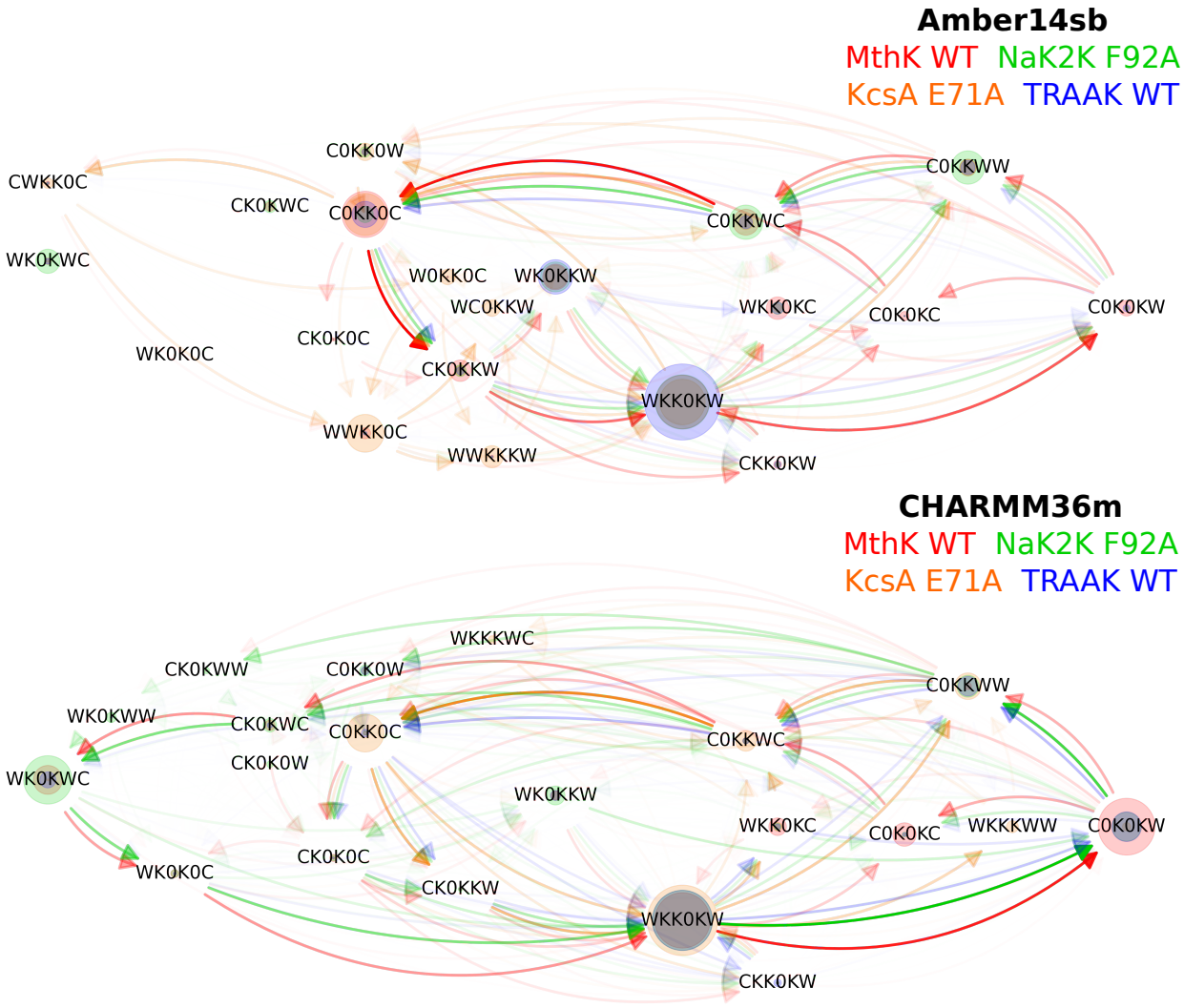

Figure 32: Net fluxes between SF occupation states for MthK WT, KcsA E71A, NaK2K F92A, and TRAAK WT at 300 mV and 323 K in 1 M KCl. Node sizes scale with the steady-state distributions of the SF occupation states. Edges represent the net fluxes between states. Only the net fluxes larger than 0.1 of the maximum among all net fluxes are shown.

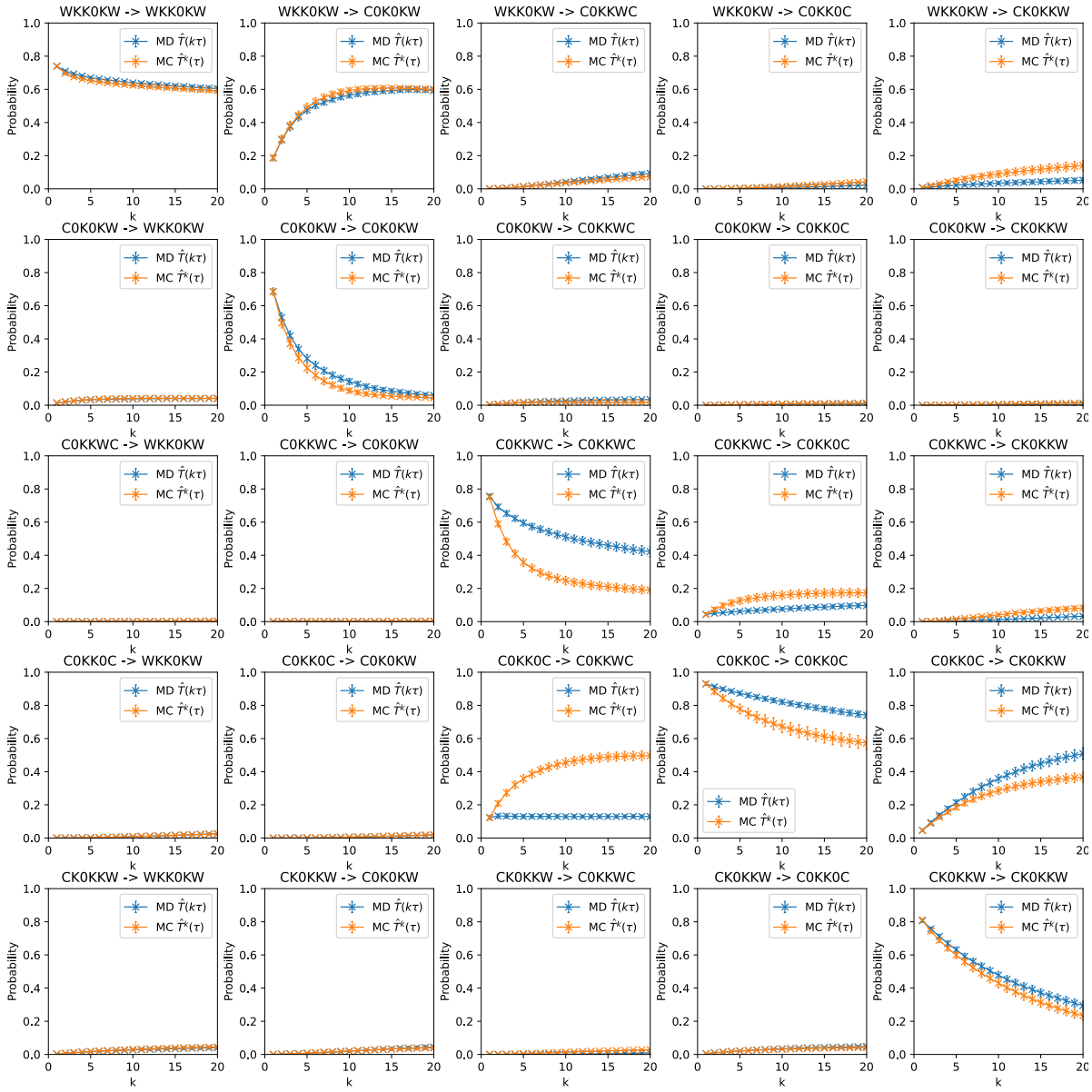

Figure 33: Chapman-Kolmogorov test with $\tau = 20$ ps for MthK WT simulated at 300mV and 323 K in 1 M KCl using Amber14sb. The five states, in which the first three most frequently observed states in MD are also included, involved in most of the observed permeation cycles were chosen. Errors represent 95% normal-based bootstrap intervals ($B = 100$). In each bootstrap iteration for the uncertainty of MC simulations, MD trajectories were re-sampled with replacement to compute the transition matrix $\hat{\boldsymbol{T}}^k(\tau)$, for $k = 1, 2, ..., 20$.

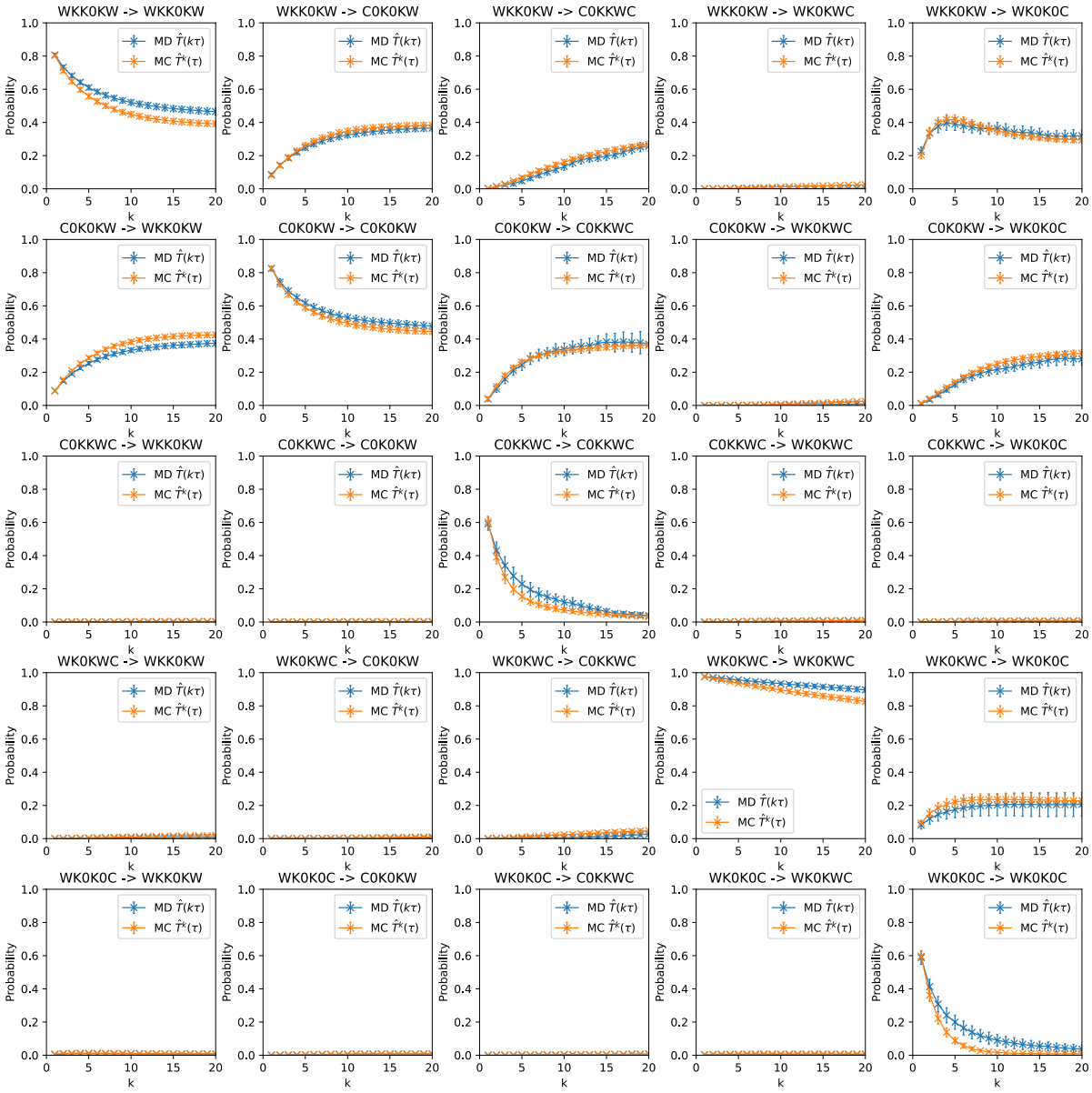

Figure 34: Chapman-Kolmogorov test with $\tau = 20$ ps for MthK WT simulated at 300mV and 323 K in 1 M KCl using CHARMM36m. The five states, in which the first three most frequently observed states in MD are also included, involved in most of the observed permeation cycles were chosen. Errors represent 95% normal-based bootstrap intervals ($B = 100$). In each bootstrap iteration for the uncertainty of MC simulations, MD trajectories were re-sampled with replacement to compute the transition matrix $\hat{\boldsymbol{T}}^k(\tau)$, for $k = 1, 2, ..., 20$.

B. Identification of Gating-Sensitive Residues in TREK-2

	$\Delta\Delta G$ (kJ/mol)		prediction	
mutant	Amber14sb	CHARMM36m	free energy calculation	conventional MD
L310C	1.49 ± 1.10	-4.10 ± 1.19	no shift	-
V311C	-28.5 ± 0.74	-24.2 ± 1.14	away from up	-
G312C	4.81 ± 1.19	-	away from down	-
L313F	-13.10 ± 1.40	6.92 ± 3.45	?	-
L313I	-7.23 ± 2.14	-6.93 ± 1.50	away from up	-
L313M	4.54 ± 0.53	8.05 ± 0.80	away from down	-
L313V	-10.41 ± 3.03	-6.67 ± 1.33	away from up	-
L313S	0.61 ± 0.75	4.94 ± 0.90	away from down / no shift	-
A314C	7.52 ± 2.61	7.53 ± 2.47	away from down	-
F316C	6.32 ± 1.67	5.85 ± 1.09	away from down	-
A318N	49.38 ± 2.13	73.00 ± 1.49	away from down	-
A318V	54.93 ± 0.81	49.84 ± 0.49	away from down	-
A318Y	88.81 ± 2.97	111.97 ± 2.85	away from down	-
S321C	-2.12 ± 0.26	-3.24 ± 0.38	no shift	-
I323C	-27.71 ± 1.30	-21.16 ± 1.90	away from up	-
L327C	-27.18 ± 1.12	-20.67 ± 1.14	away from up	-
V329C	3.50 ± 0.42	5.02 ± 0.27	away from down / no shift	-
L330C	-4.92 ± 0.80	-5.63 ± 1.59	away from up	-
S331C	4.75 ± 1.05	7.66 ± 1.46	away from down	-

Table 7: Relative free energy differences $\Delta\Delta G$ between up and down states, and prediction of direction of equilibrium shift. The conformational equilibrium is shifted away from the crystallographic down conformation when $\Delta\Delta G > 0$.

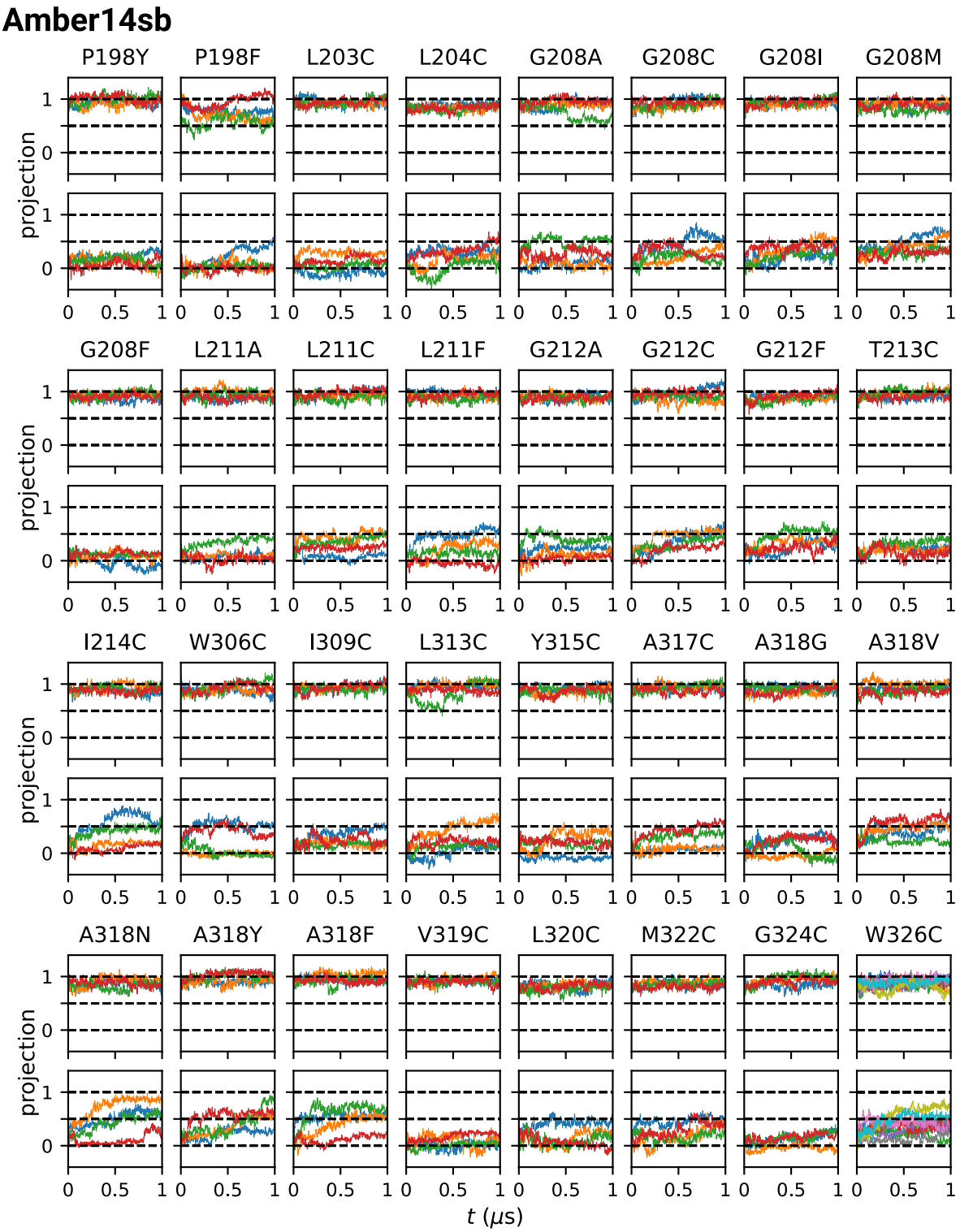

Figure 35: Projection of TREK-2 onto difference vector (Amber14sb).

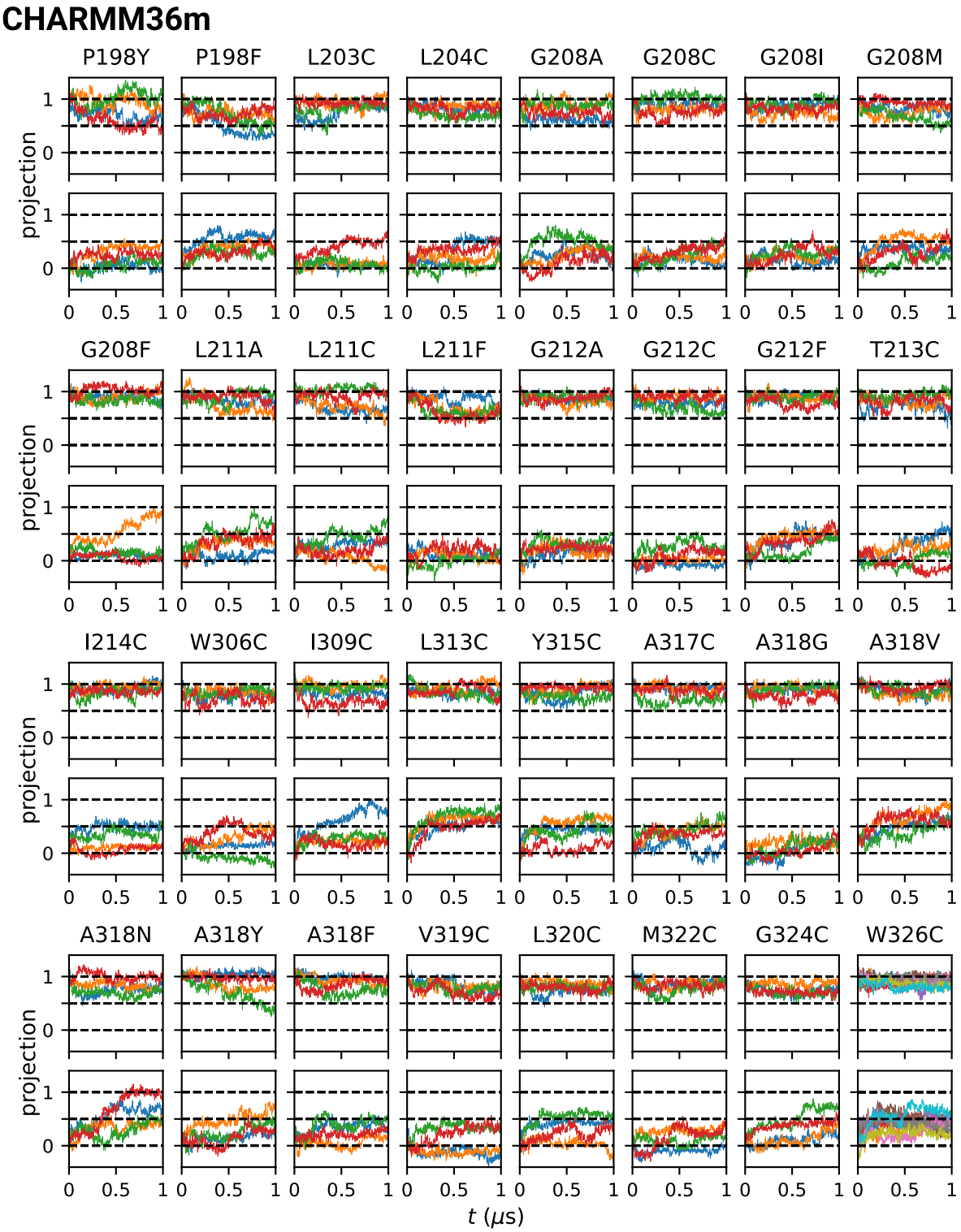

Figure 36: Projection of TREK-2 onto difference vector (CHARMM36m).

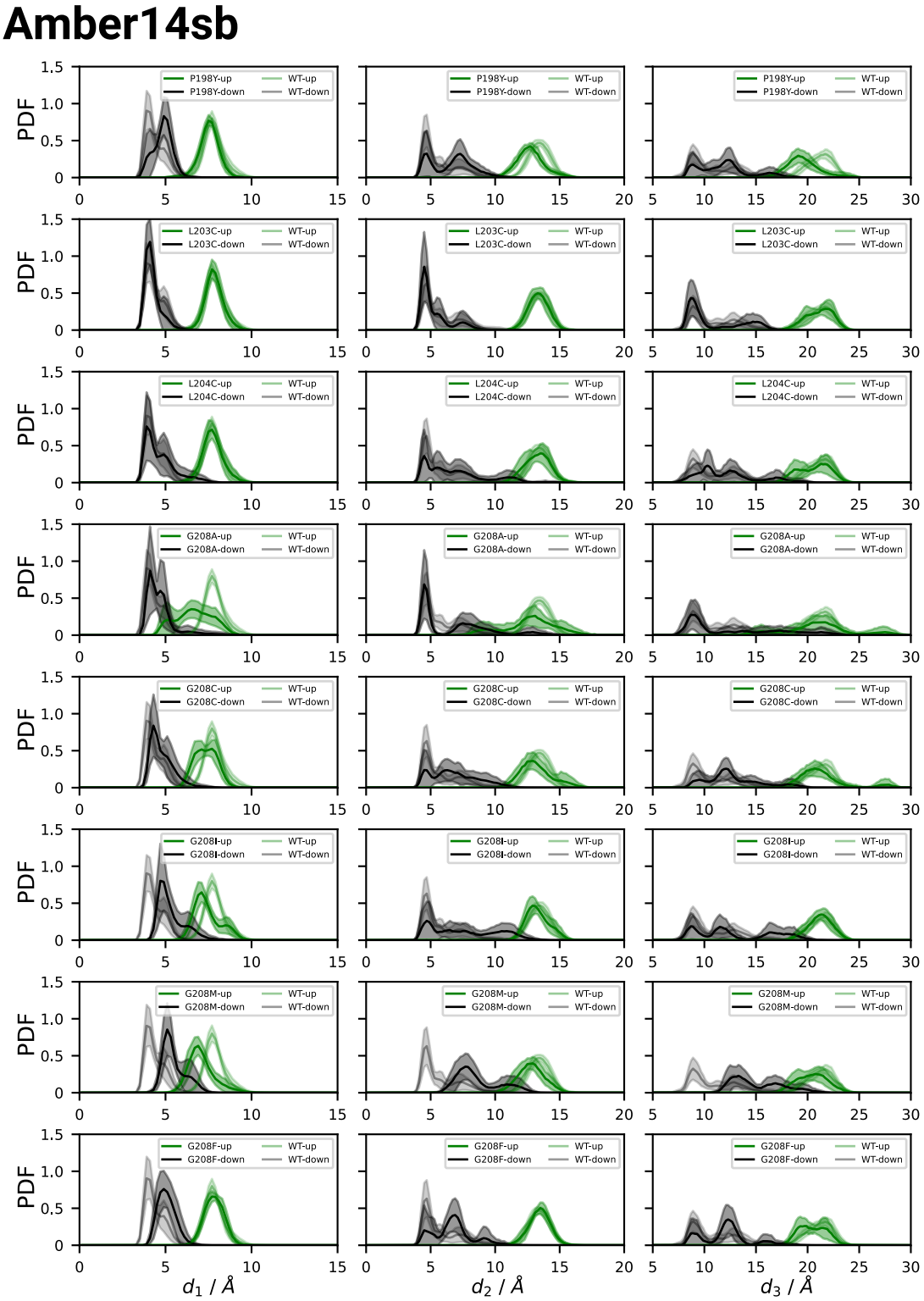

Figure 37: Probability density function of d_1, d_2 and d_3 for P198Y, L203C, L204C, G208A, G208C, G208I, G208M and G208F (Amber14sb).

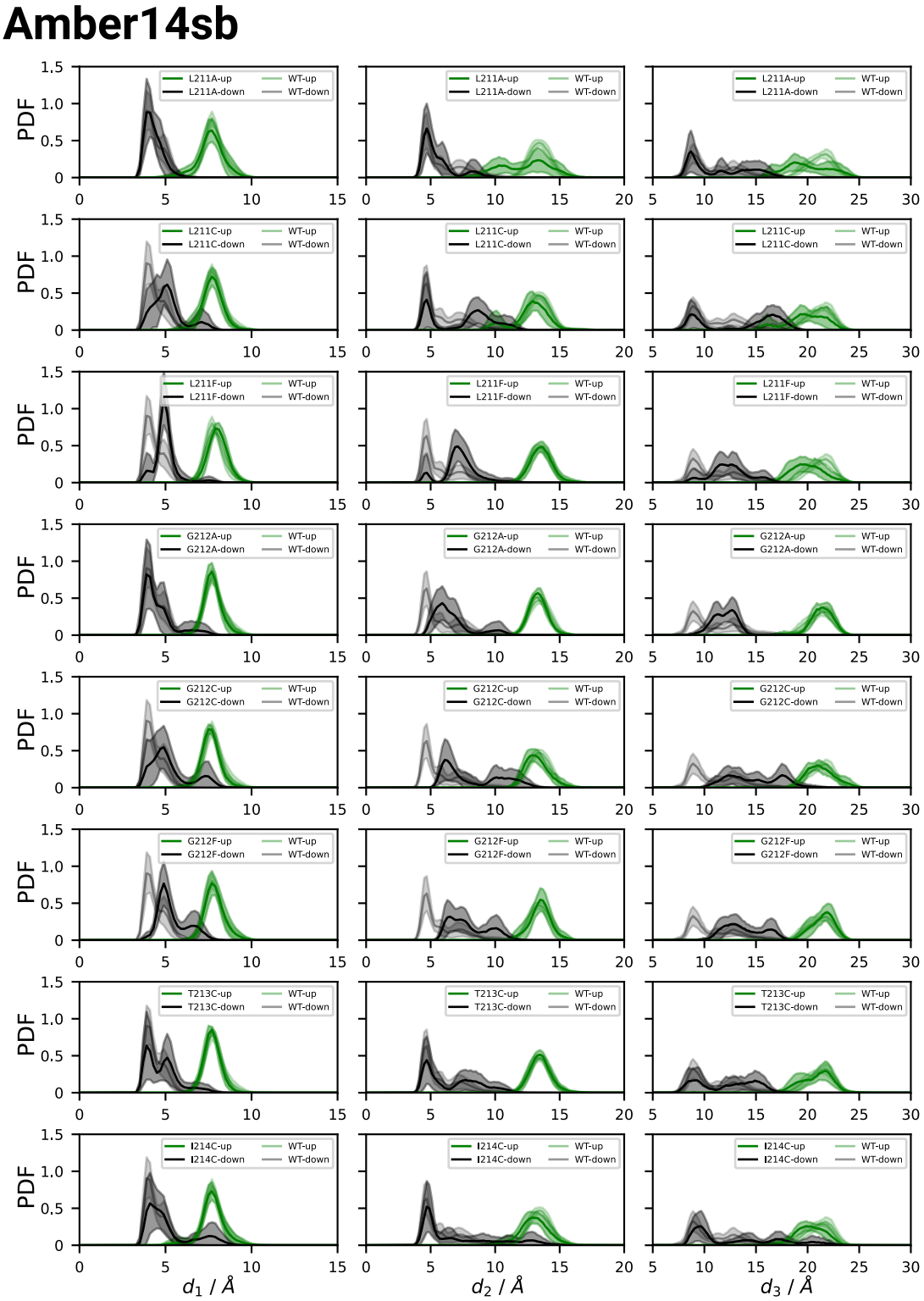

Figure 38: Probability density function of d_1, d_2 and d_3 for L211A, L211C, L211F, G212A, G212C, G212F, T213C and I214C (Amber14sb).

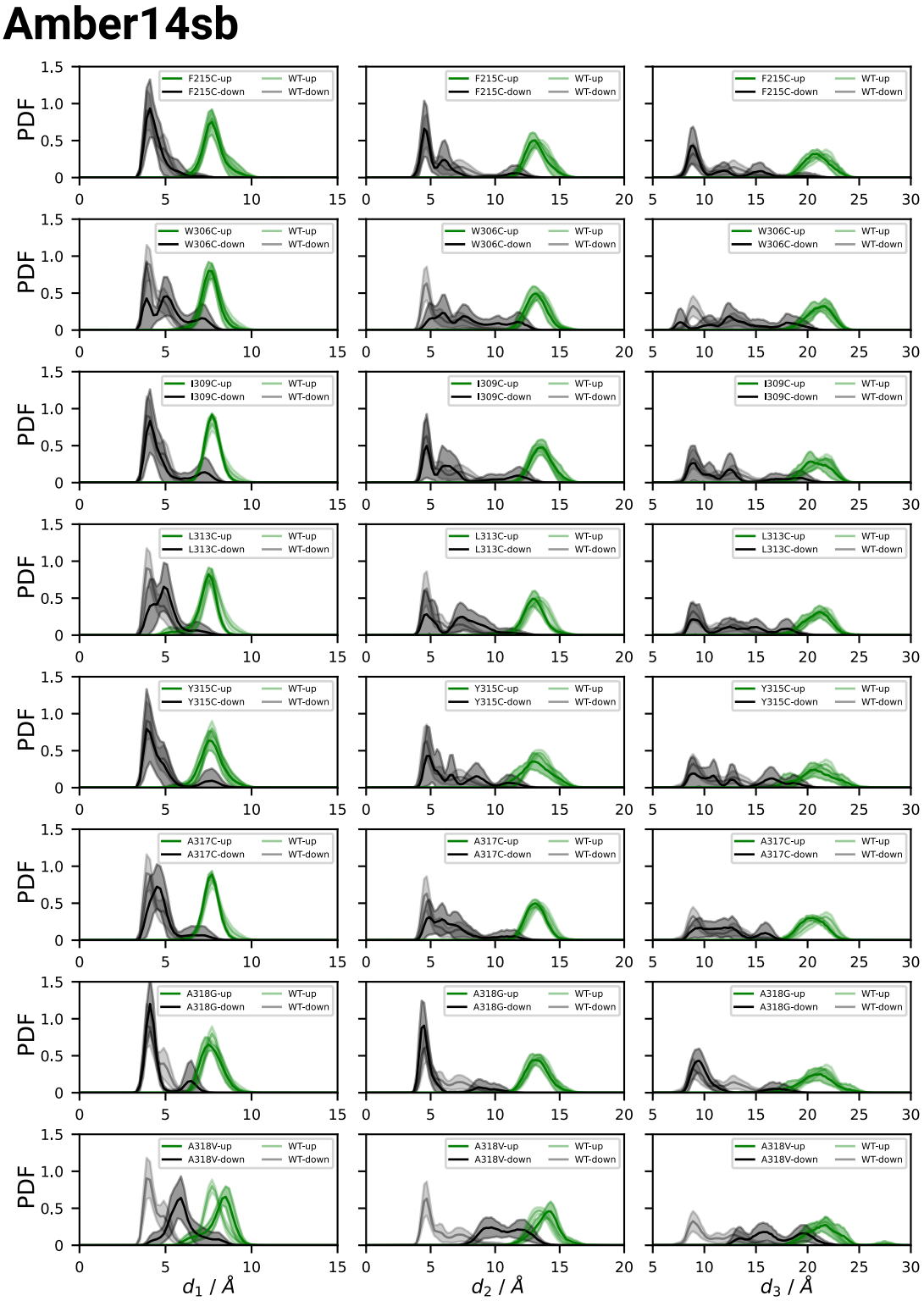

Figure 39: Probability density function of d_1, d_2 and d_3 for F215C, W306C, I309C, L313C, Y315C, A317C, A318G, A318V (Amber14sb).

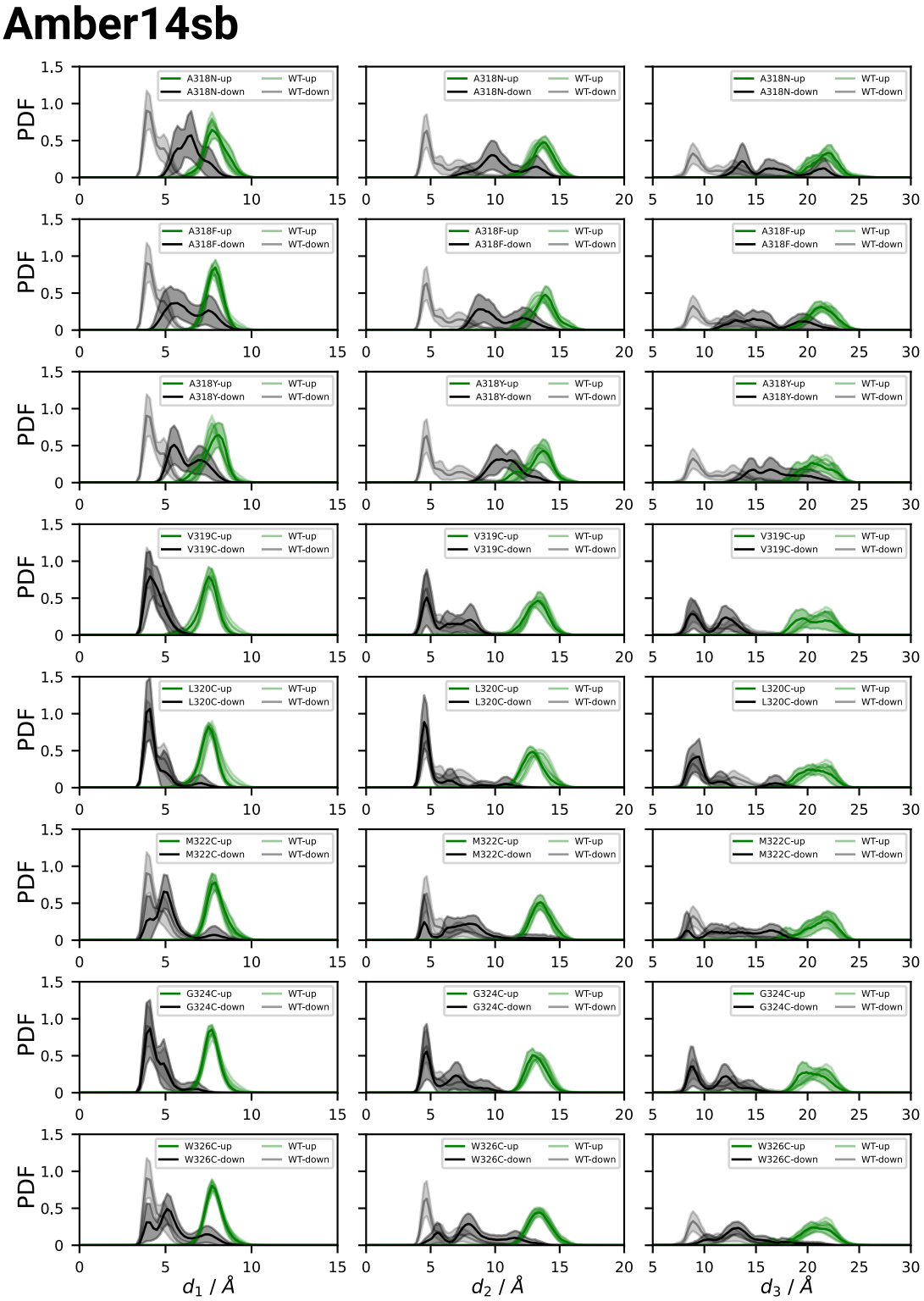

Figure 40: Probability density function of d_1, d_2 and d_3 for A318N, A318F, A318Y, V319C, L320C, M322C, G324C, W326C (Amber14sb).

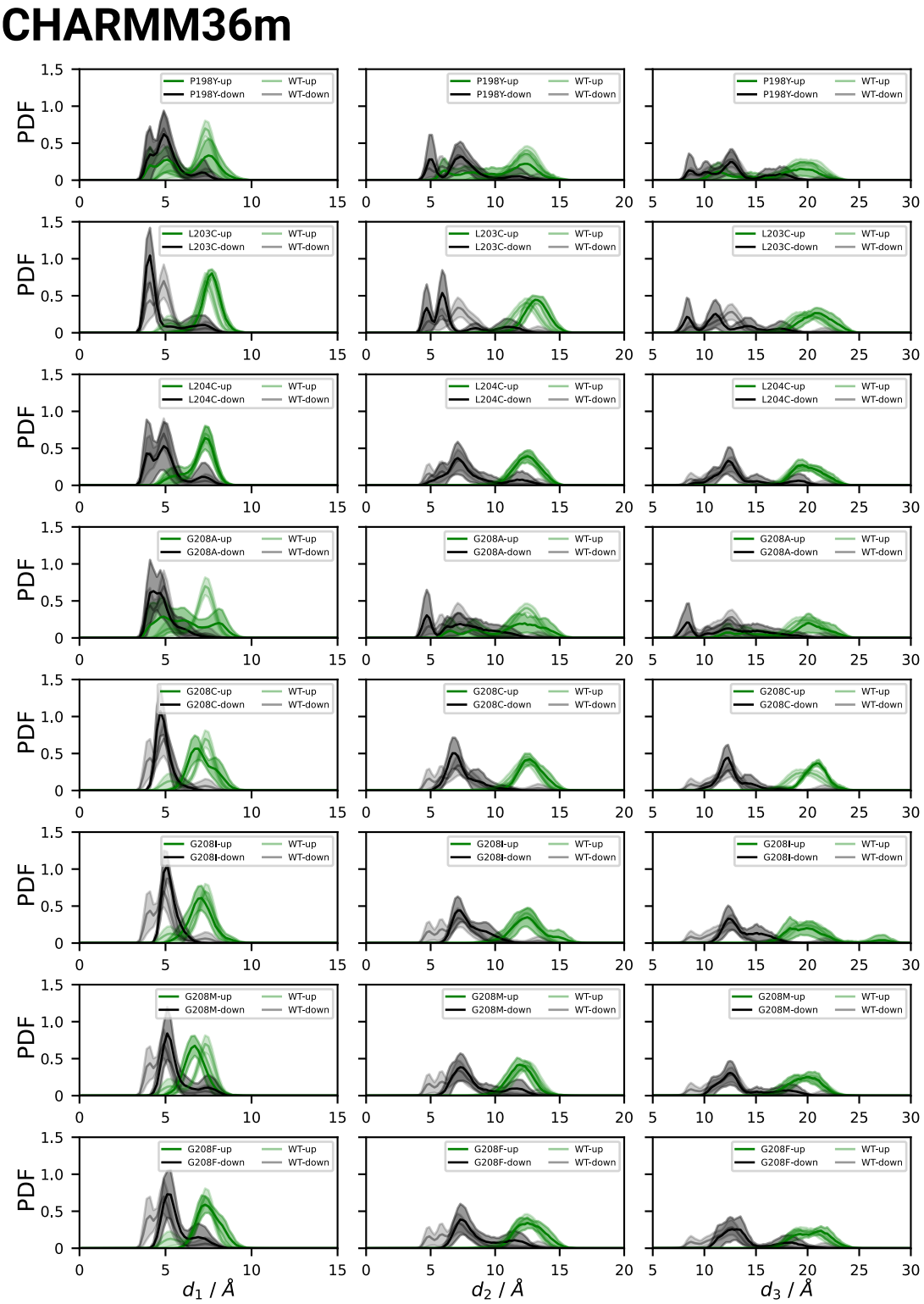

Figure 41: Probability density function of d_1, d_2 and d_3 for P198Y, L203C, L204C, G208A, G208C, G208I, G208M and G208F (CHARMM36m).

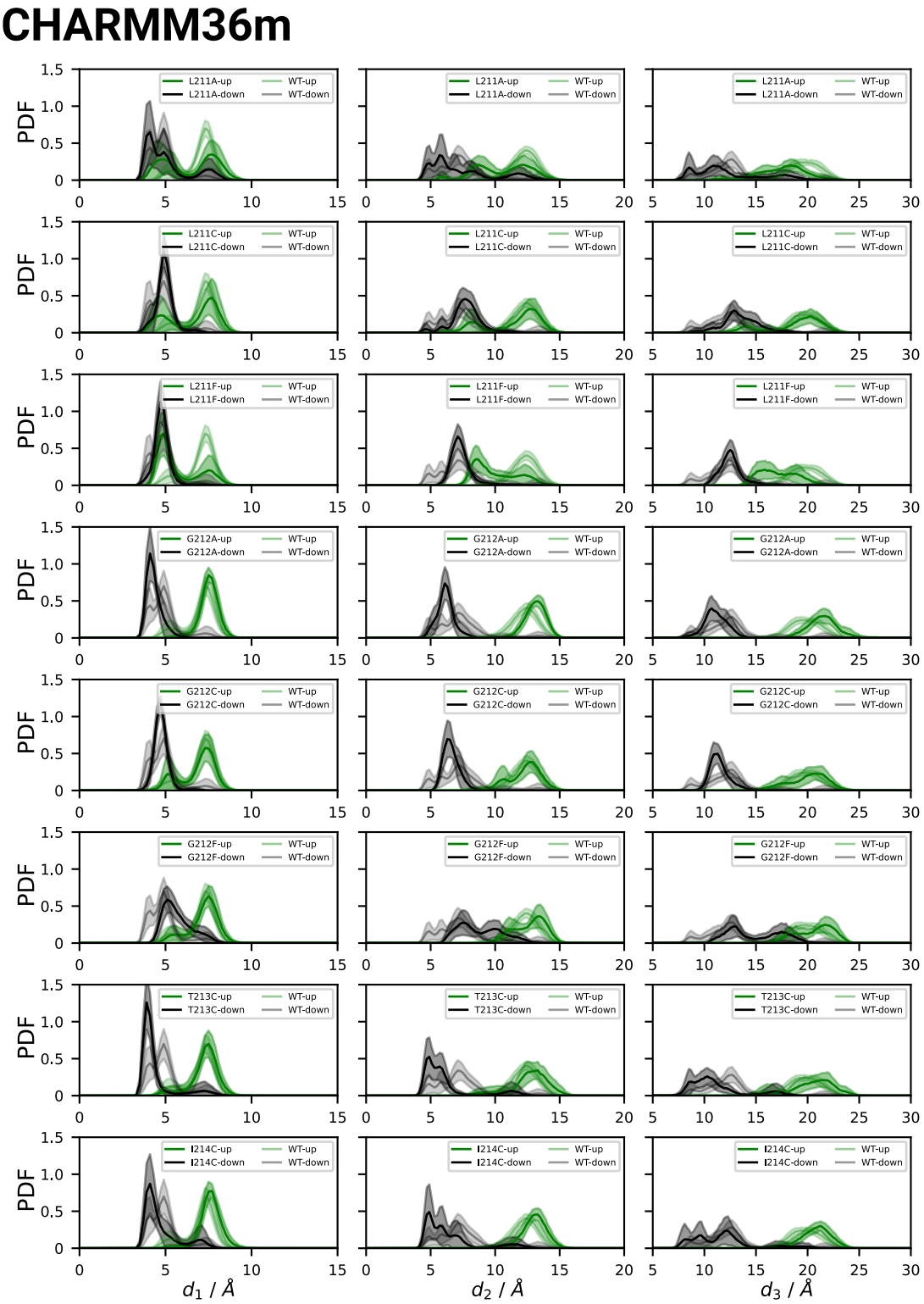

Figure 42: Probability density function of d_1, d_2 and d_3 for L211A, L211C, L211F, G212A, G212C, G212F, T213C and I214C (CHARMM36m).

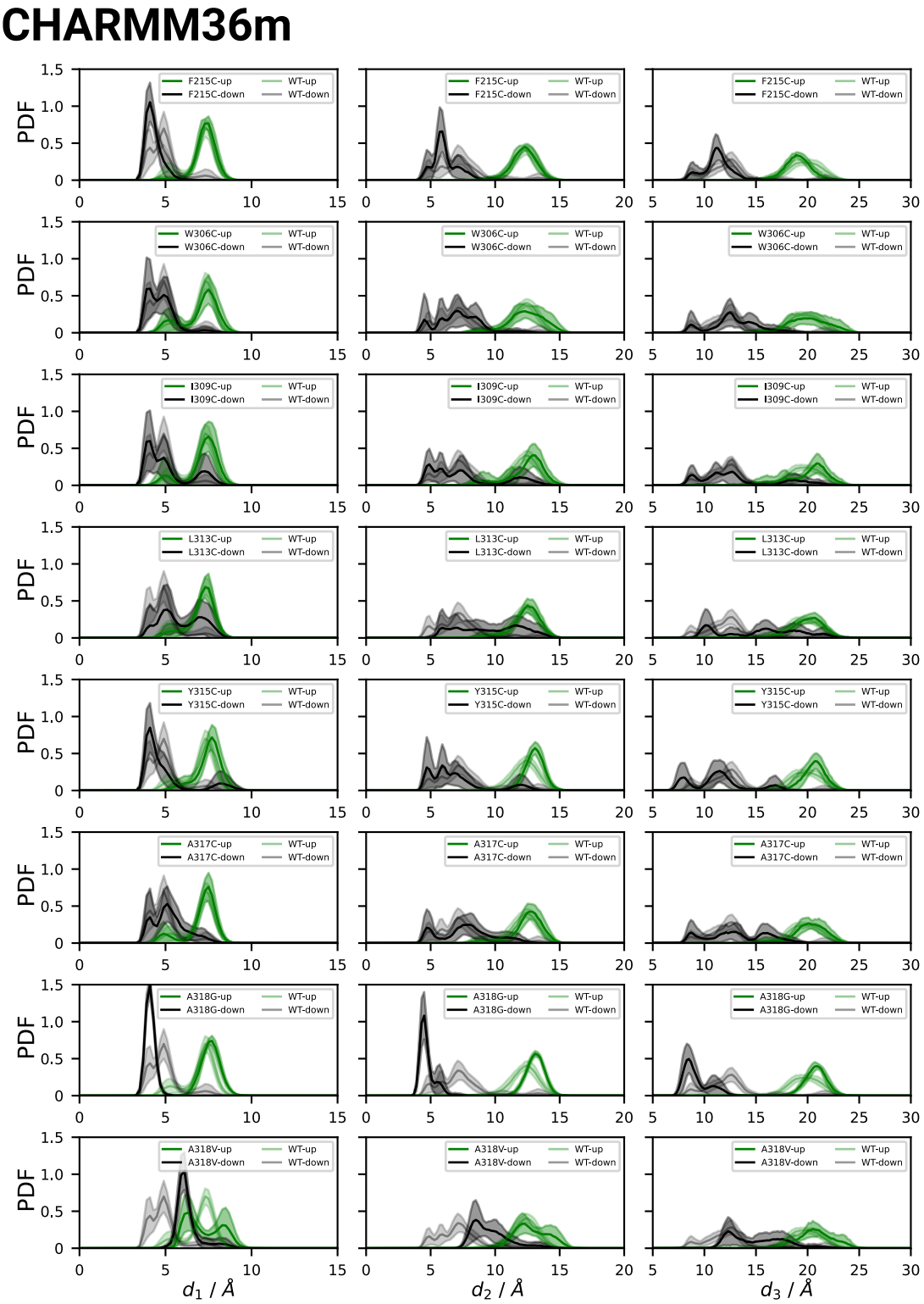

Figure 43: Probability density function of d_1, d_2 and d_3 for F215C, W306C, I309C, L313C, Y315C, A317C, A318G, A318V (CHARMM36m).

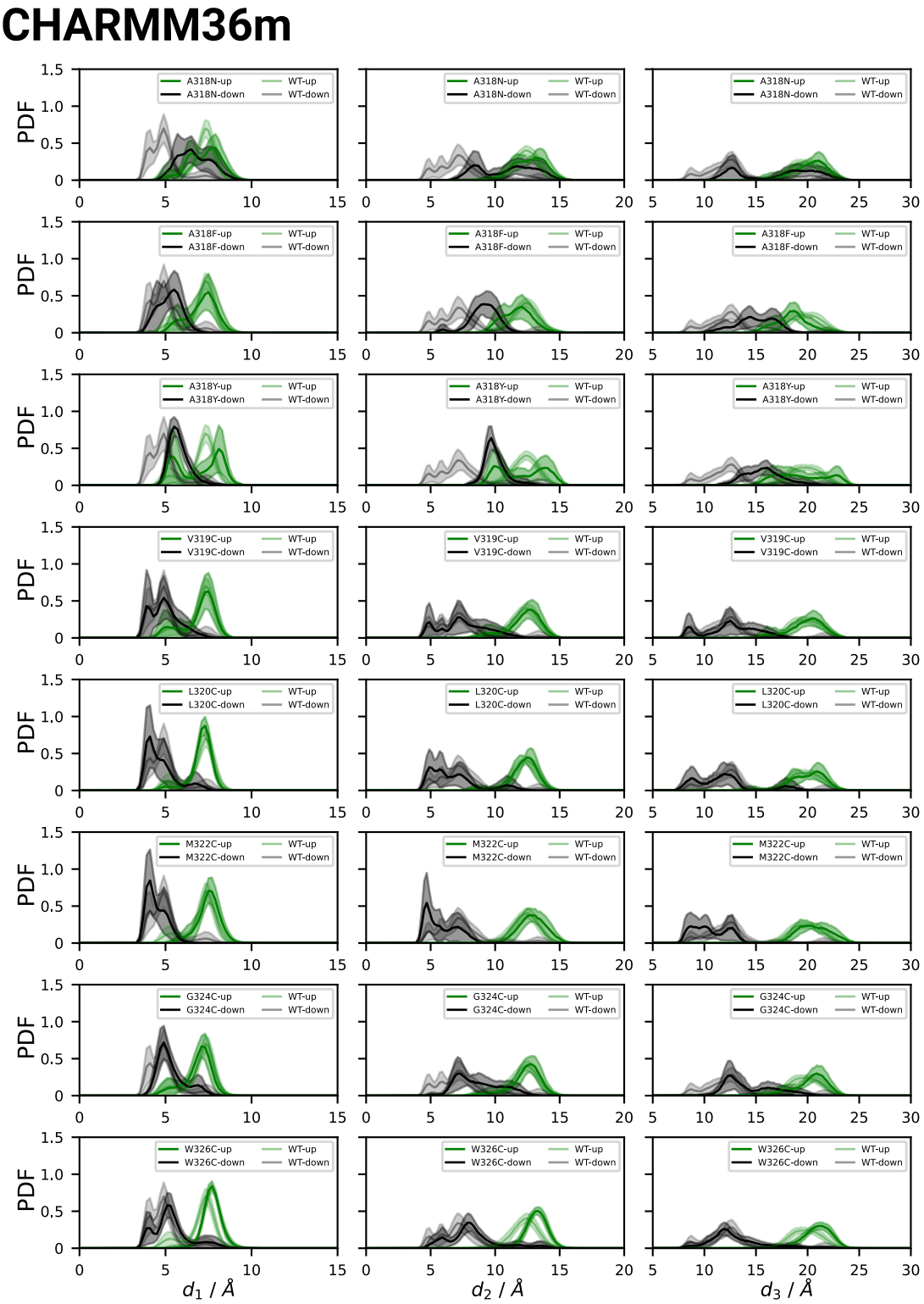

Figure 44: Probability density function of d_1, d_2 and d_3 for A318N, A318F, A318Y, V319C, L320C, M322C, G324C, W326C (CHARMM36m).

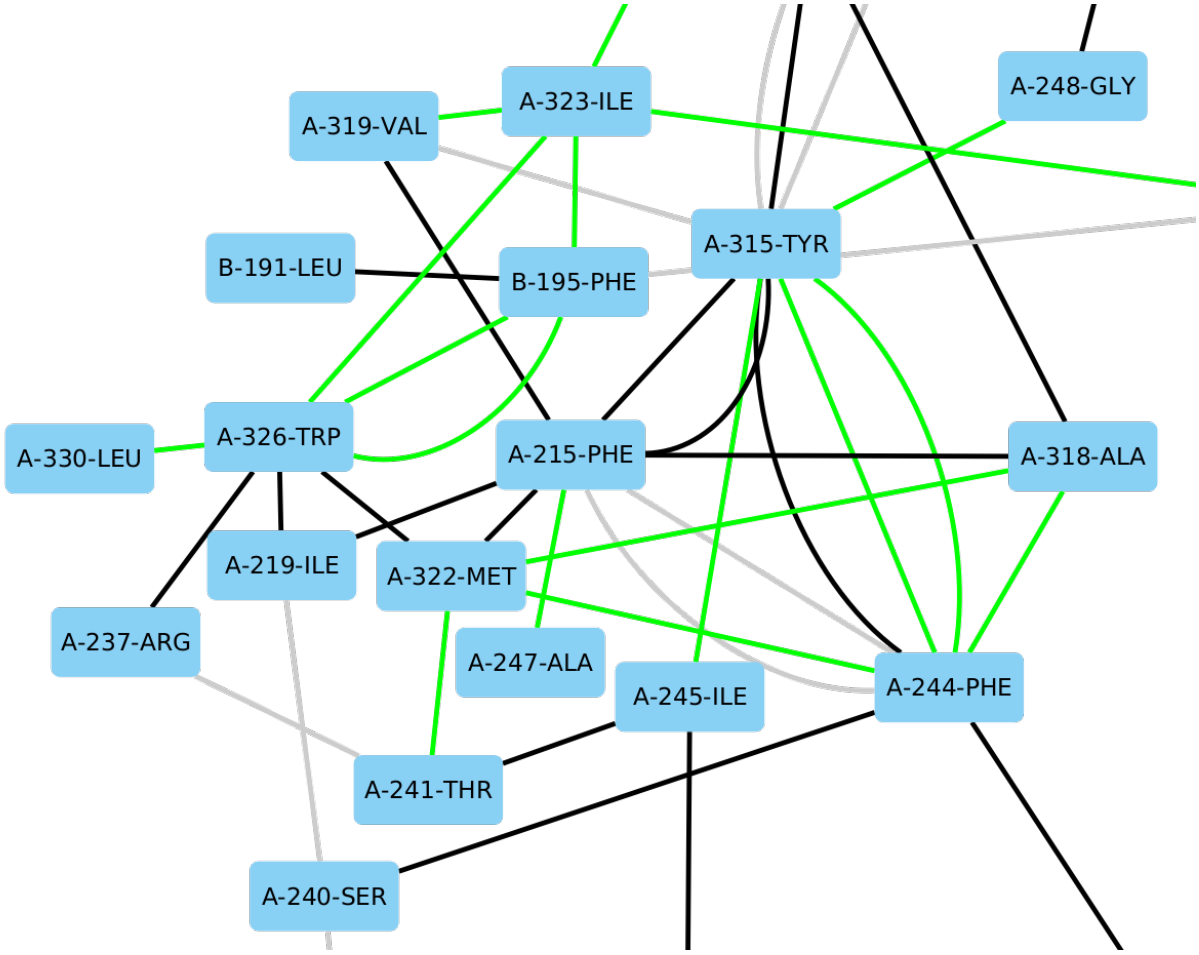

Figure 45: Residue interaction network of TREK-2 WT in crystallographic "up" and "down" conformations. Only a subset of the network is shown. Nodes represent the residues. For example, *A-326-TRP* refers to W326 in chain A. Each edge represents a main chain-side chain or a side chain-side chain interaction between two residues found only in the crystallographic "up" (green), only in the crystallographic "down" (black), or in both conformations (grey).

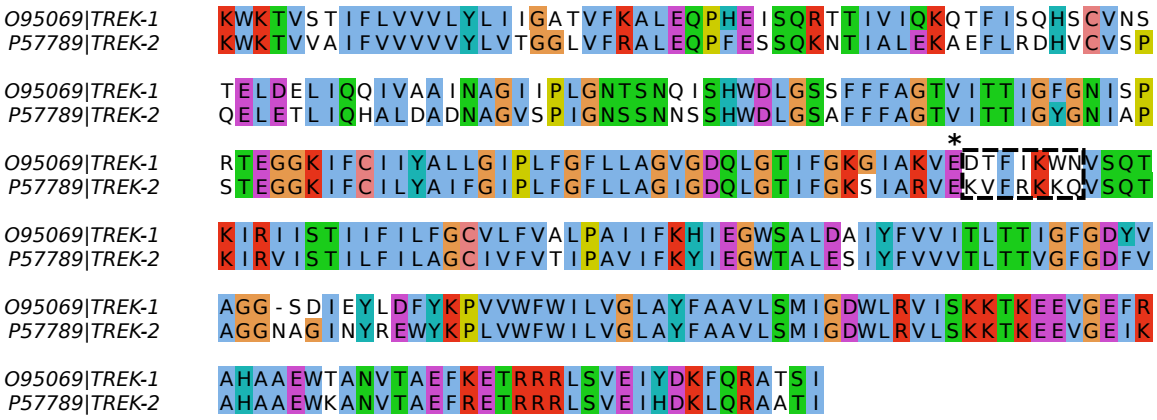

Figure 46: Sequence alignment of human TREK-1 and TREK-2. E223 of TREK-2 and the non-conserved sequence segment following E223 are indicated by an asterisk and a black dashed box, respectively.

	up		down	
residue	chain A	chain B	chain A	chain B
P198	2	2	0	1
L203	0	2	2	1
L204	2	1	0	2
G208	0	0	0	0
L211	2	2	3	4
G212	0	0	0	0
T213	1	0	0	0
I214	0	0	0	0
F215	1	2	6	6
E223	2	1	0	1
R237	0	0	1	2
W306	2	0	1	0
I309	1	1	0	1
L313	2	2	0	3
Y315	4	5	4	3
A317	1	0	0	1
A318	2	1	2	2
V319	1	1	1	1
L320	0	2	0	0
M322	3	2	2	3
G324	0	0	0	0
W326	4	2	3	2

Table 8: Number of residue-residue interactions exclusively found in crystallographic "up" and crystallographic "down", respectively. The table was derived from the residue interaction network (see Figure 45 and Methods).